



**AERODYNAMIC AND THERMAL ANALYSIS OF A HEAT SOURCE AT THE
UNDERSIDE OF A PASSENGER VEHICLE**

by

Rocky Khasow

A thesis submitted in Partial Fulfillment of the Requirements for the Degree of

Master of Applied Science

in

The Faculty of Applied Sciences

Mechanical Engineering

University of Ontario Institute of Technology

December 2014

© Rocky Khasow, 2014

Abstract and Keywords

The first part of this thesis involves full experimental and numerical studies to understand the effects of cross-winds on the automotive underbody aero-thermal phenomena using a 2005 Chevrolet Aveo5 with a heat source affixed to it to create a baseline. The results show that irrespective of the yaw angle used, only temperatures in the vicinity of the heat source increased. The rear suspension also deflected the airflow preventing heat transfer. The second part of this thesis investigated using a diffuser to improve hybrid electric battery pack cooling. It was found that the diffuser led to more consistent temperatures on the diffuser surface, suggesting the same for the battery.

Keywords: automotive aerodynamics, thermodynamics, aero-thermal, wind tunnel, computational fluid dynamics, CFD, underbody, cross-winds, battery pack, diffusers.

Acknowledgements

Financial support this research which was supported by NSERC through a Discovery and Engage grants is gratefully acknowledged. The support by Aiolos Engineering Corporation (the industry partner of this thesis) and its contact person and expert aerodynamicist (Scott Best) are greatly appreciated. The gracious support of the ACE's executives in donating some climatic wind tunnel time for this thesis is acknowledged. The hard work and professionalism of staff members of ACE including John Komar, Gary Elfstrom, Pierre Hinse, Warren Karlson, Kevin Carlucci, Tyson Carvalho, Randy Burnet, Logan Robinson, Andrew Norman, Anthony Van De Wetering is appreciated and acknowledged. The hard work of the PI's summer research students (Nicolas Quintao and Adylio Neto) in instrumenting the test vehicle is greatly appreciated.

I am fortunate to have had the support of my family through the completion of my thesis. My parents and siblings were always understanding of what I needed to do. I am also grateful to have had the support of my girlfriend Sarah Barran's family through my studies. Both my family and hers were the foundation of my support system outside of school.

The endless support by my professor, Dr. Martin Agelin-Chaab, is beyond thanks. I am forever grateful for his guidance, advice, and time

Nomenclature

Letters

V	Speed (m/s)
L	Lift (N)
D	Drag (N)
∇	Gradient operator
\bar{V}	Averaged Velocity (m/s)
ρ	Density (kg/m ³)
\bar{p}	Pressure (Pa)
μ	Viscosity (Pas)
λ	Reynolds Stresses
Pr	Prandtl Number
k	Turbulent Kinetic Energy (J)
C_1, C_2	Transition-SST turbulence model constants
Re	Reynolds Number
SD	Specific Dissipation Rate (W/K)
Q	Heat exchanger heat transfer rate (W)
T	Temperature (K)
R	Gas constant (J/kgk)
W	Weight (kg)

Greek Symbols

ω	Turbulent Eddy Frequency (1/s)
$C_1, C_2, \alpha, \sigma_k$ and σ_ω	Transition-SST turbulence model constants

Superscripts

+	Dimensionless wall distance
---	-----------------------------

Subscripts

<i>hot,in</i>	At the Hot fluid inlet of a heat exchanger
<i>cold,in</i>	At the Cold fluid inlet of a heat exchanger
<i>t</i>	Turbulent parameter
<i>numerical</i>	From the numerical data
<i>experimental</i>	From the experimental data
<i>ref</i>	Reference value

Table of Contents

Abstract and Keywords.....	ii
Acknowledgements.....	iii
Nomenclature	iv
Chapter 1: Introduction	1
1.1: Background and Motivation	1
1.2: Objectives	5
1.3: Thesis Structure	7
Chapter 2: Literature Review	8
2.1: Automotive Aerodynamics	8
2.2: Automotive Underbody and Underhood Aerodynamics	12
2.3: Aero-thermal Research	17
2.4: Electric Vehicles and Battery Cooling.....	21
Chapter 3: Methodology	25
3.1: Experimental Measurements.....	25
3.1.1: Experimental Test Facility.....	25
3.1.2: Experimental Test Vehicle Instrumentation	27
3.1.3: Test Matrix.....	30
3.2: Numerical Simulation	31
3.2.1: Numerical Introduction.....	31
3.2.2: Governing Equations	31
3.2.3: Geometry and Boundary Conditions	33
3.2.4: Mesh Generation.....	35
Chapter 4: Results and Discussion.....	39
4.1: Experimental Results	39
4.1.1: Temperature Distribution of the Hotplate.....	39
4.1.2: Temperature Distributions of Vehicle Underbody	42
4.1.3: Flow Visualization with Tufts	52
4.2: Numerical Data	61
4.2.1: Numerical Validation.....	61
4.2.2 Grid Independence	67
4.2.3: Numerical Results.....	72
4.2.3.1: Thermal Results	72

4.2.3.2: Velocity Results	83
4.3: Underbody Battery Pack Cooling Simulation Results.....	96
4.3.1: Numerical Results.....	97
Chapter 5: Conclusion and Recommendations	104
5.1: Summary of Results.....	104
5.2: Contribution	106
5.3: Recommendations for Future Works	107
References.....	108
Appendix A: Passenger Side Grid Independence Test	115

List of Figures

Figure 1.1: Illustrating aerodynamic forces acting on a vehicle, with V representing the velocity of the vehicle; L representing lift; and D representing drag.	2
Figure 1.2: A diffuser (circled) on the vehicle studied in this thesis.	4
Figure 3.1: The test vehicle inside the climatic wind tunnel.	26
Figure 3.2: The hot plate attached to the gas tank under the vehicle.	27
Figure 3.3: The vehicle underbody, showing the flow direction, position of the hotplate (dotted line rectangle), and thermocouples (dots) and probes (circles). The left side is the driver's side.	29
Figure 3.4: Schematic of the simulation domain with the vehicle inside it for the 15 yaw case.	33
Figure 3.5: Unstructured tetrahedral mesh. (a) side view of the car, (b) close up side view of front of the car, (c) close up side view of rear of the car (d) close up view of exhaust piping with two cut planes, (e) front view of the car with two cut planes, (f) close up on the hot plate with two cut planes.	36
Figure 3.6: Prism layers on the trunk of the vehicle.	37
Figure 3.7: Quality histogram for the a.) 0 yaw, b.) 8 yaw, and c.) 15 yaw meshes. Horizontal axis is the quality, and the vertical axis is the number of elements at a given quality.	38
Figure 4.1: Temperature contours of the hotplate at selected test conditions seen by the infra-red thermal camera. (a) 0° yaw, (b) 8° yaw, (c) 29.2° yaw and (d) 15.6° yaw..	40
Figure 4.2: Hotplate temperature at different yaw angles.	41
Figure 4.3: Hotplate temperature at different yaw angles.	42
Figure 4.4: Underbody temperatures for 0° yaw, 50 km/h and 10°C.	44
Figure 4.5: Underbody temperatures for 15.6° yaw, 50 km/h and 10°C.	45
Figure 4.6: Underbody temperatures for 29.2° yaw, 50 km/h and 10°C.	46
Figure 4.7: A picture of the mounted the hotplate and labels of the most sensitive thermocouples recorded in the experiments.	47
Figure 4.8: Underbody temperature distribution for selected thermocouples at different yaw angles.	49

Figure 4.9: Underbody temperature distribution for selected thermocouples at different yaw angles.....	50
Figure 4.10: Underbody temperature distribution for selected thermocouples at different yaw angles.....	51
Figure 4.11: Underbody temperature distribution for selected thermocouples at different yaw angles.....	52
Figure 4.12: A screen shot from a flow visualization video for 0° yaw (Test 1 in Table 1) at the driver side (a) and passenger side (b). Average directions of the tufts are represented by arrows.	54
Figure 4.13: A screen shot from a flow visualization video for 15.6° yaw (Test 2 in Table 1) at the driver side (a) and passenger side (b). Average directions of the tufts are represented by arrows.	56
Figure 4.14: A screen shot from a flow visualization video for 29.2° yaw (Test 3 in Table 1) at the driver side (a) and passenger side (b). Average directions of the tufts are represented by arrows.	57
Figure 4.15: A screen shot from a flow visualization video for -29.2° yaw (Test 4 in Table 1) at the driver side (a) and passenger side (b). Average directions of the tufts are represented by arrows.	58
Figure 4.16: A screen shot from a flow visualization video for 0° yaw (Test 6 in Table 1) at the driver side (a) and passenger side (b). Average directions of the tufts are represented by arrows.	59
Figure 4.17: A screen shot from a flow visualization video for 15.6° yaw (Test 8 in Table 1) at the driver side (a) and passenger side (b). Average directions of the tufts are represented by arrows.	60
Figure 4.18: Thermocouples used for numerical validation. Thermocouples encircled in red are on the passenger side, thermocouples encircled in blue are on the driver side.	61
Figure 4.19: Comparison of numerical and experimental temperature data 3 cm away from the hotplate at 0° yaw on the driver side.	62
Figure 4.20: Comparison of numerical and experimental temperature data 6 cm away from the hotplate at 0° yaw on the driver side.	63

Figure 4.21: Comparison of numerical and experimental temperature data 9 cm away from the hotplate at 0° yaw on the driver side.	63
Figure 4.22: Comparison of numerical and experimental temperature data 3 cm away from the hotplate at 29.2° yaw on the driver side.	64
Figure 4.23: Comparison of numerical and experimental temperature data 6 cm away from the hotplate at 29.2° yaw on the driver side.	65
Figure 4.24: Comparison of numerical and experimental temperature data 9 cm away from the hotplate at 29.2° yaw on the driver side.	65
Figure 4.25: Percent difference in the numerical and experimental results for the driver side.	66
Figure 4.26: Percent difference in the numerical and experimental results for the passenger side.	67
Figure 4.27: Showing the locations used for the grid independence test. The yellow lines indicate the locations data was compared across.	68
Figure 4.28: Coarse mesh of the vehicle.	69
Figure 4.29: Medium mesh of the vehicle.	69
Figure 4.30: Fine mesh of the vehicle.	70
Figure 4.31: Grid independence test illustrating the temperature along the front location of the solid rear axle.	71
Figure 4.32: Grid independence test illustrating the temperature along the rear location of the solid rear axle.	71
Figure 4.33: A zoomed in view of the temperature contours at the vehicle centerline from the side profile for Test 1.	73
Figure 4.34: Zoomed in view of the temperature contours 5 mm below the surface of the gas tank from the top view for Test 1.	73
Figure 4.35: A zoomed in view of the temperature contours at the vehicle centerline from the side profile for Test 7.	75
Figure 4.36: Zoomed in view of the temperature contours 5 mm below the surface of the gas tank from the top view for Test 7.	75
Figure 4.37: A zoomed in view of the temperature contours at the vehicle centerline from the side profile for Test 8.	76

Figure 4.38: Zoomed in view of the temperature contours 5 mm below the surface of the gas tank from the top view for Test 8.	77
Figure 4.39: A zoomed in view of the temperature contours at the vehicle centerline from the side profile for Test 3.	78
Figure 4.40: Zoomed in view of the temperature contours 5 mm below the surface of the gas tank from the top view for Test 3.	78
Figure 4.41: Temperature isosurfaces at a.) 283.5K, b.) 285K, c.) 290K for Test 1. .	80
Figure 4.42: Temperature isosurfaces at a.) 283.5K, b.) 285K, c.) 290K for Test 7. .	81
Figure 4.43: Temperature isosurfaces at a.) 283.5K, b.) 285K, c.) 290K.....	82
Figure 4.44: Temperature isosurfaces at a.) 283.5K, b.) 285K, c.) 290K for Test 3. .	83
Figure 4.45: Velocity contours at the vehicle centreline from the side profile for Test 1.	84
Figure 4.46: Zoomed in view of velocity contours at the vehicle centreline from the side profile for Test 1.	85
Figure 4.47: Velocity contours 5 mm below the gas tank from the top view for Test 1.	85
Figure 4.48: Velocity contours at the vehicle centreline from the side profile Test 7.	86
Figure 4.49: Zoomed in view of velocity contours at the vehicle centreline from the side profile for Test 7.	87
Figure 4.50: Velocity contours 5 mm below the gas tank from the top view for Test 7.	87
Figure 4.51: Velocity contours at the vehicle centreline from the side profile for Test 8.	88
Figure 4.52: Zoomed in view of velocity contours at the vehicle centreline from the side profile for Test 8.	89
Figure 4.53: Velocity contours 5mm below the gas tank from the top view Test 8. .	89
Figure 4.54: Velocity contours at the vehicle centreline from the side profile for Test 3.	90
Figure 4.55: Zoomed in view of velocity contours at the vehicle centreline from the side profile for Test 3.	91
Figure 4.56: Velocity contours 5 mm below the gas tank from the top view Test 8. .	91
Figure 4.57: Velocity streamlines a.) in front of the vehicle, b.) behind the vehicle, c.) over and d.) under the vehicle for Test 1.	92

Figure 4.58: Velocity streamlines a.) in front of the vehicle, b.) behind the vehicle, c.) over and d.) under the vehicle for Test 7.	93
Figure 4.59: Velocity streamlines a.) in front of the vehicle, b.) behind the vehicle, c.) over and d.) under the vehicle for Test 8.	94
Figure 4.60: Velocity streamlines a.) in front of the vehicle, b.) behind the vehicle, c.) over and d.) under the vehicle for Test 3.	95
Figure 4.61: Velocity contours at vehicle centerline for a) the no diffuser case, and b) the diffuser case.	97
Figure 4.62: Velocity contour at vehicle centerline at the front of the vehicle for a.) the no diffuser case and b.) the diffuser case.	98
Figure 4.63: Velocity contour at vehicle centerline at the rear of the vehicle for a.) the no diffuser case and b.) the diffuser case.	98
Figure 4.64: Velocity streamlines at the rear section of the vehicle for the no diffuser case showing a.) the top-rear view and b.) the bottom rear view.	99
Figure 4.65: Velocity streamlines at the rear section of the vehicle for the diffuser case showing a.) the top-rear view and b.) the bottom rear view.	100
Figure 4.66: Temperature contour of the battery pack for a.) the no diffuser case and b.) the diffuser case.	100
Figure 4.67: Temperature contour of the battery pack at the vehicle centerline for a.) the no diffuser case and b.) the diffuser case.	101
Figure 4.68: Temperature isosurface at 300.125K of the battery pack at the vehicle centerline for a.) the no diffuser case and b.) the diffuser case.....	102
Figure 4.69: Temperature isosurface at 301K of the battery pack at the vehicle centerline for a.) the no diffuser case and b.) the diffuser case.	102
Figure 4.70: Temperature isosurface at 303K of the battery pack at the vehicle centerline for a.) the no diffuser case and b.) the diffuser case.	103

List of Tables

Table 1: The test matrix. Tests marked with a * indicates non-rotating wheels for that test.

..... 30

Chapter 1: Introduction

1.1: Background and Motivation

When moving air hits a vehicle, a variety of forces on the vehicle are generated. The air can push down or push up on the vehicle depending on the design; these are called downforce and lift respectively. The air can also push against the direction of vehicle travel, causing resistance, called drag (Barnard, 2009). Downforce, also called negative lift, is considered a positive effect on a vehicle given its ability to increase vehicle stability. Lift and drag are negative effects on a vehicle. Lift causes a reduction in the tires contact with the road and hence reduction in vehicle stability. This is felt in the vehicle as twitchy, inconsistent steering and suspension control (Barnard, 2009a). Drag causes an increase in fuel consumption, due to additional forces resisting the movement of the vehicle. This causes the motor to have to work harder, and as a result burn more fuel, to travel at a given speed. These two aerodynamic effects form the focus of automotive aerodynamics research.

Automotive aerodynamics is the study of the air flow around and through a vehicle during operating conditions with the aim of limiting drag (Hucho, 1993). A key concern in automotive aerodynamics is the balancing of the economics and styling of the vehicle versus the aerodynamic characteristics. Often times, the characteristics that do result are due to accommodating economic and packaging factors, versus the other way around (Hucho, 1993). Since drag also has effect on fuel consumption, aerodynamics is also of interest in research aiming to improve fuel efficiency.

The global decline in fossil fuel reserves, rising fuel prices and the damaging effects of global warming have necessitated the need to minimize fossil fuel consumption. The transportation sector in particular heavily depends on fossil fuels, especially those of Canada and the United States. Electric vehicle (EV) and Hybrid electric vehicle (HEV) technology has improved significantly in recent years and offer huge potential to decrease our fossil fuel dependence. However, cooling the battery packs used in EVs and HEVs is still a challenge that requires solutions. Battery packs for EVs and HEVs have specific cooling demands, including uniform cooling within a desired range that is still difficult to achieve. There are therefore aggressive research programs focusing on different cooling techniques from phase-change material to liquid cooling, and natural and forced convective air cooling.



Figure 1.1: Illustrating aerodynamic forces acting on a vehicle, with V representing the velocity of the vehicle; L representing lift; and D representing drag.

Commonly, drag and lift reduction in road vehicles is done through the use of aerodynamic devices, such as wings, spoilers, air dams, side skirts, underbody diffusers, etc. These can be built into the design of the vehicle at the design stages or as add on device. Underbody diffusers in road vehicles is one such device, for example, that works like the reverse of a nozzle. The entrance of the diffuser is usually small to increase the velocity of the air, and the exit is large, to decrease the velocity (Barnard, 2009b). When a fluid speeds up, per the Bernoulli principle, its static pressure decreases, thus leading to an increase in downforce where the flow is faster (Barnard, 2009c). The velocity decrease at the diffuser exit, which is usually close the back of the vehicle, and causes an increase in pressure in the wake. The wake is the air immediately downstream of the vehicle. After passing over the vehicle, this air is often highly turbulent and separated from the vehicle surface. In addition to this the air immediately behind the vehicle is called “dead air” which is very slow. In order to reduce pressure drag with a diffuser, the diffuser should be designed to have the air exit it at a low velocity into the dead water to keep the pressure relatively high. This results in an effective reduction in pressure difference between the front and back of the vehicle leading to a reduction in the aerodynamic drag.

These principles are applied to thermal management in the form of ducting and nozzles such as grille openings, and brake ducts to speed up the flow near critical areas and slow down the flow at the exit to limit disturbing and energizing the wake.

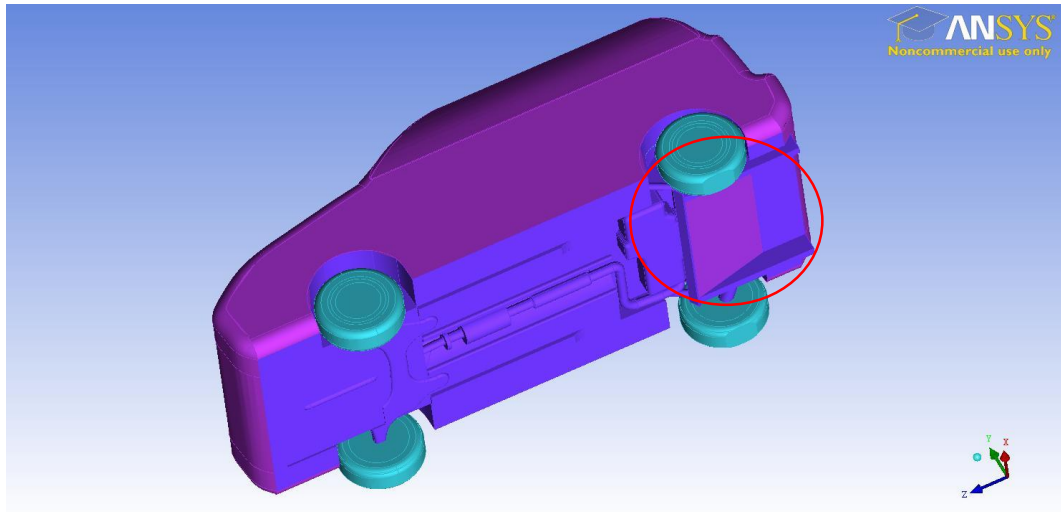


Figure 1.2: A diffuser (circled) on the vehicle studied in this thesis.

Thermal management is a major consideration in the design of vehicles for passenger comfort and efficient performance of various components. Aerodynamic thermal management is highly dependent on air flow around components requiring cooling. Faster moving air results in a higher convective cooling coefficient, which results in more effective heat transfer (Costa, 2003). As a result, numerous wind tunnel tests are performed to study vehicle thermal phenomena such as underhood and underbody temperature distribution in an effort to understand the combined aerodynamics and thermodynamics of the entire vehicle. Although vehicles encounter cross-winds in real world driving conditions, the majority of automotive climatic wind tunnel testing and development is performed in wind tunnels without cross-wind capability. This has therefore made it difficult to study in detail the effects of cross-wind on vehicle thermal phenomena. Hucho (1993) has noted a vehicle's dynamic sensitivity to cross-winds through yawing moments imparted on the vehicle, though his research did not consider the thermal effects from the cross-wind. Research on cross-wind effects on vehicles is still limited.

Traditionally aerodynamic and thermal (aero-thermal) management primarily focuses on under hood cooling (Costa, 2003; Kuthada and Widemann, 2008; Fournier, 2004; Khaled et al., 2012, etc). However, growing engine power demands, utilization of sophisticated underhood and underbody devices, and emission regulations all contribute to make underhood and underbody aero-thermal management challenging. Although air penetration into the vehicle underhood improves cooling of the components, it also increases the overall aerodynamic drag of a vehicle (Barnard, 2009d). Similar to the lack of cross-wind aerodynamic research, aero-thermal research is also limited. This study will investigate how the temperature and velocity distributions could be usefully modified through using aerodynamic devices such as a diffuser to further cool underbody components.

As discussed earlier, there are thermal cooling demands specific to the battery in the rapidly improving field of EV and HEV technology. The vehicles are equipped with a rechargeable battery pack, commonly as part of the vehicle underbody, that stores electrical energy obtained from various means (i.e., plugging into a charging station, regenerative charging). However, cooling the battery pack is still one of the main challenges that require solutions. The specific cooling demands of batteries include uniform cooling within a desired range which is still difficult to achieve. There are therefore aggressive research programs focusing on different cooling techniques from phase-change material to liquid cooling, and natural and forced convective air cooling (Chan, 2007; Al-Hallaj and Selman, 2002; Park, 2013; Pesaran, 2001, 2002; etc).

1.2: Objectives

The primary research objective is to study the velocity and temperature patterns at the underbody of a realistic vehicle using an arbitrary heat source (a hotplate). The heat source

was affixed to the underbody of said vehicle in cross-winds of various angles and temperatures. The hotplate is designed to limit the effects on aerodynamics under the body in order to reduce the effects of this added variable on the underbody flow. This was done using the capabilities of the UOIT's full scale wind tunnel at the Automotive Center for Excellence (ACE). With the baseline established by the above research – studying the effect of a generic heat source under the vehicle – the concept is expanded in a secondary objective, which will study how underbody components can be cooled with the underbody airflow, such as differentials or battery packs. To expand on this further, the secondary objective will investigate if the aerodynamics benefits of existing underbody diffusers can be applied to improve cooling HEV battery packs.

The summary of the objectives is as follows:

1. To measure and analyse the velocity distributions of the air at the underbody of the Chevrolet Aveo5 at different yaw angles experimentally and numerically. This will help to understand the effects of yaw angle and ambient temperature on the velocity distributions.
2. To measure and analyse the temperature distributions of the air around the Chevrolet Aveo5 with a heat source attached to it in order to understand the effects of angle and temperature on the velocity and temperature distributions, experimentally and numerically.
3. To simulate and analyse the effectiveness of using the existing underbody diffusers in the market to facilitate cooling of a battery pack.

1.3: Thesis Structure

This thesis is organized into five chapters including the current chapter. Chapter 2 highlights literature reviewed in preparation for the thesis, noting important literature in the automotive aerodynamic and electric vehicle battery fields. Chapter 3 details the methodology of the analysis completed, both experimentally and numerically. In Chapter 4, the discussion of the results of the analyses is reported. Finally, Chapter 5 presents conclusions of the study and recommendations for future work.

Chapter 2: Literature Review

2.1: Automotive Aerodynamics

Automotive aerodynamic research has primarily focused on the exterior shape and adapting to economic and packaging demands (Hucho, 1993). Automobiles, despite being streamlined in comparison to buildings or trains, are considered to be aerodynamically similar; that is, they are considered to be a bluff body. A bluff body is a shape in which flow separation dominates the aerodynamic characteristics (Cooper, 1993). The field has predominantly taken drag reduction as a guideline for aerodynamic optimization: a reduction in drag leads to a reduction in the force resisting the vehicle from moving. This results in a lower required power output from the engine, and less fuel required to move the vehicle. In addition, drag and lift reduction improve vehicle stability and handling (Bearman, 1980). Drag and lift optimization typically focusses on having areas for the flow to attach or reattach to after separation from the vehicle body. The entire vehicle contributes to drag: separation off the rear contributes 25% of total drag observed; 33% of drag results from the wheels and wheel wells, and 10-15% of drag from the underbody (Howell et al., 2013).

These optimizations can focus on overall exterior shape such as height from the road surface, camber, tapering, and pitch (George, 1981). It was found that by increasing the camber of the vehicle body – angling up the rear section of an Ahmed body, akin to an aeroplane wing – lift and drag will have a slight but steady increase, with slightly quicker increases upon the formation of fast moving vortices that encourage diffusion of velocity. George (1981) also found that the body mean camber line – essentially the midway line between the upper and lower surfaces of the vehicle - has a direct correlation on lift, similar

to an aeroplane wing. On a model with tires and a “rough” underbody – an Ahmed body was outfitted with strakes on the underside to disrupt the flow – shows that a rough underbody will reduce lift and increase drag in comparison to the smooth underbody case with wheels. The wheels help to enclose the vortices, increasing downforce. In addition, lowering the car to the road surface increased the downforce. However, the angular resolution used in this study was fairly coarse angular so a finer resolution was more likely to improve the results and reinforce the trends observed.

Automobile aerodynamics can also be affected by additional aerodynamic devices such as spoilers, air dams and diffusers as exhaustively discussed by Katz (1992a, 1992b). A spoiler is a device made up of an upside-down aerofoil. An aerofoil typically it oriented in a way to cause faster moving air on top of it, and slower moving air under it, due to the difference in curvature of the surfaces or the angle the aerofoil makes with the air (i.e., angle of attack). This is done in order to create a resultant lift force based on the Bernoulli’s principle. Since positive or upwards lift is undesirable in the automotive industry due to reduction in grip they create, automotive spoilers are flipped upside down in order to generate increased levels of grip and control through negative lift, or downforce. Spoilers incur drag, due to skin friction resulting from slowing of air near a solid surface that creates a layer slower moving air than the freestream air called the boundary layer. In addition, drag can occur from the resultant force of the downforce, as at non-zero angles of attack there is a component of downforce acting against the direction of travel. Furthermore, spoilers are highly dependent on the flow separating and creating a wake. If the angle of attack is too high, the flow will not have enough momentum to follow the surface of the

aerofoil shape and therefore trails off to create a high-pressure wake, which increases drag and reduces downforce (Katz, 1992a).

Note that since a spoiler is finite in length, there is an alternate path for the air to travel around an aerofoil in addition to the flow direction; the air can flow from on top the spoiler to underneath it due to the lower pressure driving the flow. This creates vortices, which reduce downforce by having the high pressure air act on the wrong surface. Vortices increase momentum diffusion, however, and this property is used upstream closer to the leading edge of the flow in order to increase the momentum of the flow, preventing flow separation (Katz, 1992a).

Studies have also focused on “detail optimization” when improving the external body shape, such as the benefits of closed openings or rounded leading edges with regards to drag reduction (Hucho, 1993), where such optimizations saw drag coefficient improvements of -0.33. All of this research is typically done through two methods: experimental analysis or numerical analysis. Experimental analysis is conducted through wind tunnels. Wind tunnels are a time-honoured method of evaluating the aerodynamics of a vehicle; the first tests were conducted at the turn of the 20th century and tests are still done today to verify vehicle aerodynamics (Cooper, 1984). Wind tunnel velocity testing methods are numerous (Foss et al., 2004) and run the gamut from checking velocity with direct (anemometers) and indirect (hot wires, pressure probes) methods (Foss et al., 2004). Wind tunnel design and test setup has also been highly scrutinized, for example with research in the field debating the degrees of turbulence required for more realistic simulations. Cooper (1991) suggests that an improvement on traditional wind turbulence generation methods (such as having two grids in the flow path each moving in a single

axis) would be to incorporate the use of perpendicular V-shaped vane arrays that produce both the correct shape of turbulence and a low turbulent frequency. Using this vane array, the downstream turbulent velocity in the flow direction approximately 1.6m downstream was increased 400% compared to typical grid-based methods.

There are limitations in having a stationary ground while performing some wind tunnel tests. According to Hucho (1993) a fixed ground is adequate for the study of ground vehicles as long as the displacement thickness of the ground boundary layer measured in the empty test section is less than 10% of the vehicle's ground clearance. The effect of having a rolling road to simulate the relative velocity of the road to the vehicle and its effect on the boundary layer has also been investigated (Fago et al., 1991). With a rolling road, the drag coefficient was found to be relatively more constant at a variety of ground clearances compared to the stationary ground, with downforce showing a similar trend. In addition, the wake and recirculation downstream of the car is considerably elongated compared to the stationary case. Fago recognizes the limitations in his observations, noting that underbody roughness, internal flows and cross-winds may also have an effect. With the increasing convenience of numerical analysis, experimental analysis is often regulated to verifying numerical analysis because it is roughly what actually happens to the vehicle.

Numerical analysis is conducted done using Computational Fluid Dynamics (CFD). While experimental data is still held to the highest standard, CFD is accepted in early stages of research for the purpose of testing (Costa, 2003). It is also very useful in measuring variables which may be difficult to measure without disturbing the flow, such as pressure, velocity or temperature in a closed off space. CFD modelling techniques have been analyzed by others, with improvements suggested on which simplifications are allowable

for CFD analysis, the type of mesh used, the type of turbulence model, comparing different boundary conditions such as a rolling road, comparing the results using high power techniques such as Large Eddy simulation (Tsubokura et al., 2008) and more. Research done regarding the use of CFD in automotive aerodynamics discusses the trade-off between computational time versus the accuracy of the result (Lanfrit, 2005; Menter et al., 2003).

Modern methodologies of automotive aerodynamic analysis focuses on optimizing and automating the CFD process in order to reach upon an optimized solution faster and to utilize physical experiments more effectively. Lietz (2011) details an eight step process to approach this optimization. First, the aerodynamicist must create an analytical model and identify the factors to be studied, then identify which areas of the vehicle can be modified to produce a result desired limits – reductions in drag, in this case. The rest of the simulation parameters are setup (step 3) and then the simulation performed (step 4). The data is collected into a response surface for the fifth step, to determine the relationship between the multiple independent variables on a dependant variable. In this case, Lietz focuses on how multiple dimensions could affect drag, such as hood height, roof height, windshield angle, rear overhang, etc. Using the response surface, a virtual optimization is performed in order to reach a first iteration of an optimized design. In the seventh step, this design is simulated in order to confirm performance. Lastly, the data from the simulation is analysed (step 8). This methodology, while computationally expensive, will continue to improve with improvements in computational power and to the optimization algorithms.

2.2: Automotive Underbody and Underhood Aerodynamics

Exterior shape is not the only avenue of aerodynamic improvement; underhood flows also have been extensively researched. According to Renn and Gilhaus (1986), underhood

aerodynamic obstructions such as the radiator, fans, engine and accessories – collectively called underhood aerodynamics - contribute up to 10% of the overall vehicle drag; however difficulty in the trade-off between packaging, cooling and aerodynamics makes this a difficult area to optimize. There are a variety of studies looking at various aspects of underhood flow. Knaus et al. (2005) performed an investigation on the CFD codes that can be used throughout the design process, and how they can be used to optimize both the front end and cooling system design. The Behr Integrated System Simulation was identified as a one-dimensional (1D) simulation that analyses the entire system with standard objects. Underhood 3D is another solver that can only consider a limited geometry, but is easy to set up and leads to quick results. Star-CD is an all-purpose code that is highly accurate, but unstructured, leading to high meshing times. The intake geometry of a BMW 5 series sedan was studied using Underhood 3D and Star-CD. The simulations produced similar results with some minor differences in flow angles and depth. A maximum flow rate deviation of 13% was observed. In addition, different oil cooler configurations were studied to show the impact on flow distribution on the oil cooler and its efficiency. It was found that an oil cooler in front of the radiator increases its performance by 33% in the high speed operating condition because it has a much lower intake temperature than the behind-the-radiator case (Knaus et al., 2005).

Underhood design optimization methodologies have also been researched. Wille et al. (2010) detailed a CFD procedure to develop a vehicle through the design stages. This process was tested with a Porsche 911 Carrera and its inlet grills. CFD helps in these stages to determine the flow path. Once in the wind tunnel, the number of pressure probes and positioning has an effect on the pressure loss. To maintain constant flow inhomogeneity,

in order to resolve local gradients, at least 50 probes are needed – leading to a higher pressure loss across the radiator. Wille et al. (2010) found that 15 probes equally spaced around the radiator gave the best balance between pressure loss and inhomogeneity. Comparing the flow through the side inlets versus the center inlet across all of the tests, they determined that the 1D, CFD and wind tunnel measurements are close in detailing the difference in flow between the two configurations.

Barnard (2000) detailed a theoretical and practical approach to determining relationships regarding drag in automotive cooling systems. Theoretically, for low outlet to frontal opening area ratio, the core area to frontal area ratio should be as large as possible. His study tested the effects of cooling components on drag with an Ahmed body. The radiator was modelled by a wire mesh grid. It was observed that outlet geometry and size have an effect on the drag and velocity of the air, respectively. Various effects were theorized and tested, such as the influence of outlet aperture size, outlet geometry, placing a low pressure region in the back face (done with a blanking plate to cover half of the outlet), influence of inlet area and heat addition. The theoretical models correlated well with the experimental data. It was also found that the drag was lower for a smaller area and at a non-horizontal exit angle, as predicted. In addition, the drag reduced with the introduction of the low pressure region at the exit, though it was difficult to model as the change in pressure coefficient was not known. Inlet area, as detailed in the theoretical derivations, had little effect on the drag.

Improvements of underhood testing methodologies have been investigated, similar to improvement in testing external flow. Propeller anemometers, while often used, have high errors in shear flow. Ng et al. (2002) developed a pressure-based technique to evaluate

vehicle aerodynamics. Their technique measures the total pressure on the front of the radiator and the static pressure on the back of the radiator (done by facing the rear probe opposite the flow on the rear face of the radiator). The setup was tested against a propeller anemometer array in various test setups such as having the fan and shroud installed, the fan running, an air dam installed and blocked and an unblocked grille. The flow was visualized with wool tufts. Similar flow patterns when compared to the propeller anemometer were recorded, with an average 23% variance between the propeller anemometer and pressure. This difference was attributed to the large propeller anemometers used, which lack accuracy, and spatial resolution.

Despite the large grill openings at the front of the car, the fan still dominates the flow pattern underhood. Siqueira et al. (2002) reported a numerical simulation using the CFD program Star-CD of the underhood flow for a DaimlerChrysler truck with the purpose of establishing a precedent for future studies during the concept phase of vehicle design. The truck was analysed under two conditions; with the truck at a standstill with the fan running and with the truck moving when the engine is producing maximum torque with the fan running. The heat exchangers (radiator, condenser, and intercooler), engine, fan and cabin truck were modelled for this study. The results indicated that for both test conditions the flow pattern under the hood are very similar, showing similar regions of recirculation and flow re-attachment. These explained that the fan influences flow the most under the hood, so the flow looks similar in both cases.

Compared to the rest of the field, research on underbody aerodynamics is limited, being far outclassed by underhood and external aerodynamics. Air dams are used to reduce the amount air going under the car. These air dams have been well proven to increase the

downforce due to the decrease in pressure underneath the vehicle (Katz, 1992b). Diffusers are used to modify the flow under the vehicle by accelerating it at the entrance of the diffuser and slowing the flow down at the exit of the diffuser. Slowing down the air, as discussed earlier, increases its static pressure and thus reduce pressure drag. Designing diffusers with sharp edges helps to create strong vortices off of the edges thus encouraging the flow to remain attached to the diffuser (Katz, 1992b).

The majority of underbody analysis is split into two distinct methods: research on highly generalized vehicle models, such as the Ahmed body (Jowsey and Passmore, 2010), and research on specific vehicle models. For example, a study reported a general design guideline for the optimal dimensions and geometry of an automotive underbody diffuser for low drag and high downforce using an Ahmed body (Jowsey and Passmore, 2010). They performed experimental studies, suggesting diffuser angles between 13-16 degrees for single-channel diffusers and 16-19 degrees for multiple channel diffusers. It needs to be reiterated that this is optimized for an Ahmed body.

Alternatively, research can focus on improving existing vehicles. For example, Kang et al. (2011) reported on the design of an active diffuser that changes shape depending on velocity, resulting in an improvement of up to 4% drag reduction on a specific Hyundai model. Further underbody aerodynamic research involves improving the understanding of features such as the flow in wheelhouses and around the tires (Regert and Lajos, 2007), and optimizing the Ahmed Body (Beaudoin and Aider, 2008). The common theme in underbody aerodynamic research is to reduce overall drag and increase downforce as optimizations with the exterior shape and underhood are becoming more marginal. In addition, there is plenty research that focusses on coupling thermal and aerodynamic

research in the underhood, due to the high cooling demands of the engine. There are also some components under vehicles that require cooling (e.g., differentials, battery packs). However, there is no real focus on how to link underbody aerodynamics to the thermal demands of these underbody components.

2.3: Aero-thermal Research

The engine and related components, such as battery packs, differentials, heat exchangers, etc. have cooling demands that are met through air-to-air or air-to-fluid cooling (Talom and Beyene, 2008). This field is called aero-thermal research. The majority of research in the field focuses on the underhood layout for optimizations. This is largely due to the vast improvements that can be made in these areas with respect to drag reduction and control of underhood temperatures. Later studies looked at the interaction between external and underhood flow. Costa (2003), explained how computational fluid dynamics (CFD) can help with the positioning of components, exterior design, and powertrain cooling system design. His study detailed a method to analyse and improve underhood thermal management in vehicles using CFD tools. There are many different CFD codes used in the industry; however Costa focused on Underhood 3D, a Ford Motor Company proprietary program. This study reviewed the front end design of a variant of a small SUV, using the original design as a base and optimizing the under hood flow. The final design utilized an air dam under the radiator to create a low pressure region behind it to remove the hot air from the cooling pack and an air deflector in the hood to direct the flow into the intake. By the CFD analysis, these improvements reduced the underhood temperatures by 20%.

Kuthada and Wiedemann (2008) reported recent discoveries regarding drag as observed from an integrated numerical and experimental approach. A baseline investigation was

performed on the vehicle, showing that the cooling airflow at the front of the vehicle changes the drag the most, though the force generated by the heat exchangers (the charge-air cooler, AC condenser and radiator in this study) is only a small percentage of the total change. The investigation of the rear end shows that different shapes (notchback and a squareback) had different cooling air drag values, independent of the cooling air flow speed. Kuthada and Wiedemann (2008) also tested whether a moving ground experiment has an effect on cooling air drag. When considering a road simulation, the effects of the different rear end designs on drag and cooling air pressure are minimal.

Nobel and Jain (2001) proposed a design methodology to improve the efficiency of underhood thermal management design using CFD techniques. With this simulation, learning where components should be located in the underhood can be determined early in the process when physical prototypes may not yet exist. Importing models from Unigraphics into Fluent, one must define the boundary conditions for the problem in order for Fluent to use the linearized Navier-Stokes equations. Despite the relative ease of modelling the underbody components like exhaust piping or gas tanks, some components, like the radiator, are not fully modelled because of the high level of detail required. Instead, the radiator is treated like a porous material, with macroscopic cells representing the varying temperature (and thus heat distribution) along the core. CFD can also model the fan by using the multiple reference frame method to consider the rotation of the fan as well as any translation and velocity in the frame itself. The modelling methodology was demonstrated on a large international heavy-duty class truck. The CFD results compared favourably with the experimental data. The pressure drop was up to 6 Pa higher, the heat

rejection being 4% lower and the charge air cooler temperature was 9K lower in the CFD model (Nobel and Jain, 2001).

In a much smaller scope of work, underhood research has also looked at the effects on the surrounding conditions that affect the underhood aerodynamics, such as road inclination. Khaled et al. (2010) reported on using simple models to determine the underhood temperature distribution at different inclinations. The vehicle was raised in the rear 1 cm for the downhill condition, and raised 1 cm in the front for the uphill condition. These models were then verified against wind tunnel measurements where the vehicle was instrumented with 80 thermocouples and 20 fluxmeters to measure component temperatures and air temperatures. This study aimed to capture the temperature and total (convective and radiative) heat flux underhood at constant-speed driving, slow-down and thermal soak phases of each thermal functioning point. The error between the experimental and predicted results for the temperatures and heat flux are 3.6% and 3.7% respectively.

Another study investigated the ambient effects such as varying humidity, turbulence and cross-winds on a Chrysler vehicle (Lan and Srinivasan, 2009). Despite standardized thermal road trip tests, the inlet air velocity profile and ambient temperature conditions change dramatically, affecting the thermal conditions of the vehicle. The analysis was conducted using CFD to study the free stream effects, with the goal of understanding prototype results more accurately in addition to improving future CFD modelling by selecting appropriate boundary conditions. The study looked at 10 underhood and underbody components; two in front of the engine, five behind the engine, one at the mid-underbody, and two at the rear underbody. A standard $k-\varepsilon$ turbulence model is used. A baseline model was established with an ambient air temperature of 42.2°C, and the

turbulence intensity and length scale at 1% and 0.33m respectively. Following this, ambient temperature, turbulence intensity, length scale, tail winds, perpendicular cross winds, and blockage ratio (defined as frontal area as a ratio of wind tunnel area) were varied and studied. Ambient temperature, tail wind speed and turbulence intensity has a direct correlation with underhood and underbody temperatures; increasing either ambient temperature, tail wind speed or turbulence intensity leads to an increase of component temperature. Turbulent length scale and perpendicular crosswind have little effect on component temperatures. However, blockage ratio has an inverse effect on temperature. For cross-winds studies the focus is more on larger, broadsided vehicles where more effects can be felt, such as trains and transport trucks (Baker, 1991a; 1991b; 1991c). For specific passenger vehicles, such as the one studied in this thesis, specific research is much more limited.

Lin et al. (1997) studied the effects of crosswinds on engine cooling through the Specific Dissipation parameter. The car engine was not in operation but a hot coolant was cycled through the radiator to simulate it. Thermocouples measured the inlet and outlet temperature of the coolant. The test was performed in 5 degree increments from 0 to 20 degrees on three different vehicles, at relative wind velocities of 14, 19, 28 and 33 m/s. Specific Dissipation was used to measure how crosswinds affect the engine cooling system. Specific Dissipation is as follows (Lin et al., 1997):

$$SD = Q/(T_{hot,in} - T_{cold,in}), \quad (1)$$

where $T_{hot,in}$ and $T_{cold,in}$ are the hot and cold fluid inlet temperatures of the heat exchanger, and Q is the heat exchanger heat transfer rate. The overall trends observed are that the front

end configuration and angle affects the heat dissipation, with dissipation decreasing with angle. The Specific Dissipation increases with velocities tested, with a maximum decrease in on car of 13% at the maximum yaw and velocity (33 m/s and 20 degrees yaw). On-road tests were also conducted, which confirmed the experimental results.

2.4: Electric Vehicles and Battery Cooling

Electric vehicles are propelled by electric motors as opposed to typical gas-powered vehicles. However, the distance an electric vehicle can travel when fully charged is severely limited compared to a traditional gas-powered vehicle. This is due to the limited battery energy density (Chan, 2007). This has led to the development of hybrid electric vehicles. Hybrid electric vehicles combine the powertrains of an electric vehicle and gas vehicle (Chan, 2007). An electric motor can be combined in series with the gas engine, where the engine acts as a generator for the electric motor. The electric motor can also be in parallel with the gas engine, where propelling the vehicle can come from power from either of them or a combination of both. More complex hybrids can result from additional generators or energy recouping methods. Hybrids can be categorized per power level generated by the electric motor, or by electric energy replenishment methods (Bitsche and Gutmann, 2004). The main issue with hybrids is the challenge of cooling battery packs. The battery packs consist of numerous cells that store and discharge energy to drive the electric motor depending on the driving demands. The charging and discharging rates of a cell depend on the temperature of the individual cell. However, the energy requirements from the vehicle apply to the whole battery pack. If an individual cell is charging at a different rate because of a localized temperature increase, this could lead to overcharging

the cell resulting in damaging it. This therefore reduces the capacity of the battery (Pesaran, 2001).

To prevent these temperature localizations, the batteries are also required to be maintained at a consistent and uniform temperature. Various cooling methods are being explored, such as air cooling, liquid cooling and phase change materials. Air cooling is simply done with air blowing over the modules. Air cooling methods have focused on using fans to influence the air. Passive air cooling refers to not heating or cooling the cabin air before it enters the battery. Active cooling takes fresh cooling air from outside the vehicle through an auxiliary air heating/cooling system first in order to send the air to the battery at an appropriate temperature (Rao and Wang, 2011). Heating a battery is important because batteries should be within an operating range. The ideal range for a lithium-ion (Li-ion) battery pack is between 25°C to 45°C (Pesaran et al., 2003). Liquid cooling can have a specially designed battery with jackets between each of the cells or a jacket around all of the modules, or direct contact with a non-conductive fluid. While the heat transfer rate of liquids is generally much higher than air for a given mass flow rate, the associated increase in viscosity and the resulting increase in required pumping power to circulate the cooling fluid generally reduce mass flow rates for liquid cooling. Thus liquid cooling generally is only 150%-300% more effective than air cooling (Pesaran et al., 2001).

Use of external aerodynamic devices such as diffusers to treat the air and influence the incoming cooling air is limited. Air cooling methods primarily focus on channelling the air through the battery pack cells to maximize the effectiveness of the cooling mechanism. Park (2013) for example, numerically evaluates the design of six different tapered air manifold inlet and outlet designs for a battery pack with multiple cooling passages

throughout the battery. He observed a nearly 70°C reduction in temperature with the optimized design, which had an added ventilation duct, and only an 18°C temperature difference throughout the battery pack.

Pesaran et al. (1999) reviewed a battery pack cooling system design methodologies. To begin designing a battery thermal management system (BTMS), the designer should follow a systemic approach where the design goals are first clearly detailed, such as desired temperature, temperature difference, component sizing, etc. The heat generation of the module should be estimated or measured, at which point initial numerical analysis can begin to determine temperatures, flow rates (if internally cooled), pumping power required, or whatever is of focus. With the initial results, prototyping, both on-bench and on a dynamometer, should follow to confirm the numerical analysis, with optimization from lessons learned in prototype testing. Attention must be paid to vehicle constraints; similar to aerodynamic optimization, BTMS design is highly dependent on packaging with drastic design changes (such as having to move from air to liquid cooling) possible depending on the amount of room available for the system. As a rough guideline, parallel HEVs can suffice with air-cooling, likely due to their smaller battery size, whereas series HEVs and EVs require the more robust cooling liquid cooling provides (Pesaran et al., 1999).

A well-known issue with air cooling is the resulting temperature gradient in the battery that occurs as the air continues to move downstream. As the air heats up as it moves downstream it becomes less effective at extracting heat from the battery. Research has found that by reciprocating the air – that is, having the air alternate the sides it enters the battery to begin cooling it – can reduce cell variance by 4°C or 72% (Mahamud and Park, 2011). An alternative approach which may offer some benefits in addition to internal air cooling of

the battery is to look at external cooling of the battery pack. External cooling in this context implies exposing a surface of the battery pack to the incoming air from under the vehicle. By externally cooling part of the battery, it could potentially reduce cooling by forced convection and hence reduce the associated energy usage.

Overall, the gap in research appears to be the link between underbody temperature and cross-winds for various underbody devices. Aerodynamic research typically focusses on the exterior body for improvements, and research that does link aerodynamics and thermodynamics focuses on the underhood region with the high cooling demands from the engine, not under the body. This is despite heat producing devices underbody such as a battery pack in an EV or HEV. Furthermore, cross-wind research aerodynamically is limited, and no research found linked cooling of any kind to yaw angle, only pitch. Thus the following research looking at the aero-thermal effects in yaw fills an existing gap in open literature.

Chapter 3: Methodology

The methodology for this thesis comprises of two approaches: the experimental measurements, and the numerical simulation. Experiments were conducted in the wind tunnel. The temperatures were monitored with thermocouples. Go-pro video cameras were used to record the underbody flow pattern using flow visualisation tufts. For the numerical analysis a CAD model of the vehicle was created in NX. This model was imported to the meshing program ICEM in order to discretize the domain, in which the solver Fluent was used to perform the calculations of the case. The results were post processed to visualize the velocity and temperature results in order to compare to the experimental data and to provide further insight into the velocity and temperature results.

3.1: Experimental Measurements

3.1.1: Experimental Test Facility

The tests were conducted in the climatic wind tunnel (CWT) in the Automotive Centre of Excellence (ACE) at the University of Ontario Institute of Technology (UOIT). The CWT is the world's only full-range CWT that incorporates a dynamometer in a large turn-table for yaw testing. The vehicle was mounted on the 11.7 m turntable and the dynamometer. The nozzle of the wind tunnel can be expanded from a minimum of 7 m² to a maximum of 13 m² in order to test a variety of vehicle sizes and shapes at a maximum speed of 250 km/h. The climatic aspects of the wind tunnel range the gamut from a 100 °C temperature range (from -40 °C to 60 °C), relative humidity from 5-95%, a solar array to simulate the sun, and the capability to simulate driving or falling snow or driving rain (Best et al., 2013).

The CWT was designed with a boundary layer removal system to reduce the size of the boundary layer for all possible configurations. For example, the final design resulted in a boundary layer only approximately 100 mm thick at 7.5 m away with the nominal nozzle size (9.3 m^2) and a wind speed of 100 km/h (Best et al., 2013). In addition, the air exiting the nozzle is highly uniform; the static pressure variance across the nominal nozzle area is only 0.01 Pa and the temperature variance is a maximum of $0.2 \text{ }^\circ\text{C}$ (Best et al., 2013). The displacement thickness 2 m from the inlet entrance is only 5 mm tall, far less than the 300 mm ride height of the vehicle and thus acceptable by Hucho (1993).



Figure 3.1: The test vehicle inside the climatic wind tunnel.

The 2005 Chevrolet Aveo5, which is the test vehicle, was tested at two different temperatures, $10 \text{ }^\circ\text{C}$ and $50 \text{ }^\circ\text{C}$, two wind speeds of 50 km/h and 100 km/h, and five different yaw angles: -29.2° , 0° , 8° , 15.6° , and 29.2° . The vehicle was strapped down to the turntable using ratchet straps at the rear of the vehicle while at the front of the vehicle aircraft cable was used to anchor the vehicle down to prevent it from lifting while exerting minimal aerodynamic interference. Testing was done at various yaw angles in order to

further the understanding of the flow-field in cross-winds given the previously noted limited research currently available. Because of the large yaw angles involved in the test, the 13 m² (2.9 m × 4.5 m) nozzle was used for the tests. Figure 3.1 is a picture of the test vehicle in question in the climatic wind tunnel.

3.1.2: Experimental Test Vehicle Instrumentation

The test vehicle was outfitted with a hotplate affixed to the gas tank under the vehicle as shown in Fig. 3.2. The hotplate measured 20 cm long by 20 cm wide by 2.5 cm thick and was made of aluminum. Four K-type thermocouples were embedded at each edge of the plate at approximately half the depth of the plate (12 mm) to record the temperature. Based on preliminary tests the power supplied to the hotplate was limited to 1000 W to avoid melting of the car's gas tank which was made of acrylonitrile butadiene styrene.

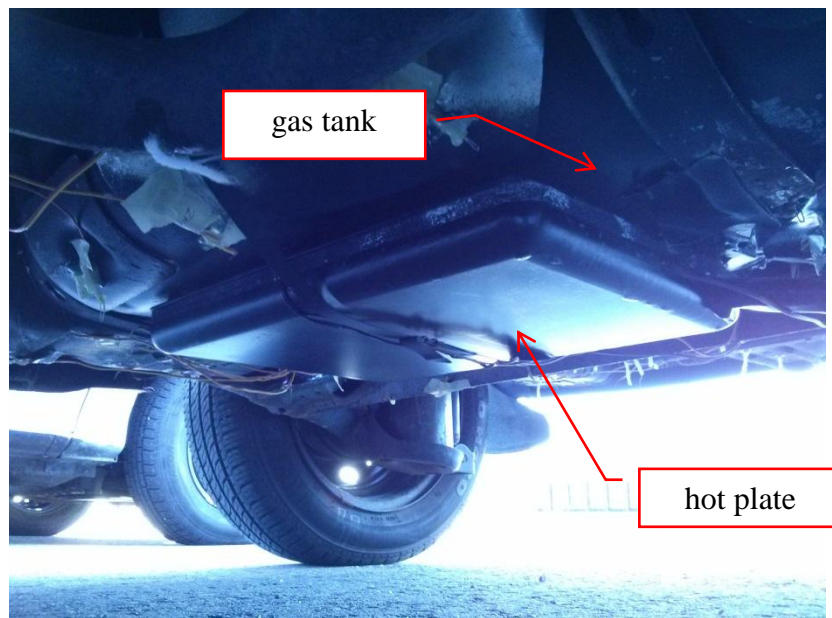


Figure 3.2: The hot plate attached to the gas tank under the vehicle.

In all 137 K-type thermocouples were installed around the hotplate and vehicle underbody to measure the temperature distribution and changes due to the wind. These thermocouples

have an error range of 2.2 °C (Ripple, 1995). A square array of thermocouples 10 cm apart covering the vehicle's underside from the front axle to the back side was used. Finer arrays of thermocouples at 3 cm apart were used around the hotplate as shown in Fig. 3.3 for better capture temperatures close to it. All the thermocouples were placed 5 mm away from the surface of the underbody so they are approximately inside airflow boundary layer. A few thermocouples were located at the radiator, hood, front bumper, side-view mirrors, the centre of the roof, in front and behind the rear wheel wells for reference. The thermocouples were connected to a bank of nine Ipetronik M-Thermo K-type 16 channel modules. These modules were then connected to a data acquisition system called TALENT Test Automation System supplied by ReACT Technologies Inc. The thermocouples were calibrated and each one checked in advance of the test by comparing their temperature readings to a known temperature. Figure 3.3 shows the position of the instrumented thermocouples under the body.

Two Aeroprobe 5-hole pressure probes were also used to measure the wind speed and direction; one at the driver side of the vehicle and the other at the passenger side. The probes were mounted at the distance of 10 cm from the underbody surface. They were located approximately 1860 mm downstream of the front axle of the car. The driver side probe was approximately 30 cm from the driver side edge of the car while the passenger side probe was approximately 65 cm from the passenger side edge of the car, as shown in Fig. 9. In addition, tufts of approximately 5 cm long and 3 mm wide were affixed to the underside of the vehicle for flow visualization.

An infra-red camera (model IRXP 5000) with a wide angle (61.9°) lens was used to measure the surface temperature of the hotplate to compare with the data from the

embedded thermocouples in the hotplate. This infra-red camera was mounted in a custom window in the turntable under the vehicle. A second custom window was made in the turntable for three video GoPro cameras for the flow visualization. The three cameras have the following specifications: One GoPro Hero Camera with 1280×960 pixels resolution and 170° angle of view and two Go-Pro Hero 3 Cameras with 1280×960 pixels resolution and of 149.2° angle of view.

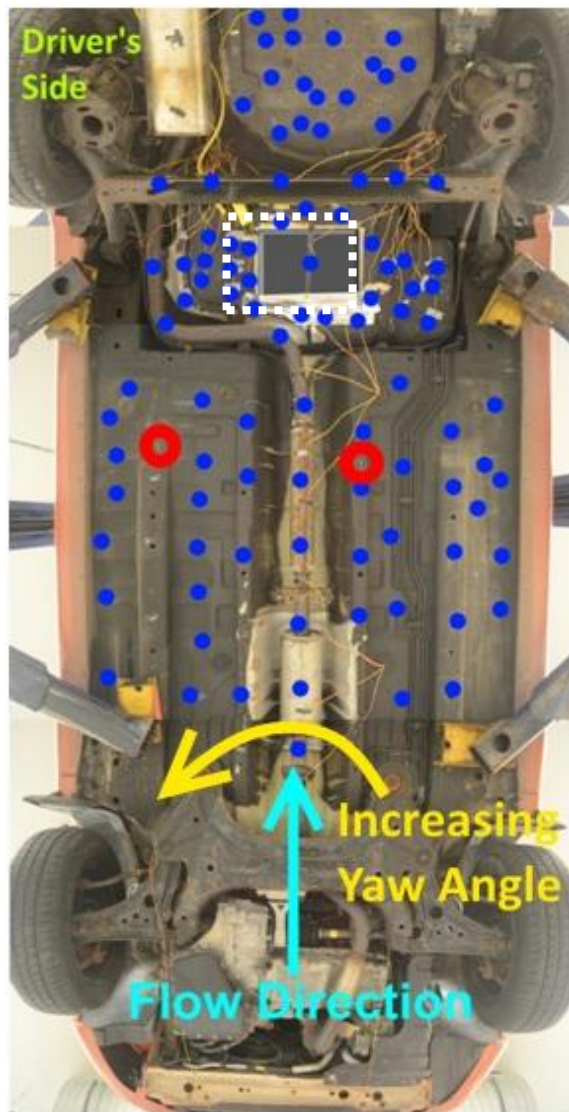


Figure 3.3: The vehicle underbody, showing the flow direction, position of the hotplate (dotted line rectangle), and thermocouples (dots) and probes (circles). The left side is the driver's side.

3.1.3: Test Matrix

The experiments were conducted at a variety of yaw angles, wind speeds and tunnel temperatures. Table 1 contains the detailed test conditions including 18 tests in all.

Table 1: The test matrix. Tests marked with a * indicates non-rotating wheels for that test.

Test	Road speed (km/h)	Yaw angle (deg)	Test section temperature (°C)
1	50	0	10
2		15.6	
3		29.2	
4		-29.2	
5*	0	0	
6	100	0	
7		8.0	
8		15.6	
9*	0	15.6	
10	50	0	50
11		15.6	
12		29.2	
13		-29.2	
14*	0	0	
15	100	0	
16		8.0	
17		15.6	
18*	0	15.6	

3.2: Numerical Simulation

3.2.1: Numerical Introduction

The flow in this study is predominantly turbulent. Although analytical solutions for turbulent flows are not yet possible, on the basis of the continuum fluid assumption, the dynamics of turbulence is adequately described by the continuity and Navier-Stokes equations. Approximate solutions of the Navier-Stokes equations can be obtained using numerical methods known as Computational Fluid Dynamics (CFD). The solution is implemented by generating a mesh of the region of interest or domain. This is done by subdividing the domain into a set of discrete volumes and points. The governing equations are then discretized yielding a system of algebraic equations which can be solved at each point within the domain. In this thesis, the goal of the CFD study is to obtain trends that can be compared with the experimental measurements. In addition, because the experimental technique obtained only point-wise data the CFD technique provides the whole field and comprehensive data to complement the experimental data.

3.2.2: Governing Equations

As mentioned earlier, the air flow is turbulent and therefore requires the use of the Reynolds-Averaged Navier-Stokes Equations (RANS). Since the temperature field is also of interest, the Reynolds-Averaged Energy equation is solved as well.

$$\nabla \cdot \bar{\mathbf{V}} = 0 \quad (2)$$

$$\rho \left(\frac{\partial \bar{V}}{\partial t} + (\bar{V} \cdot \nabla) \bar{V} \right) = -\nabla \bar{p} + \nabla (\mu \nabla \cdot \bar{V} - \lambda) \quad (3)$$

$$\frac{\partial \rho T}{\partial t} + \nabla \cdot (\rho \bar{V} T) = \nabla \cdot \left[\left(\frac{\mu}{Pr} + \frac{\mu_t}{Pr_t} \right) \nabla T \right] \quad (4)$$

The air in the simulation is assumed to have ideal gas behaviour, for which the equation of state can be written as,

$$\rho RT = W(p + p_{ref}) \quad (5)$$

Since the flow in the problem is assumed to be fully turbulent an appropriate turbulence model is required. In this study, as mentioned earlier the eddy viscosity-based Shear Stress Transport (SST) turbulence model available in ANSYS Fluent was employed because it combines the strengths of the standard k - ω and k - ε models. The equations in Fluent for turbulent kinetic energy and eddy viscosity are as below:

$$\frac{\partial \rho k}{\partial t} + \nabla \cdot (\rho \bar{V} k) = \nabla \cdot \left[\left(\mu + \frac{\mu_t}{\sigma_k} \right) \nabla k \right] + P_k - C_1 \rho k \omega \quad (6)$$

$$\frac{\partial \rho \omega}{\partial t} + \nabla \cdot (\rho \bar{V} \omega) = \nabla \cdot \left[\left(\mu + \frac{\mu_t}{\sigma_\omega} \right) \nabla \omega \right] + \alpha \frac{\omega}{k} P_k - C_2 \rho \omega^2, \quad (7)$$

where C_1 , C_2 , α , σ_k and σ_ω are the model constants, and the eddy viscosity is related to the turbulent kinetic energy and the eddy frequency as follows.

$$\mu_t = f(k, \omega) \quad (8)$$

The commercial CFD software Fluent was used in this study because of its flexibility and availability. Starting from an initial condition the solution is marched towards a steady-

state. Convergence is judged against the normalized continuity, momentum and energy residuals and is considered converged when these residuals have been reduced to 1×10^{-6} .

3.2.3: Geometry and Boundary Conditions

This study investigates a steady-state air flow and temperature distribution around a test vehicle in ACE's climatic wind tunnel. A steady state simulation was performed in order to simulate the typical highway condition, where a vehicle is travelling at a relatively constant velocity. The full geometry is depicted in Fig. 3.4. The full scale wind tunnel and vehicle were simulated. The dimensions of the wind tunnel or domain are 13.5 m wide by 7.5 m tall by 20.1 m long.

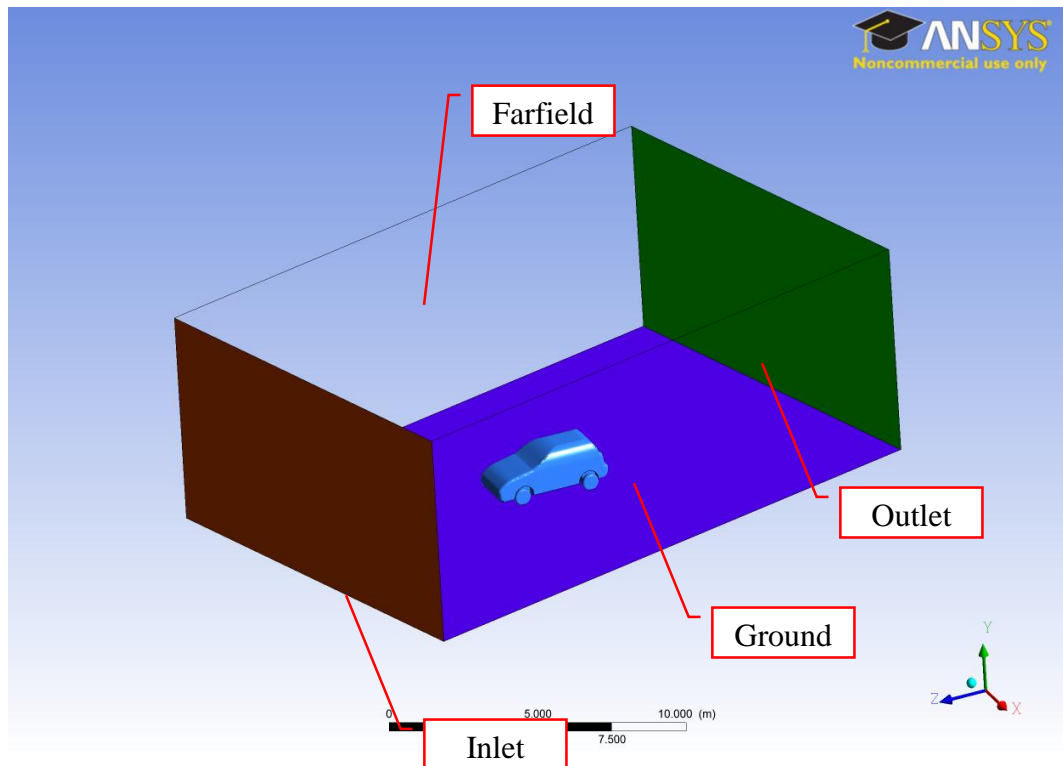


Figure 3.4: Schematic of the simulation domain with the vehicle inside it for the 15 yaw case.

In a CFD simulation the term "wall" refers to any solid surface that the flow cannot penetrate and thus includes the walls, the floor, ceiling, and surfaces of the test vehicle. The following is a summary of the boundary conditions that have been applied to the model. The no-slip boundary condition is applied to the floor and all surfaces of the test vehicle. A constant average temperature was applied to the hotplate. The inlet velocity must be specified to obtain the desired value of Reynolds number. Two velocities were tested. A uniform wind velocity of 13.9 m/s (50 km/h) was used for the 0 and 29.2 degree yaw tests in order to further understand and visualise the flow. For the 8 and 15.6 degree yaw tests, 27.8 m/s (100 km/h) was used as the wind speed to investigate the interesting experimental trends observed that will be discussed in Chapter 4. Both these values were chosen to be consistent with the experimental values used; the velocities were specified in absolute terms relative to the origin. The Reynolds number was based on test vehicle length of 2.48 m and viscosity of the air was $Re = 2,282,349$ for the 50 km/h test and $Re = 4,564,698$ for the 100 km/h test. In addition, the inlet turbulence intensity was set to 1% as suggested by Lan and Srinivasan (2009) and from expert advice from Aiolos engineers about the turbulence in the wind tunnel they designed. The outflow condition was specified as zero relative pressure at the domain outlet. The other boundary conditions include specification of pressure at the outlet plane (Fig. 10), 10°C ambient temperature at all surfaces aside from the hotplate (which was specified at the average of the four thermocouples embedded in the hotplate). The pressure boundary condition was implemented by setting the pressure gradient to zero at the outlet and the surrounding walls including the ceiling.

For the underbody battery pack cooling cases, all cases were analyzed at a wind speed of 100 km/h. This is to approximate the highway cruise condition, in which air cooling would be effective due to a higher convective heat transfer rate. The heat flux specified from the battery pack surface was 245 W/sq.m, as suggested by Park (2013). The surrounding walls were set to a pressure outlet with a zero target mass flow rate and the outlet was set to a pressure outlet where the solver calculates the mass flow rate. The inlet air temperature and ambient temperature were both specified as 300K.

3.2.4: Mesh Generation

The meshing of the domain is a very important step since various meshing parameters, such as the number of nodes and the shape of the elements have a significant impact on the accuracy of the results and the numerical behavior of the solution. A fine unstructured tetrahedral mesh was generated using ANSYS ICEM to resolve all flow features of interest. This process was repeated for the different angles outlined in the test matrix above and for the diffuser tests.

The diffuser was designed to be a single channel diffuser at the optimal angle of 14.5° as suggested by Jowsey and Passmore (2010). The mesh resolution at various locations within the geometry is shown in Fig. 3.5. Flow along the various surfaces in the space is resolved by using a finer mesh size around those obstacles while the boundary layers along all surfaces are resolved by clustering 10 layers of prismatic elements near the walls (shown in Fig. 3.6). The prismatic layers are also adjusted such that the first node is 0.6 mm away from the wall. This wall node spacing yields a dimensionless wall distance of $y^+ \leq 11$, where y^+ was chosen to be 11. This value is consistent with the recommended value for

SST turbulence model (ANSYS, CFX-5 Manual). The total number of elements used for the mesh is approximately 20 million.

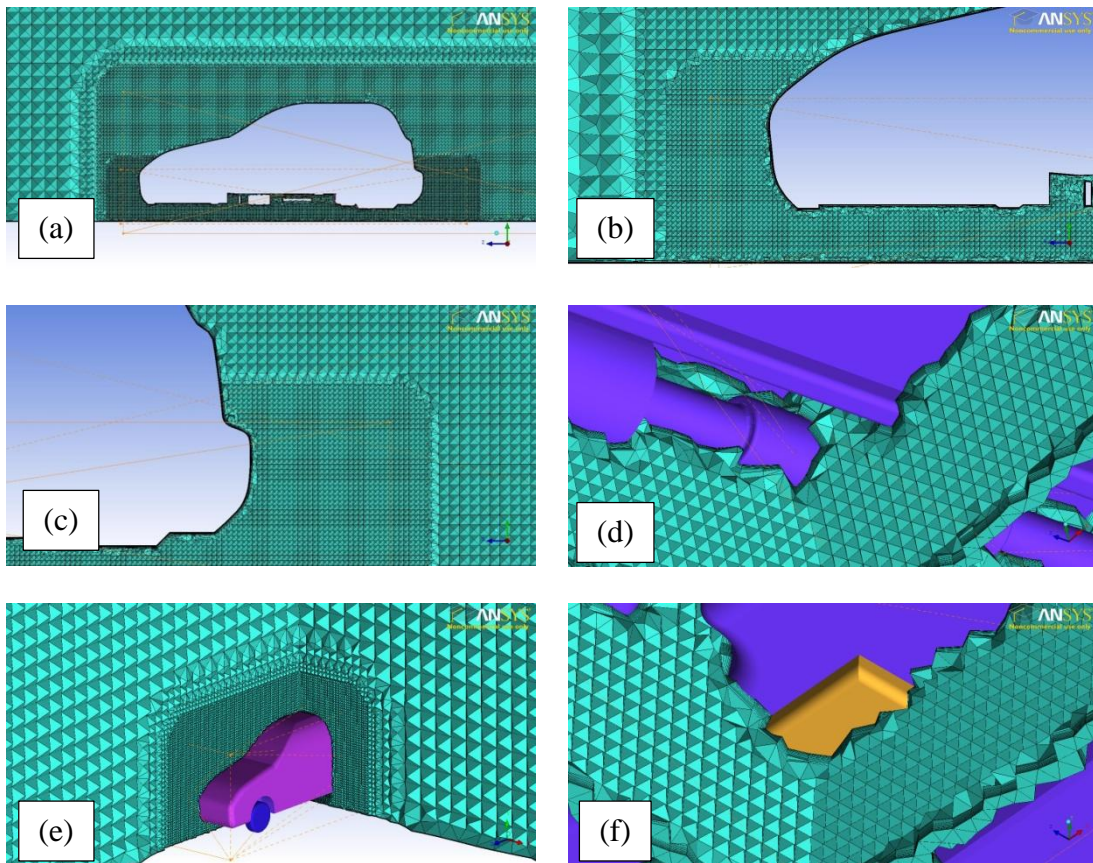


Figure 3.5: Unstructured tetrahedral mesh. (a) side view of the car, (b) close up side view of front of the car, (c) close up side view of rear of the car (d) close up view of exhaust piping with two cut planes, (e) front view of the car with two cut planes, (f) close up on the hot plate with two cut planes.

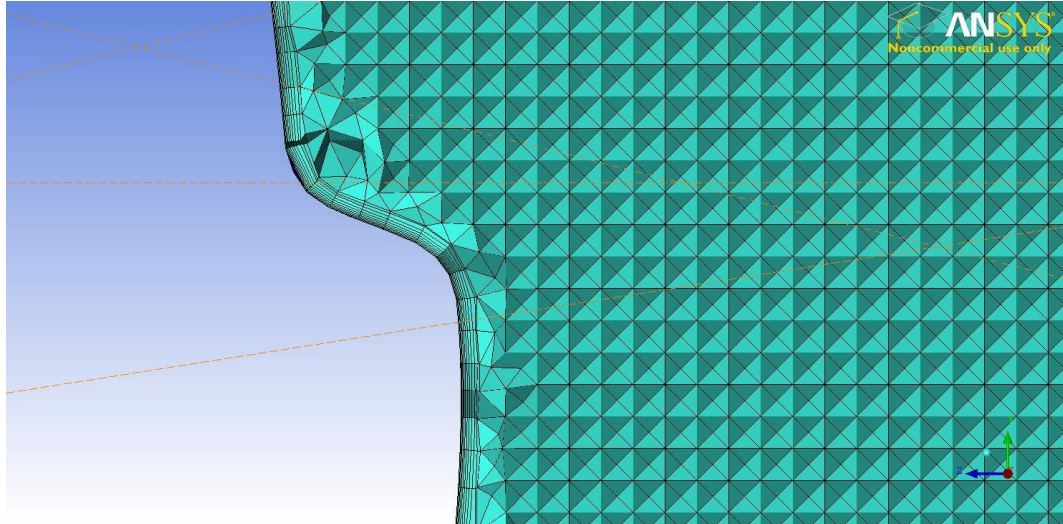


Figure 3.6: Prism layers on the trunk of the vehicle.

The quality metric used by ICEM is calculated such that perfectly regular elements have a quality value of 1, while values close to zero indicate degenerate elements. In practice a mesh that is composed of elements above a quality of 0.2 is considered acceptable (ANSYS, CFX-5 Manual). The quality histogram is shown in Fig. 3.7 along with the node and element counts for the mesh. From the histogram shown below it is evident that less than 0.1% of the elements have a quality below 0.2 implying that the quality of the mesh is good and therefore appropriate for this study.

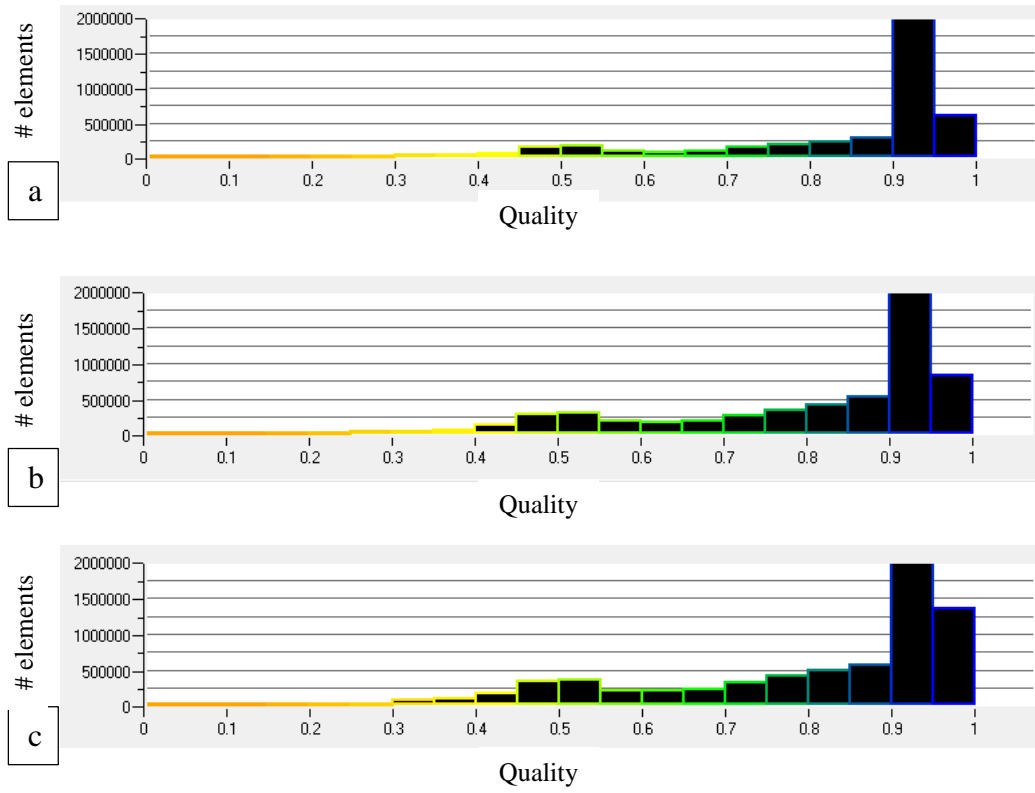


Figure 3.7: Quality histogram for the a.) 0 yaw, b.) 8 yaw, and c.) 15 yaw meshes. Horizontal axis is the quality, and the vertical axis is the number of elements at a given quality.

Chapter 4: Results and Discussion

In this chapter, the data obtained through experiments and numerical simulation are analyzed and discussed. The chapter is divided into three main sections consisting of experimental and numerical results. Section 4.1 discusses the experimental results comprising velocity and temperature distributions of the underbody of the Aveo5 at various yaw angles. The numerical simulation results are discussed in Section 4.2. This section focuses on the velocity and temperature distributions of the underbody of the Aveo5 at various yaw angles to complement the experimental results in regions where it was impossible to obtain data experimentally. Finally, Section 4.3 discusses the numerical analysis performed in understanding the effect of an underbody diffuser on the cooling of a battery pack.

4.1: Experimental Results

4.1.1: Temperature Distribution of the Hotplate

For each test the infrared thermal imaging cameras were used to record images of the temperature distribution on the hotplate. Fig. 4.1 is comprised of images of temperature contours of the hotplate for the four selected test conditions indicated. Note that the vertical strip on each image is not part of the hotplate but rather the location of the strap that was used to fasten the hotplate to the underside of the car.

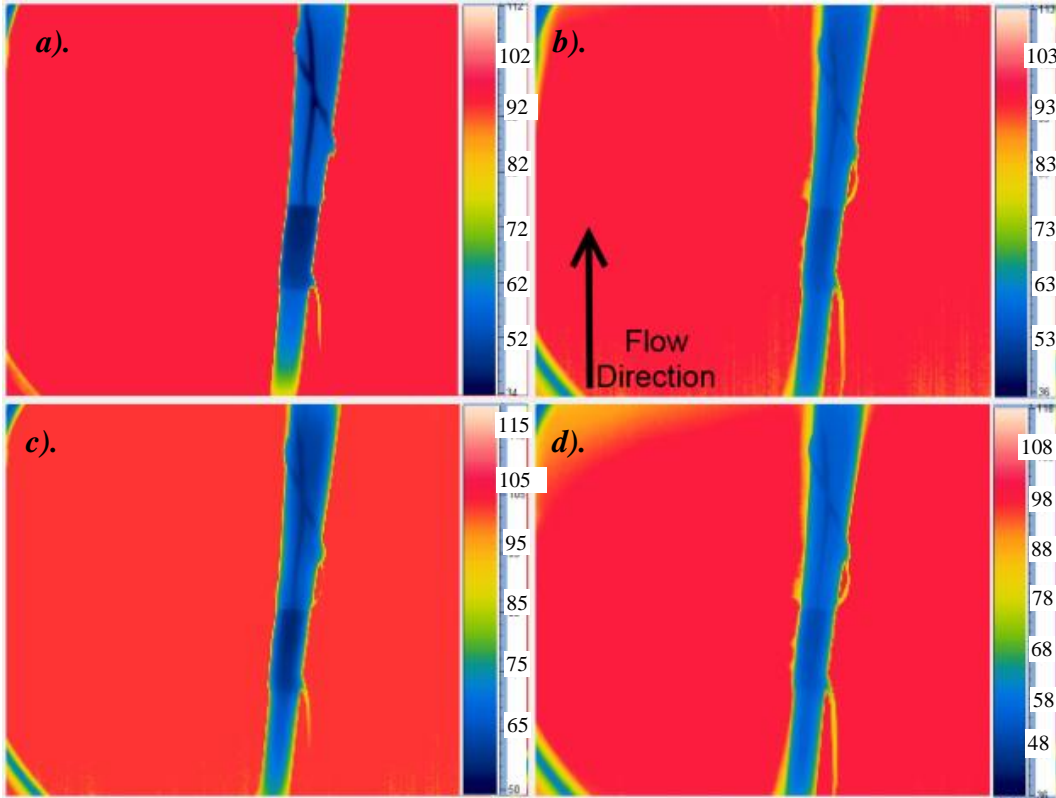


Figure 4.1: Temperature contours of the hotplate at selected test conditions seen by the infra-red thermal camera. (a) 0° yaw, (b) 8° yaw, (c) 29.2° yaw and (d) 15.6° yaw.

The figure shows that in general the temperature of the hotplate is uniform over the entire plate. The variations among the contours are within 10%. This is therefore consistent with the design requirement. In addition, four thermocouples were embedded inside the hotplate along the middle of each side: ET1, ET2, ET3 and ET4 (see Fig. 4.7), respectively for monitoring the temperature. These thermocouples were used to determine the steady state. The temperature values of the thermocouples are plotted as shown in Figs. 4.2 and 4.3 for two selected test conditions. Figure. 4.2 and 4.3 show that the temperature of these imbedded thermocouples is consistently higher than the surface temperature reported in Fig. 4.1. This is expected since they are closer to the heating elements in the hotplate. The thermocouple at the leading edge of the hotplate (ET4) has the highest temperature in Figs.

4.2 and 4.3. This can be attributed to flow stagnation at the leading edge of the hotplate. This reduces the ability of the wind to cool the plate by convection and hence the high temperature recorded. Note that the plate is a like bluff body at the underside of the test vehicle. On the other hand, the thermocouple on the trailing edge of the hotplate (ET2) has the lowest temperature (Figs. 4.2-4.3). This is probably because separated flow reattached to the plate at that point thus cooling the plate more through an increase in convective heat transfer coefficient. At zero yaw the temperatures are the highest and decrease with yaw angles greater than zero. This is also attributed to flow separation at the leading edge at zero yaw resulting in less cooling. However, as the angle increases the hotplate is more exposed to direct airflow from the wind tunnel which results in more cooling of the hotplate (Figs. 4.2-4.3). As expected the data also show variation with the ambient temperature as the 50°C condition recorded higher values than 10°C ambient temperature condition.

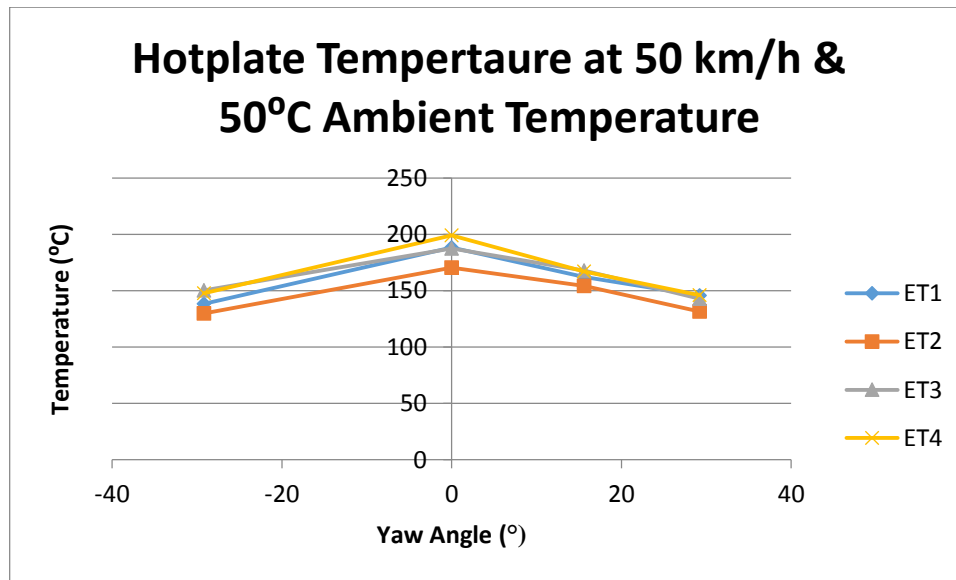


Figure 4.2: Hotplate temperature at different yaw angles.

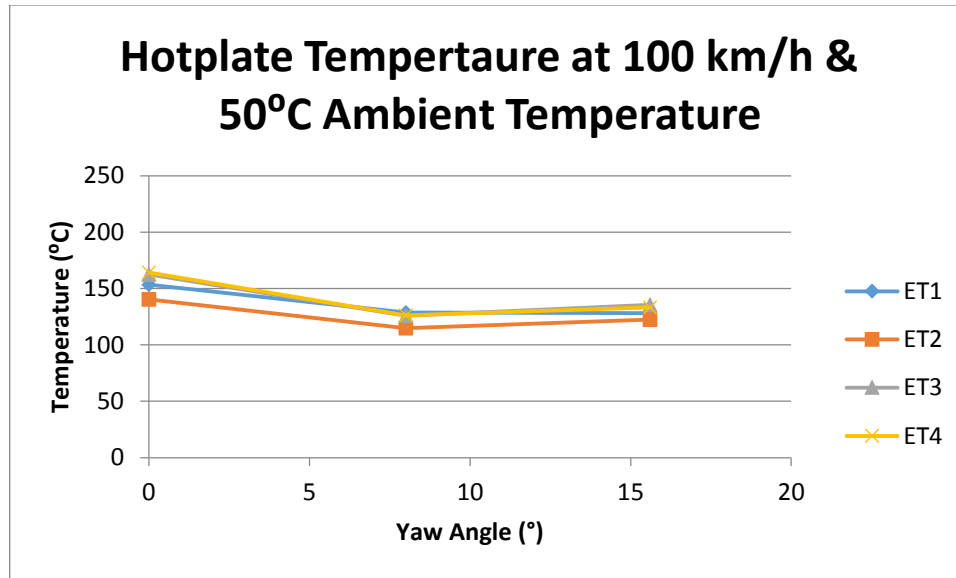


Figure 4.3: Hotplate temperature at different yaw angles.

4.1.2: Temperature Distributions of Vehicle Underbody

Temperature data are reported in Figs. 4.4-4.6 to provide information about the underbody temperature distribution for the three cases indicated: 0° yaw, 50 km/h and 10°C (Fig. 4.4), 15.6° yaw, 50 km/h and 10°C (Fig. 4.5) and 29.2° yaw, 50 km/h and 10°C (Fig. 4.6). In general only the temperatures of the thermocouples in the vicinity of the hotplate are most affected by the hotplate. In fact, the temperature recorded by majority of the thermocouples is not significantly different from the ambient temperature. This is expected because of the small size of the hotplate and direction of the airflow. At 0° yaw (Fig. 4.4), the temperature is relatively evenly distributed at both the driver and passenger sides of the hotplate. It clearly shows that the heat was convected from the hotplate to the thermocouples at the downstream end of it as expected. The figure also shows that the thermocouples behind the beam axle of the rear suspension remained the same as the ambient temperature values. However, they were expected to record higher temperatures since they appear to be in the

airflow direction and heat was expected to be convected to them. As will be explained later, it was observed that the rear axle of the test vehicle was unusually low and therefore blocked convected heat from reaching the thermocouples behind it. In fact, smoke visualization, the results of which are not reported here, also confirmed this phenomenon.

In Figs. 4.5-4.6, the yaw angles were increased and exposed the driver side of the hotplate to the nozzle airflow, which then convected the heat from that side of the hotplate to the downstream end of the passenger side. It was expected that the heat would be convected across the hotplate diagonally to the driver side and this occurred. When the direction of the yaw angle changed to negative 29.6° the trends described above were reversed as expected although not identical since the underbody is not symmetric as will be explained later.

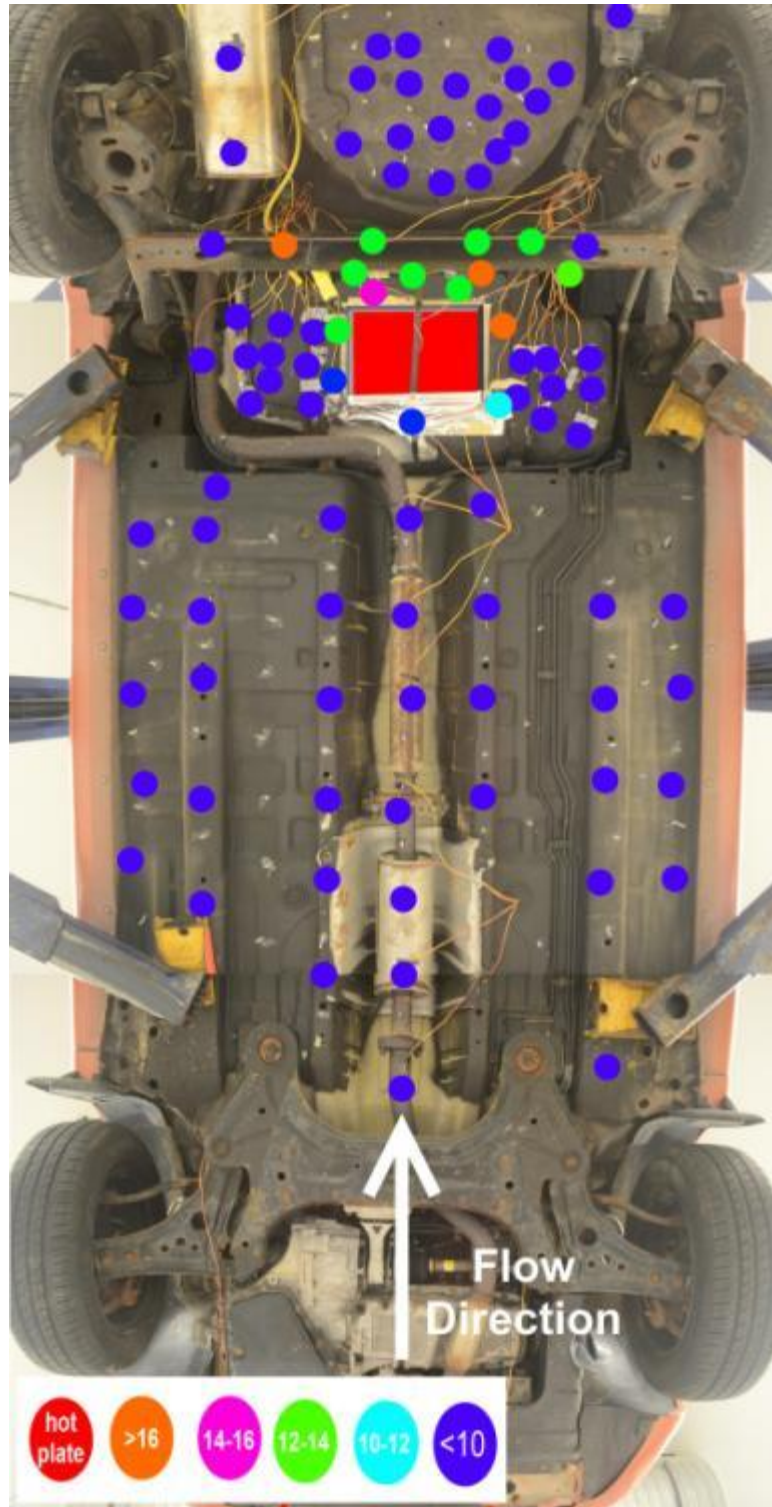


Figure 4.4: Underbody temperatures for 0° yaw, 50 km/h and 10°C.

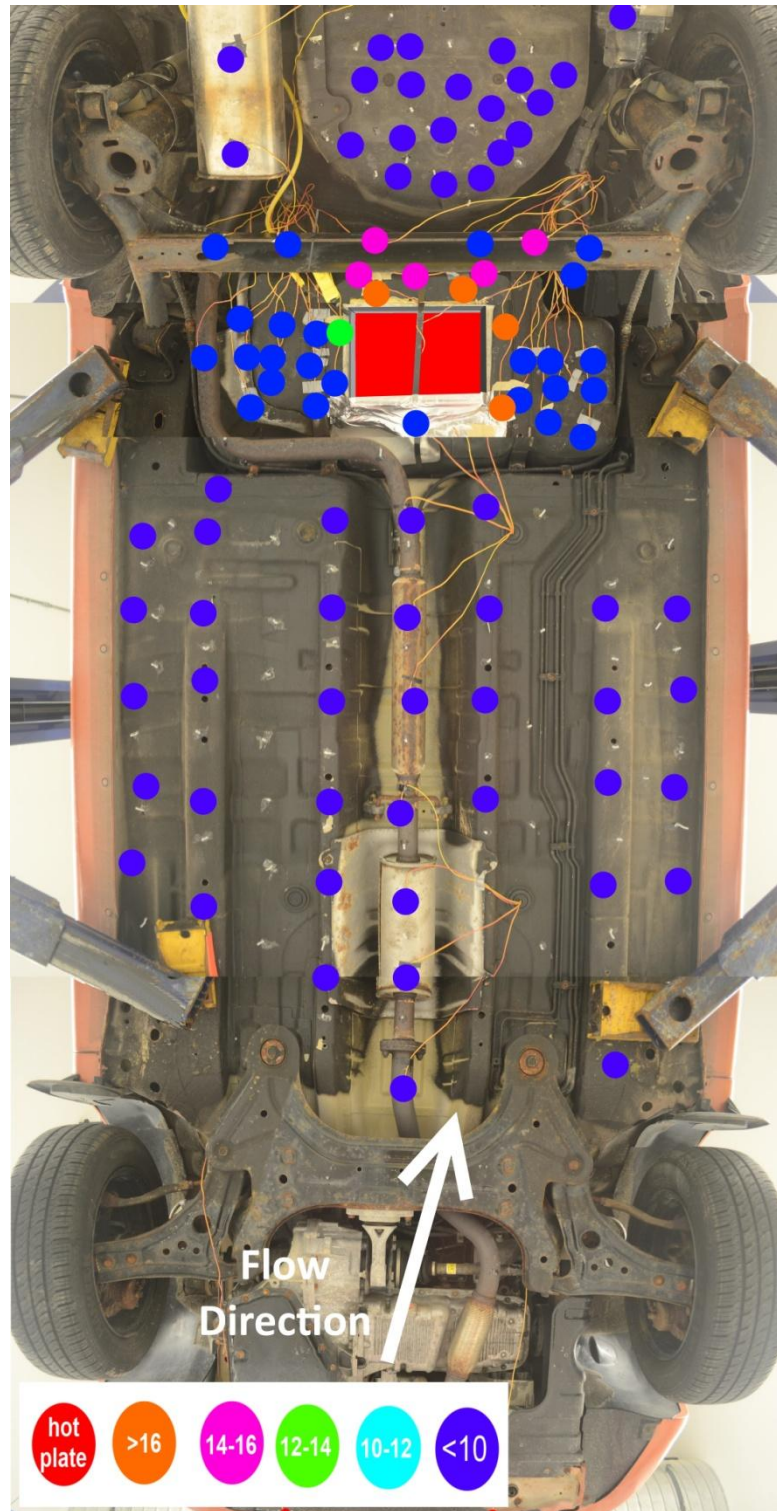


Figure 4.5: Underbody temperatures for 15.6° yaw, 50 km/h and 10°C.

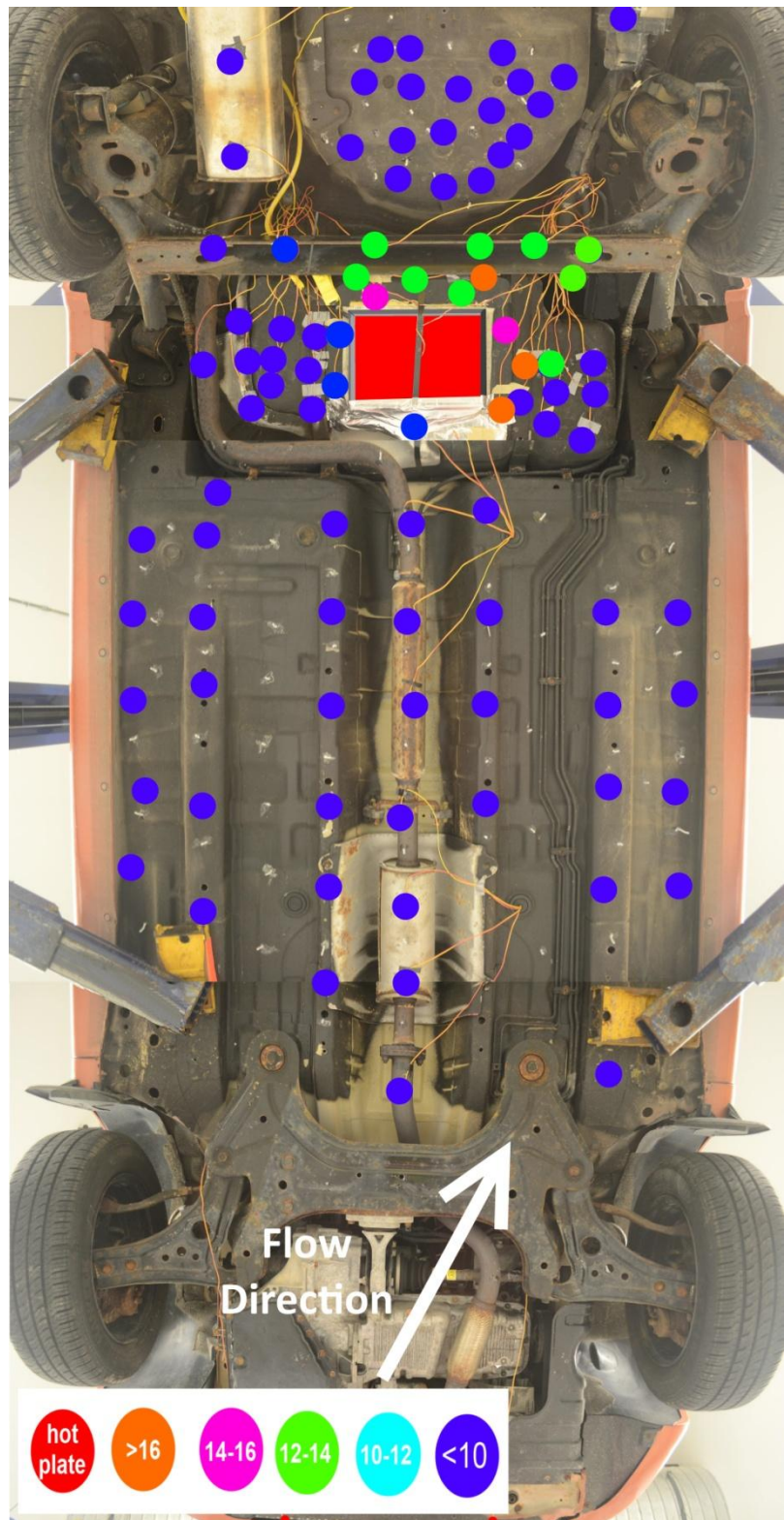


Figure 4.6: Underbody temperatures for 29.2° yaw, 50 km/h and 10°C.

Furthermore, the trends remained similar even when the road speed and ambient temperature were increased to 100 km/h and 50 °C, respectively.

In addition to the qualitative trends discussed above, the actual temperature values were plotted with yaw angles to provide quantitative information on the effect of cross-wind on the temperature distribution as shown in Figs. 4.8-4.11. As mentioned earlier, only a few thermocouples close to the hotplate recorded significant temperatures above the ambient values. Thus the focus of this section is the area in the vicinity of the hotplate. For convenience the thermocouples are numbered T1 to T11 as indicated in Fig. 4.7.

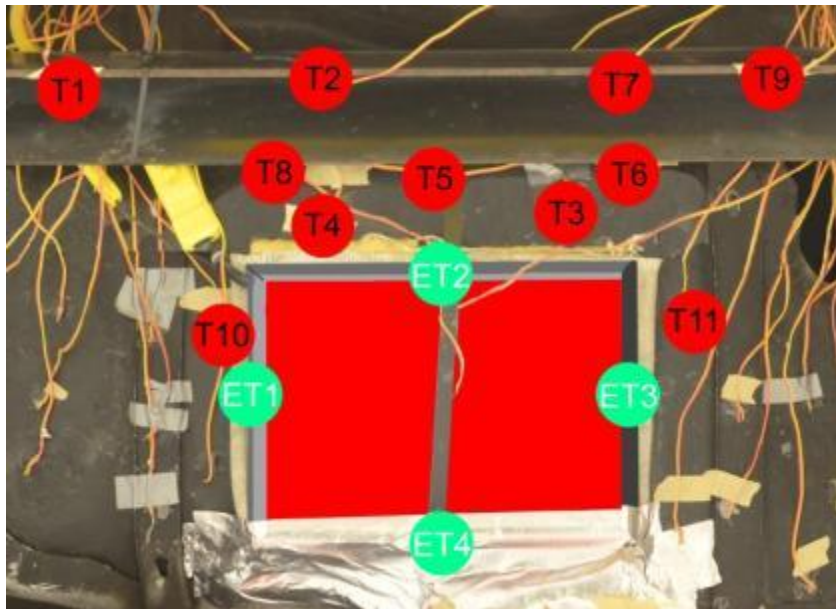


Figure 4.7: A picture of the mounted the hotplate and labels of the most sensitive thermocouples recorded in the experiments.

Figure 4.8 shows the temperatures measured by the selected thermocouples at 50 km/h road speed and 10⁰C ambient temperature. Recall the yaw direction is shown in Fig. 3.3 in which the incoming air increasingly points towards the driver side with increasing yaw angle. As the yaw angles increased from 0⁰ to 15.6⁰ the temperature of the passenger side (T3, T6, T7, T9 and T11) predominantly increased whereas those on the driver side (T1, T2, T4, T8

and T10) generally decreased. This is consistent with the qualitative observation made in the previous section. As explained earlier, when the yaw angle increased the driver side of the hotplate was exposed more directly to the nozzle airflow, which convects the heat from the hotplate to the thermocouples at the passenger side, thus the higher temperature readings. From Fig. 4.7, one might suspect the air to blow diagonally across the hotplate to the thermocouples at the passenger side and this exactly occurred.

However, increasing the yaw angle further to 29.2° resulted in a decrease in all the temperature values. The large yaw angle obstructed the hotplate from the full impact of the airflow unlike the case for the 15.6° yaw. This resulted in less heat convected and hence the decrease in temperature. Switching the yaw angle to negative 29.2° gave trend roughly opposite those described for the positive 29.2° . Note that the profiles are not symmetric due to the asymmetrical nature of the underbody. This change in physical arrangement could locally change the flow, leading to the differences observed.

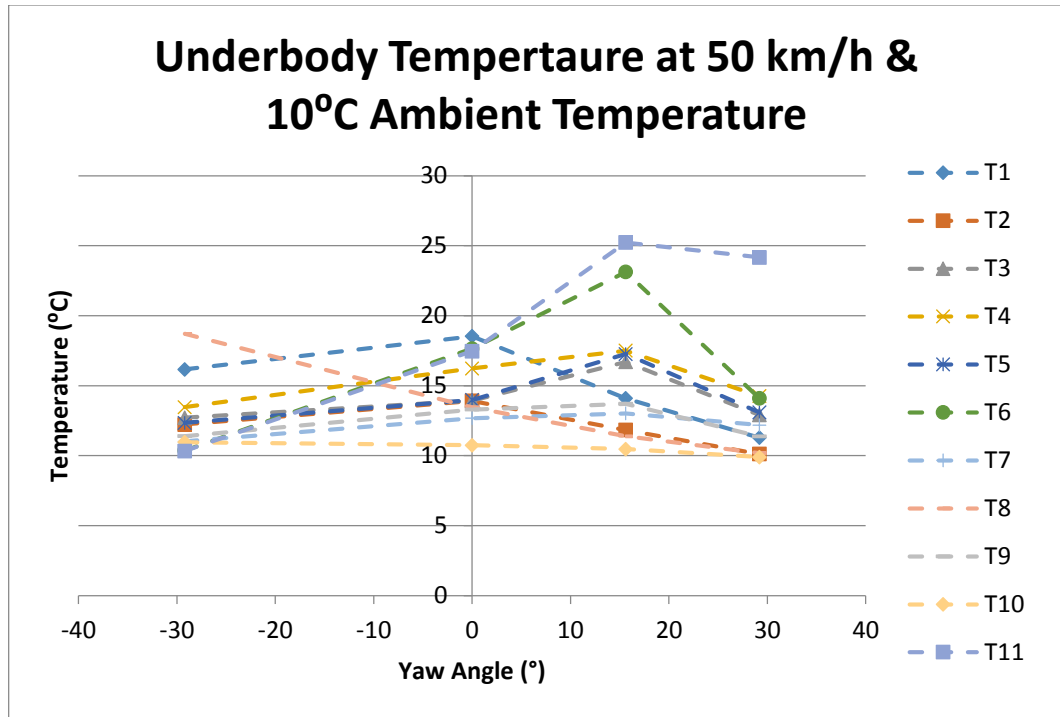


Figure 4.8: Underbody temperature distribution for selected thermocouples at different yaw angles.

Figure 4.9 shows the temperature profiles for 100 km/h and 10°C temperature. Note that only three angles were tested in this case. Overall, the most noticeable trend is the much tighter spread among the temperatures. However, the trends are similar to those described earlier for the 50 km/h speed. Thermocouples T6 and T11 again recorded the highest temperatures. This suggests that in comparison with the 50 km/h test the yaw angle has a greater impact on the temperature distribution than road speed. The slight dip for 8° yaw test is not understood but it can be speculated that the orientation of the hotplate restricted the airflow from convecting heat to the thermocouples.

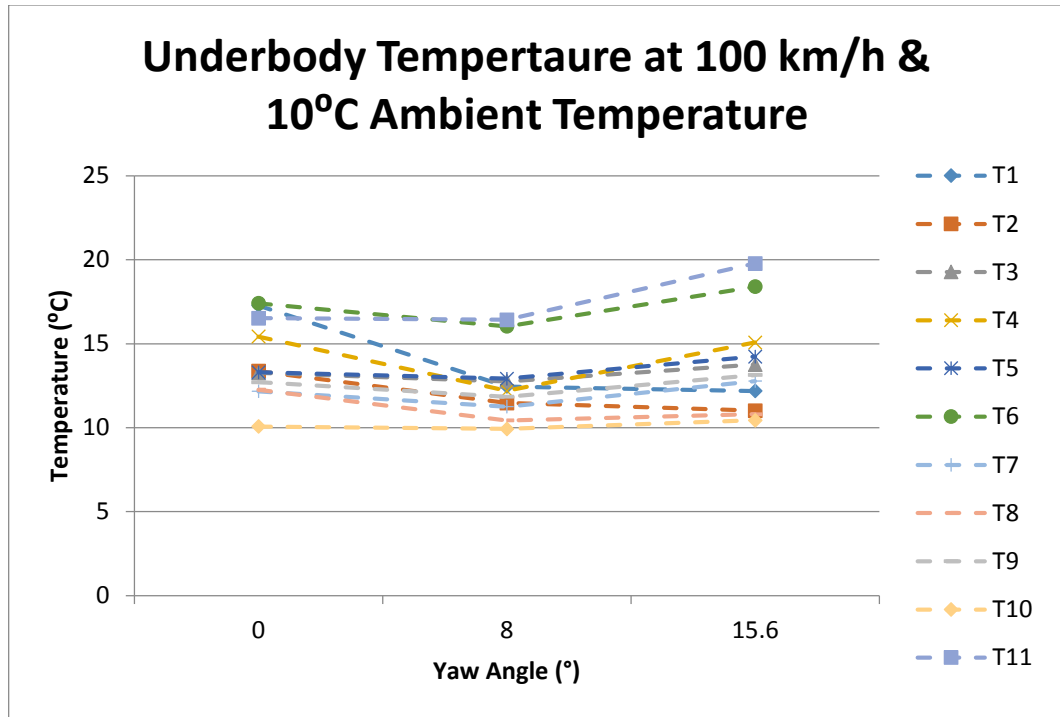


Figure 4.9: Underbody temperature distribution for selected thermocouples at different yaw angles.

The temperature profiles for 50 km/h road speed and 50°C ambient temperature are shown in Fig. 4.10. By comparing this figure with Fig. 4.8 it is evident that the ambient temperature has quite an effect on the temperature distribution. The temperature values are highest for the 0° yaw unlike in Fig. 4.8 where the highest temperature was at 15.6° yaw. In addition, a number of thermocouples including T3, T6, T9 and T11 at the passenger side now show trends different from what they were in Fig. 4.8.

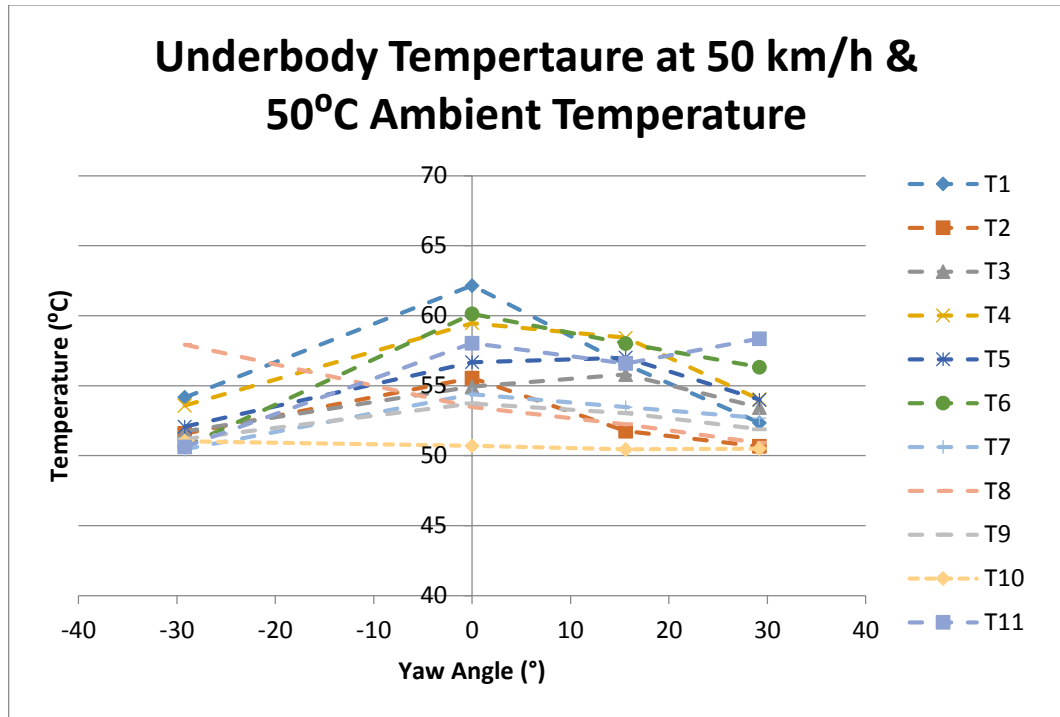


Figure 4.10: Underbody temperature distribution for selected thermocouples at different yaw angles.

Finally, Fig. 4.11 details the temperature results from the 100 km/h and 50°C case. The temperature profiles have similar trends as those described in Fig. 4.9 except that the values did not increase from 8° to 15.6° but rather remained nearly constant.

To examine the effect of rotating and non-rotating wheels, the same yaw angle was maintained and only the rollers (simulating the road in other tests by rotating the tires) were turned off. These comparisons were made at 100 km/h at 10°C and 50°C ambient temperature at 0° and 15.6° yaw. At both yaw angles and 10°C, the effect of stopping the wheels was negligible and no appreciable variance in temperature was recorded. However, at 50°C there was a noticeable effect with the thermocouples at the passenger side recording a higher temperature reading during the non-rotating wheel case than the rotating wheel

case. The results suggest that rotating wheels can help to cool the hot-plate further as the wheel motions acts to drive the air from out of the wheel well.

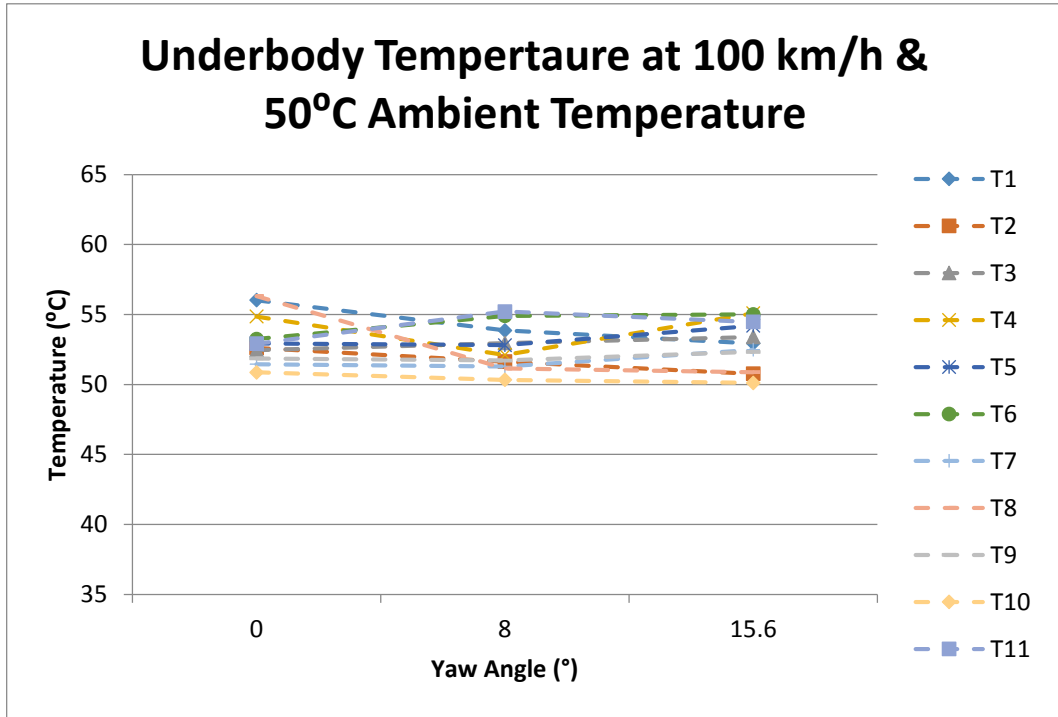


Figure 4.11: Underbody temperature distribution for selected thermocouples at different yaw angles.

4.1.3: Flow Visualization with Tufts

The flow visualization was conducted using tufts to provide whole-field flow patterns to qualitatively represent the local flow direction under the vehicle. The figures shown below are screen captures of videos obtained by the GoPro cameras described in Section 3.2. Three cameras were employed and were positioned to capture images across the entire width of the test vehicle underside. All the cameras were at approximately 1.8 m downstream of the front axle of the test vehicle. The approximate field of view of each camera was about 40 cm × 40 cm. In this report only the images that captured the flow

angle probes at the driver side and passenger side are presented for convenience. Note that the images have the fish-eye effect and are therefore a bit distorted at the edges so that the directions of the tufts are not as they appear at the edges. As a result the tufts with extreme distortions due to the fish-eye effect (at the edges of the image) are not taken into account in the discussion. In addition, arrows are used to represent the average direction of the tufts (i.e., flow direction). The directions of these arrows are rough estimates of the average flow direction of the tuft determined after carefully watching the video for approximately 10 minutes.

As shown in the figures below the tufts follow consistent patterns but there are significant local effects caused by the complexity and unevenness of the vehicle's underbody especially the exhaust piping channels. For the 0° yaw case shown in Fig. 4.12, the tufts at the driver side (Fig. 4.12a) point in a direction consistent with the nozzle airflow but the tufts close to the exhaust piping channel are not. This can be attributed to local effects resulting from circulating flows caused by the exhaust piping channel. For the same test condition, the image obtained by the camera at the passenger side is shown in Fig. 4.12b. In this image the directions of the tufts are not as consistent as in Fig. 4.12a due to local underbody geometry effects mainly from the exhaust piping channel.

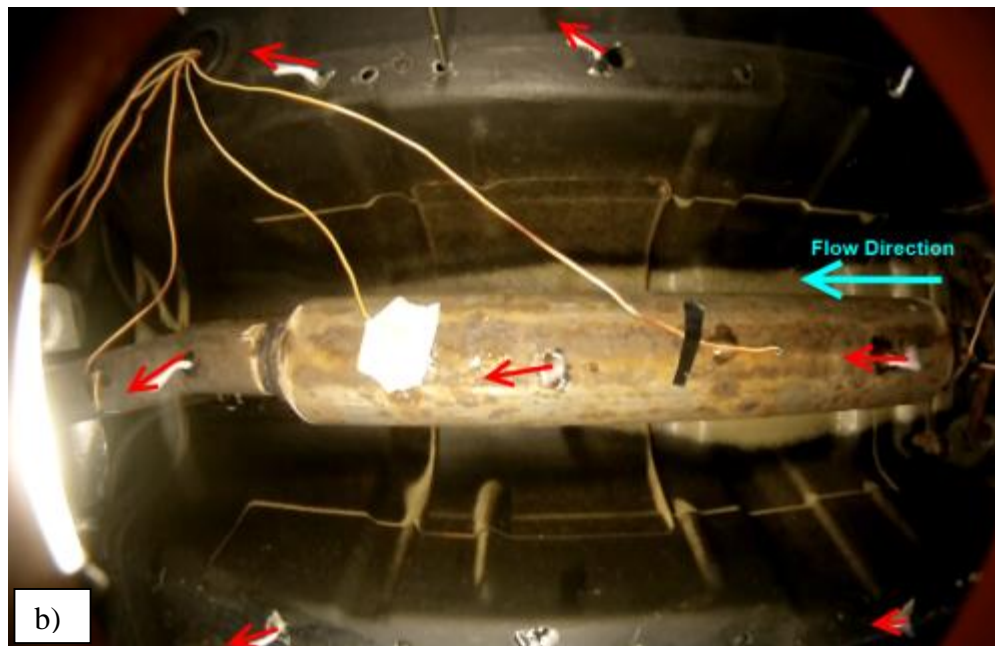
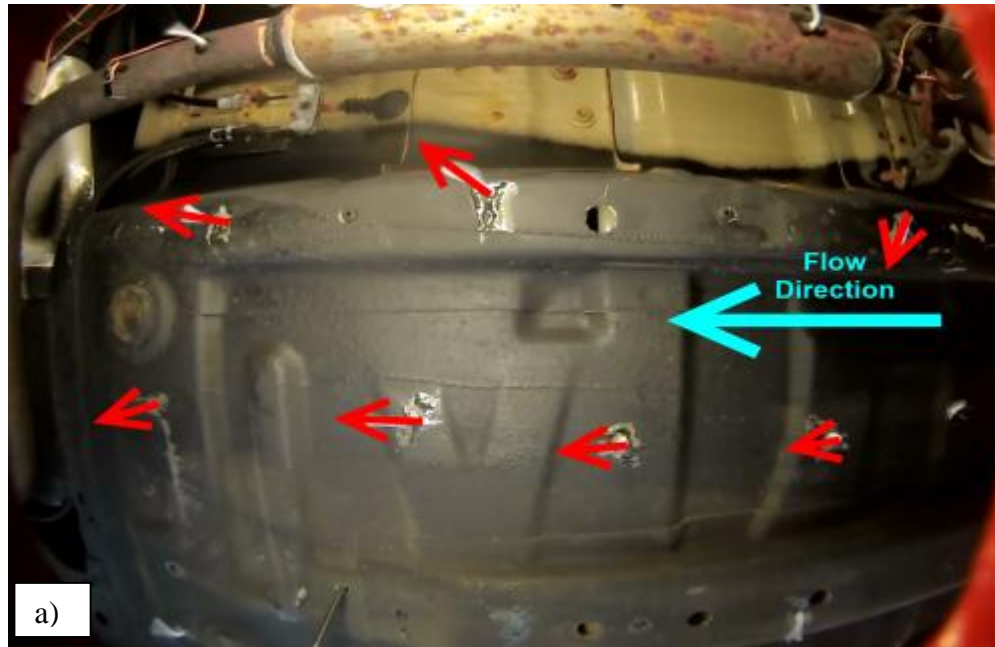


Figure 4.12: A screen shot from a flow visualization video for 0° yaw (Test 1 in Table 1) at the driver side (a) and passenger side (b). Average directions of the tufts are represented by arrows.

The results of Test 2 (15.6° yaw, 50 km/h and 10°C) are shown in Fig. 4.13. While the direction of the tufts in Fig. 4.13a appears largely consistent with the flow direction of the nozzle airflow, this is not entirely the case due to the local effects explained above. Fig.

4.14 and 4.15 have similar ambient conditions but with opposite yaw angles of positive 29.2° and negative 29.2° , respectively. Interestingly for both of these large yaw angles the flow patterns indicated by the direction of the tufts are consistent with the nozzle airflow. The reason for this sudden consistency with no apparent local effects from asymmetric nature of the underbody is not yet understood. However, it is obvious that high wind speed dampened the local effects.

In Fig. 4.16a the flow patterns indicated by the tufts are similar to the 50km/h case and are fairly well organized, with the local flow in the direction of the wind except minor local effects. On the other hand, Fig. 4.16b shows that there is a high degree of turbulence and flow circulations as indicated by the tufts pointing in various directions. Again these local effects can be attributed to the relatively complex geometry affecting the flow.

Finally, the flow patterns in Fig. 4.17 are also similar to those in Fig. 4.13 which has the same yaw and temperature but twice the road speed. In fact, the results also confirm the previous observation that at 15.6° yaw the more complex local underbody geometry has higher velocities and a more realistic yaw angle than the smoother driver side. As mentioned earlier, the reason why this yaw angles overcome of effects of the local geometry is not yet fully understood.

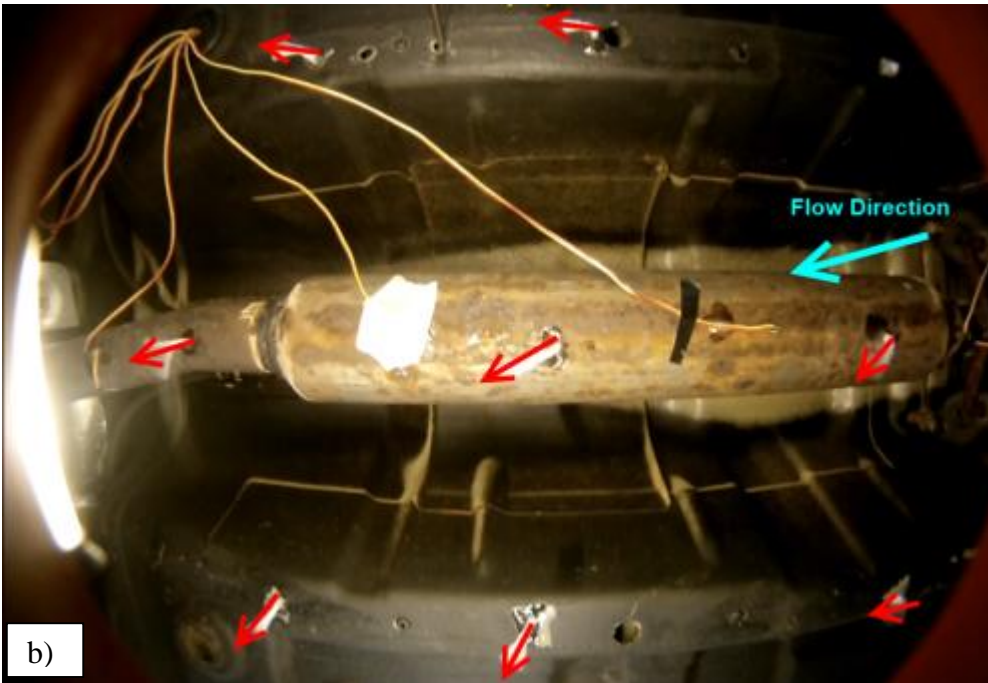
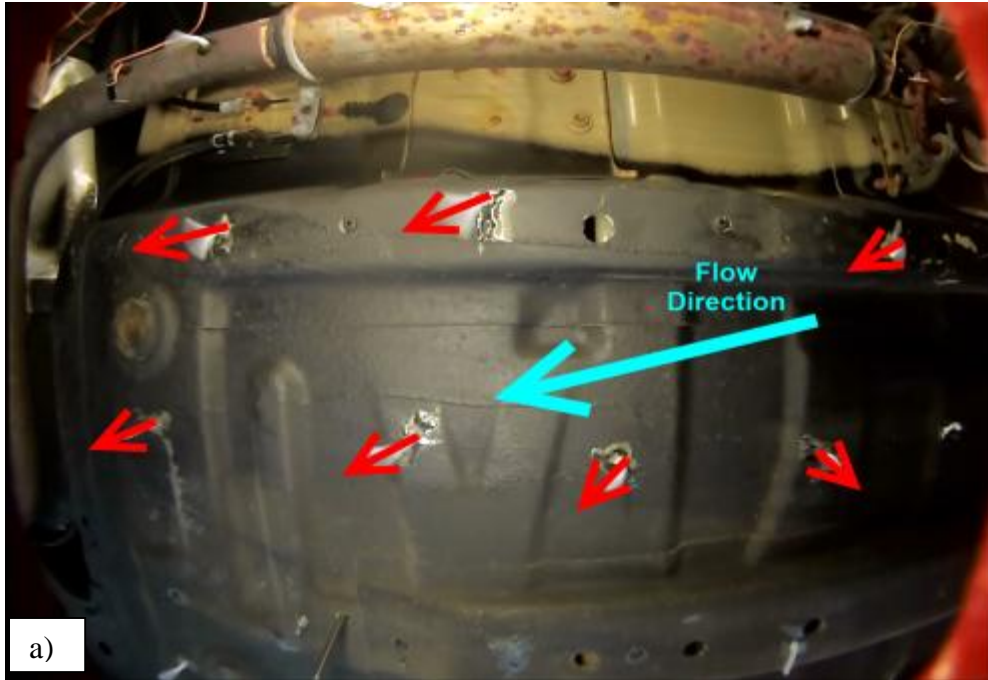


Figure 4.13: A screen shot from a flow visualization video for 15.6° yaw (Test 2 in Table 1) at the driver side (a) and passenger side (b). Average directions of the tufts are represented by arrows.

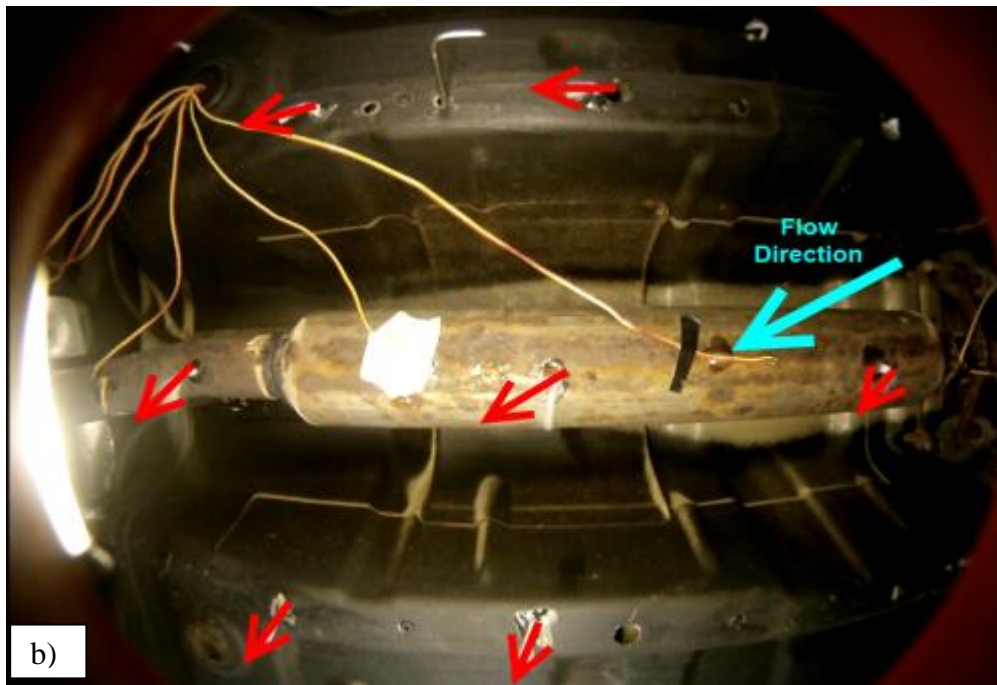
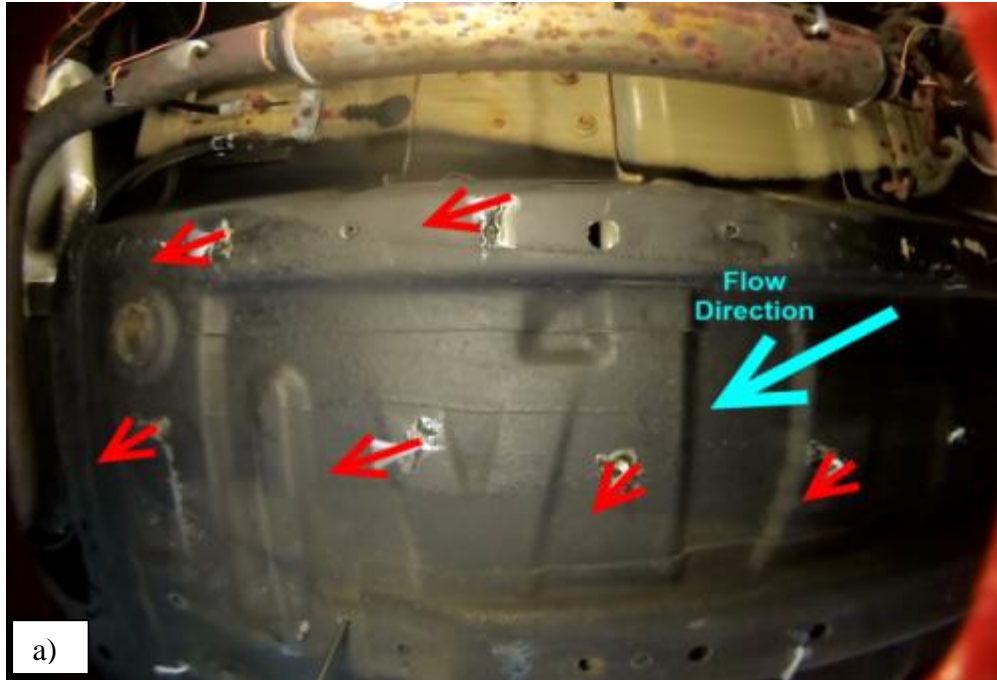


Figure 4.14: A screen shot from a flow visualization video for 29.2° yaw (Test 3 in Table 1) at the driver side (a) and passenger side (b). Average directions of the tufts are represented by arrows.

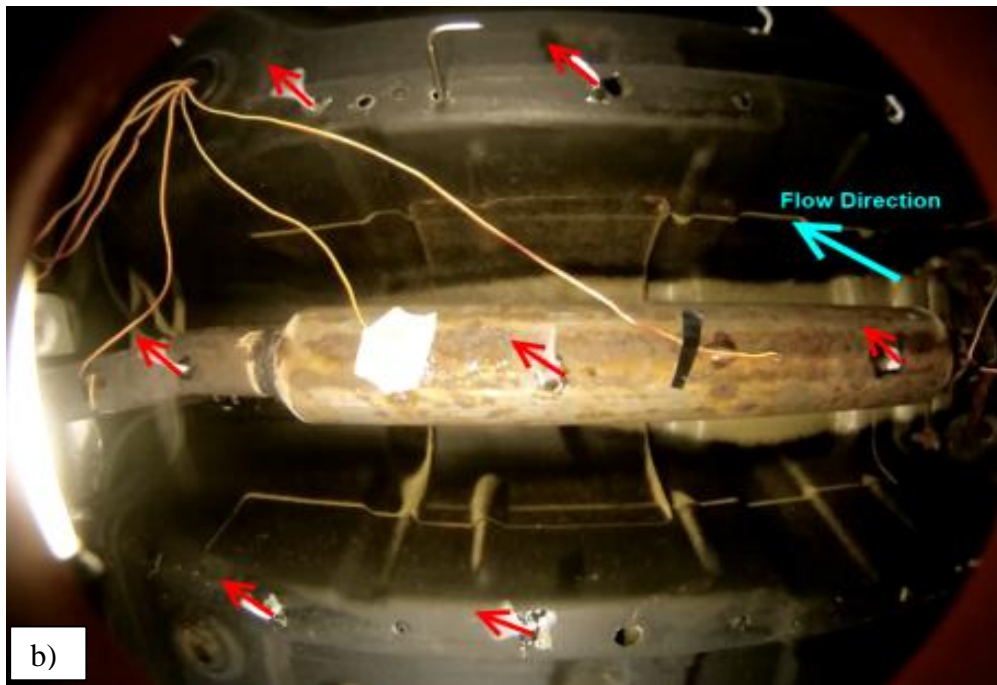
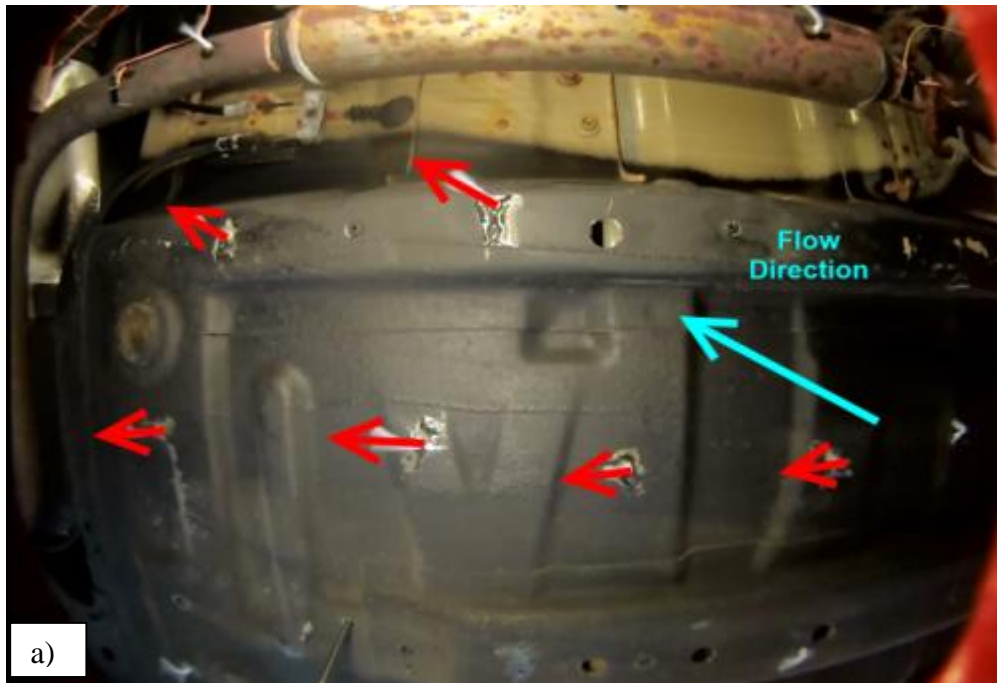


Figure 4.15: A screen shot from a flow visualization video for -29.2° yaw (Test 4 in Table 1) at the driver side (a) and passenger side (b). Average directions of the tufts are represented by arrows.

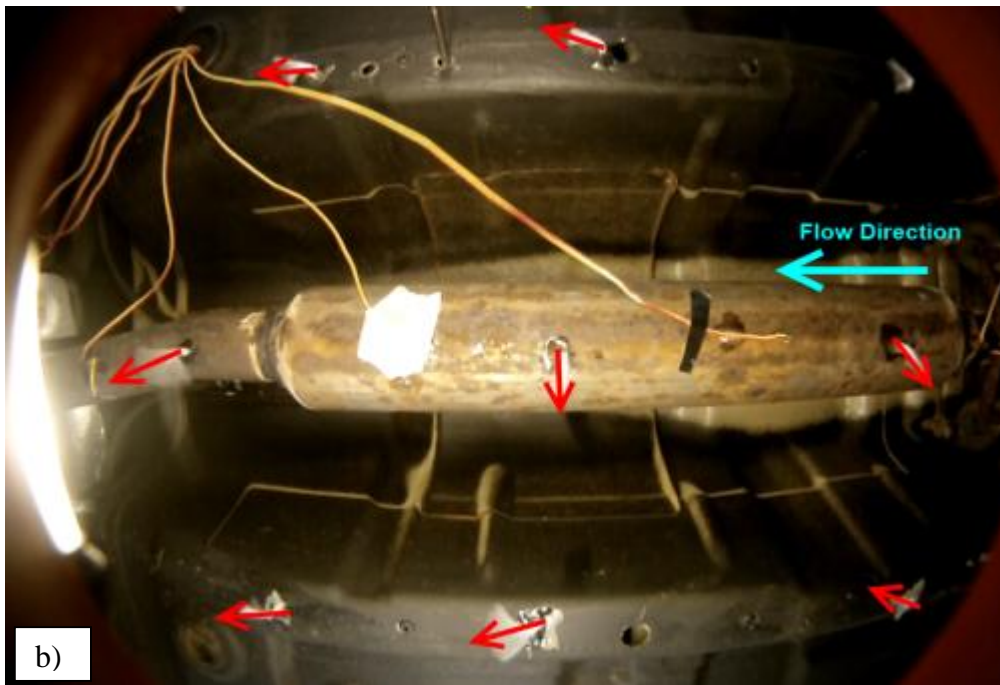
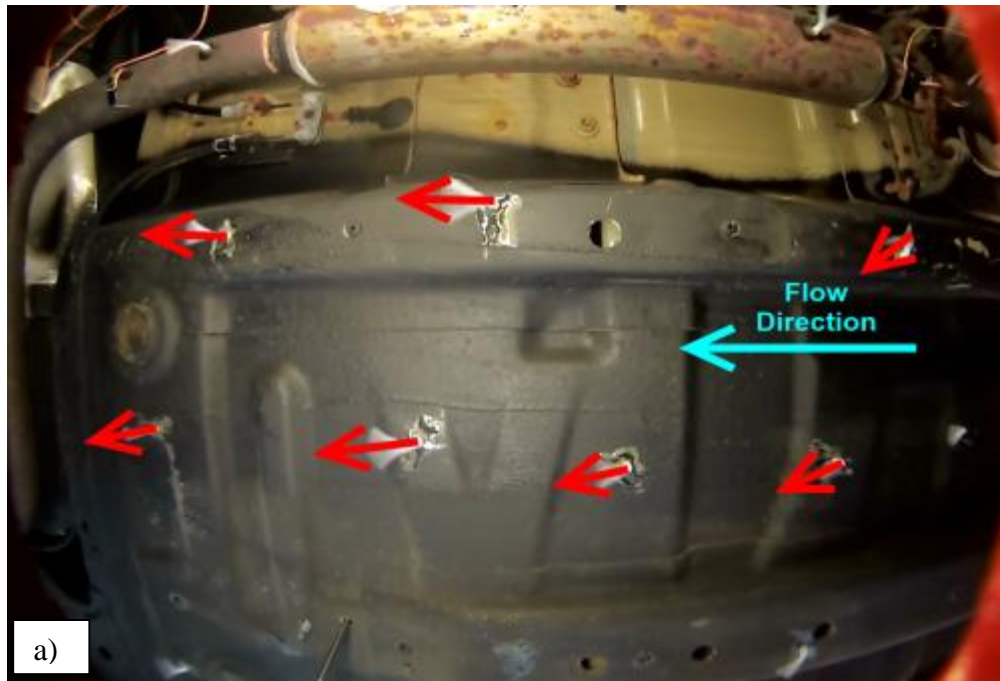


Figure 4.16: A screen shot from a flow visualization video for 0° yaw (Test 6 in Table 1) at the driver side (a) and passenger side (b). Average directions of the tufts are represented by arrows.

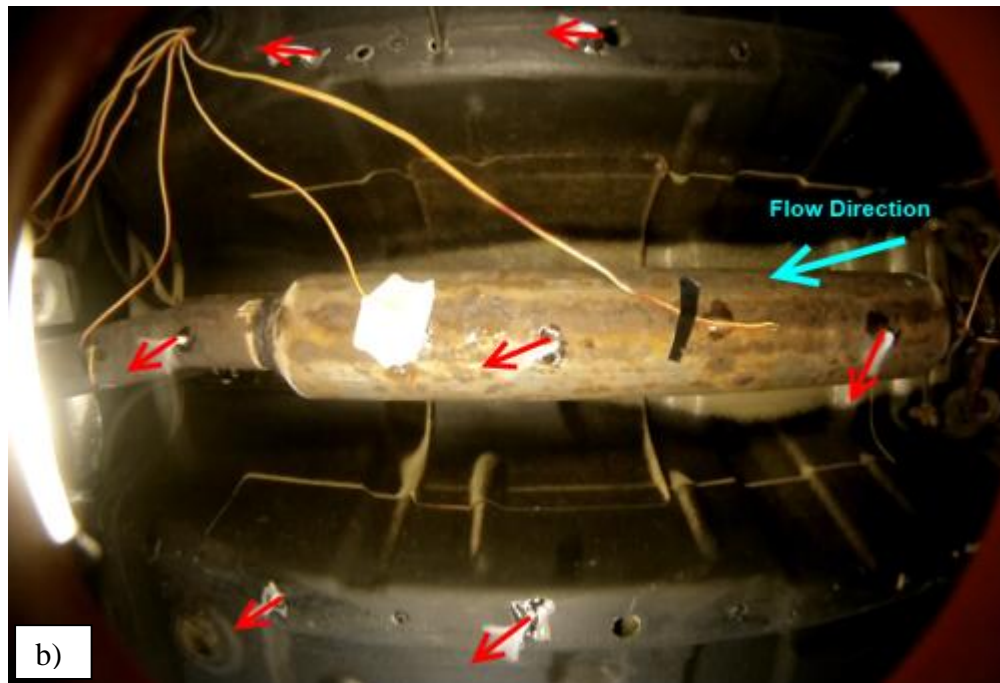
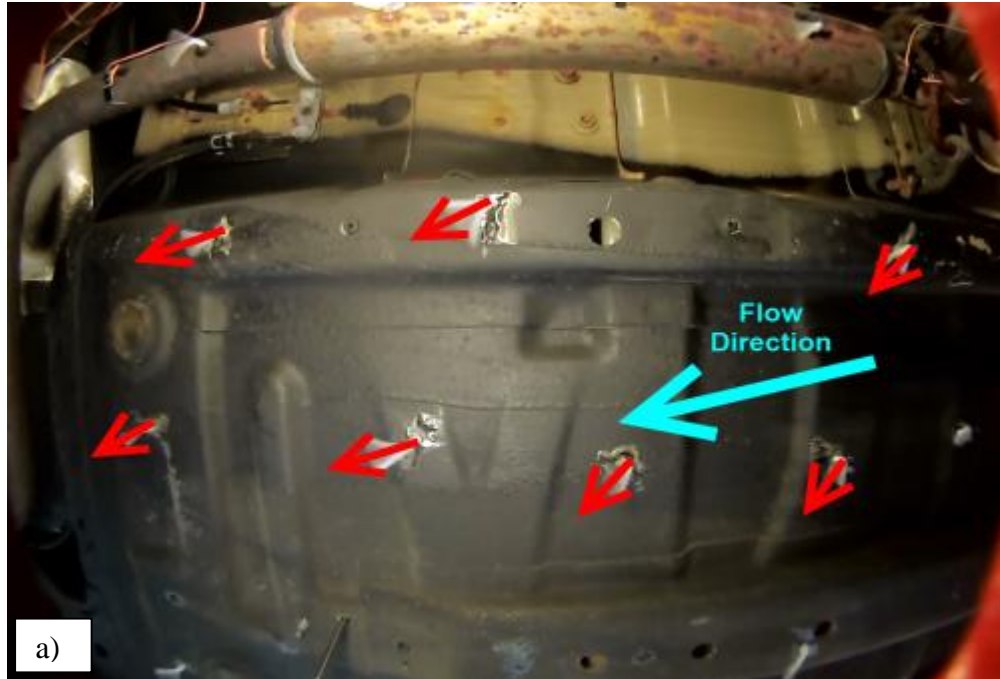


Figure 4.17: A screen shot from a flow visualization video for 15.6° yaw (Test 8 in Table 1) at the driver side (a) and passenger side (b). Average directions of the tufts are represented by arrows.

4.2: Numerical Data

4.2.1: Numerical Validation

Two test conditions were validated with experimental data: the 0° yaw and 50 km/h wind speed, and the 29.2° yaw and 50 km/h case (Tests 1 and 3 respectively in Table 1). These tests were chosen because they represent the extreme cases. Fifteen experimental points around the hot plate were compared with the numerical analysis. Data near the hotplate was used because they are assumed to represent the worst case scenario. This is because near the hotplate there are large temperature variations in comparison to the upstream of the hotplate. It was decided to validate the numerical analysis with this worst case scenario. Seven points of these were on the driver's side of the vehicle and 8 points on the passenger side. The locations of the thermocouples whose temperatures were used for the validation are shown in Fig. 4.18 below. Note that the numerical data were extracted at similar locations.

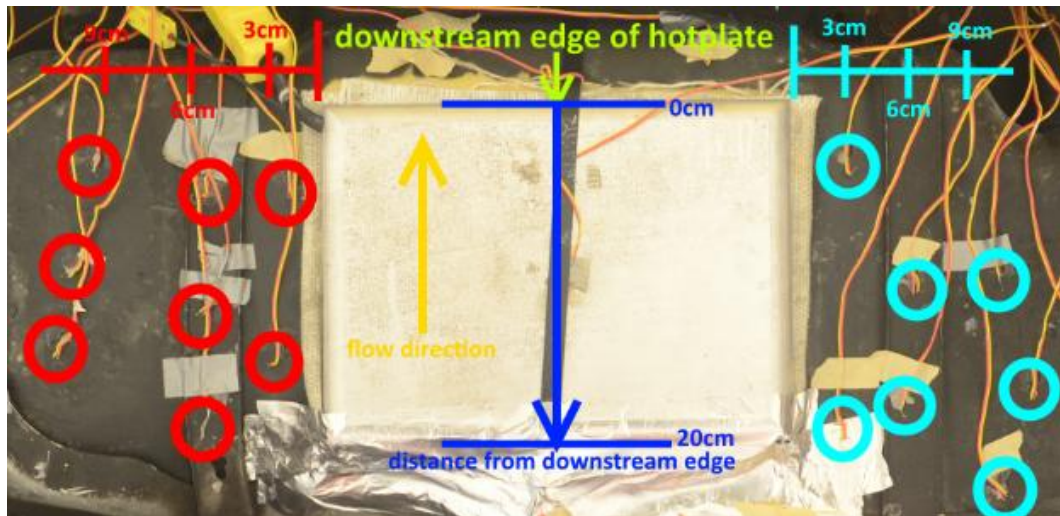


Figure 4.18: Thermocouples used for numerical validation. Thermocouples encircled in red are on the passenger side, thermocouples encircled in blue are on the driver side.

Figures 4.19-4.21 illustrate the temperature data observed from the experiments versus the numerical analysis for the 0° yaw case on the driver side. Each graph is a single column of thermocouples as shown in Fig. 4.18: each column of thermocouples is 3 cm, 6 cm and 9 cm away from the hotplate. There are at least 2 thermocouples per column as indicated by the data points on the graph. Numerically, more data points can be captured which is why there are 10 data points of numerical data per graph. This explains why the numerical data plotted are more than the experimental data as shown in Fig. 4.19. The distance from the downstream (i.e.: towards the rear of the car) edge of the hotplate is approximated for the experimental data points.

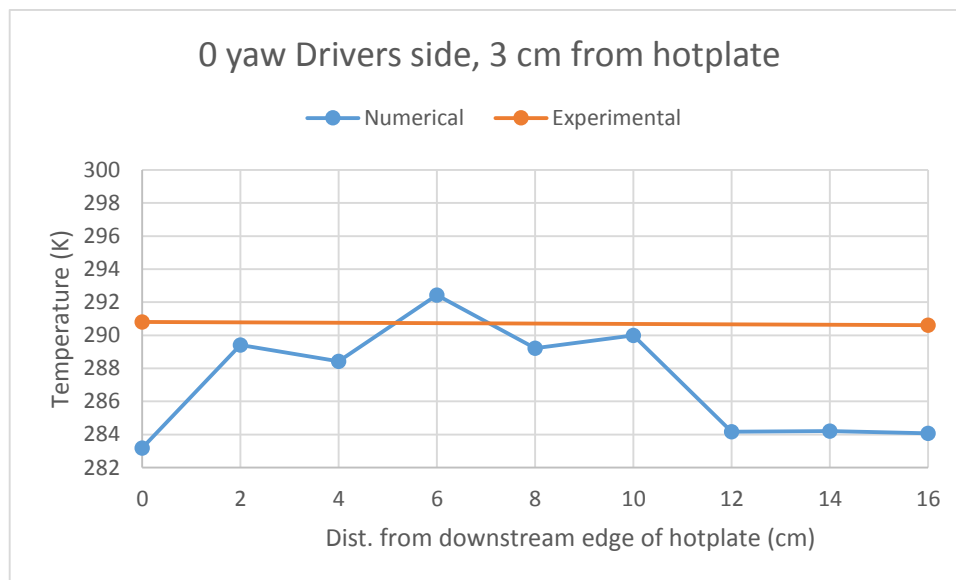


Figure 4.19: Comparison of numerical and experimental temperature data 3 cm away from the hotplate at 0° yaw on the driver side.

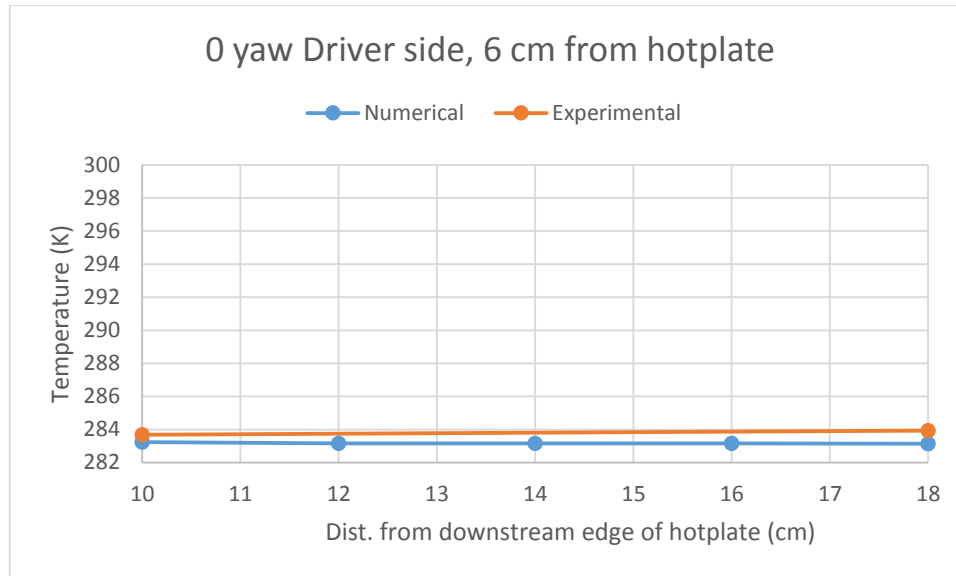


Figure 4.20: Comparison of numerical and experimental temperature data 6 cm away from the hotplate at 0° yaw on the driver side.

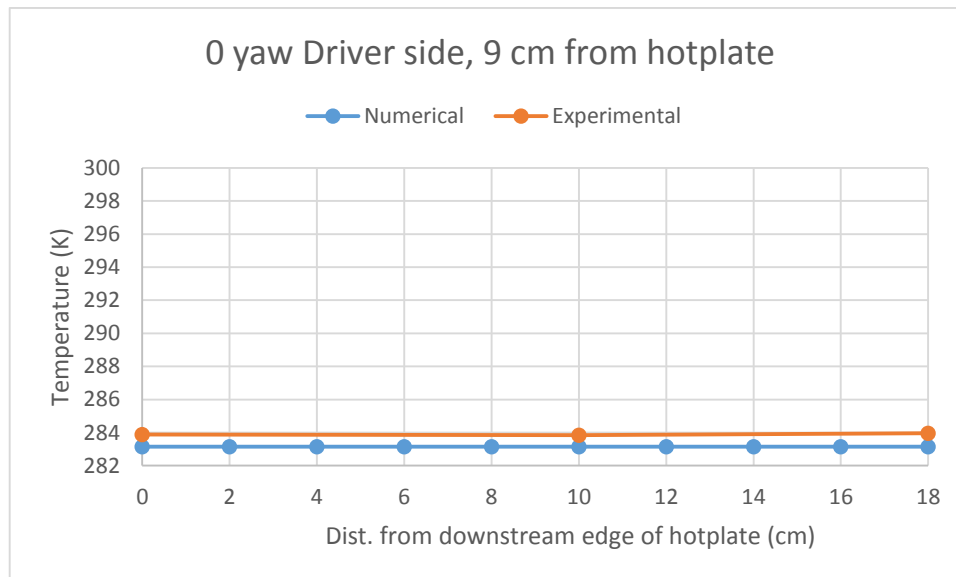


Figure 4.21: Comparison of numerical and experimental temperature data 9 cm away from the hotplate at 0° yaw on the driver side.

This percent differential was calculated through the following formula:

$$\frac{T_{numerical} - T_{experimental}}{T_{experimental}} \times 100\% = \text{percent difference} \quad (9)$$

On the driver side at 0° yaw, there is a little difference in temperature further away from the hot plate as shown by Fig. 4.20 and 4.21 where the temperature difference is less than

a degree. Closer to the hotplate, where the temperature is higher, there is a greater variance between the experimental and numerical data as expected. The difference is 8 degrees which represents approximately 3% difference which is within the 10% range of error considered acceptable for engineering applications (Karniadakis and Sherwin, 2005). This could be due to the complex flow around the hotplate and underbody in addition to the large temperature gradients which are difficult to model.

For the 29.2° yaw test, similar plots were developed as shown in Figs. 4.22-4.24 below.

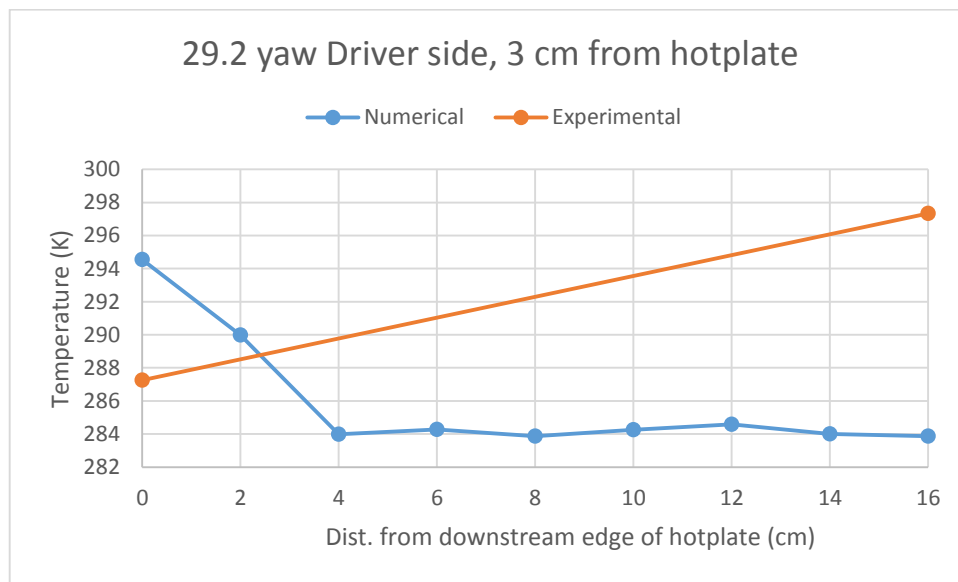


Figure 4.22: Comparison of numerical and experimental temperature data 3 cm away from the hotplate at 29.2° yaw on the driver side.

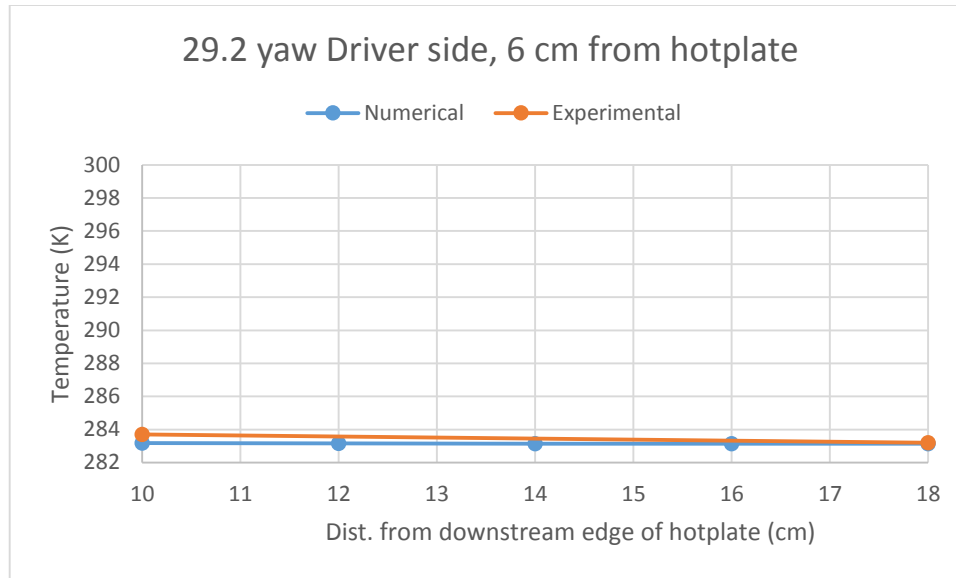


Figure 4.23: Comparison of numerical and experimental temperature data 6 cm away from the hotplate at 29.2° yaw on the driver side.

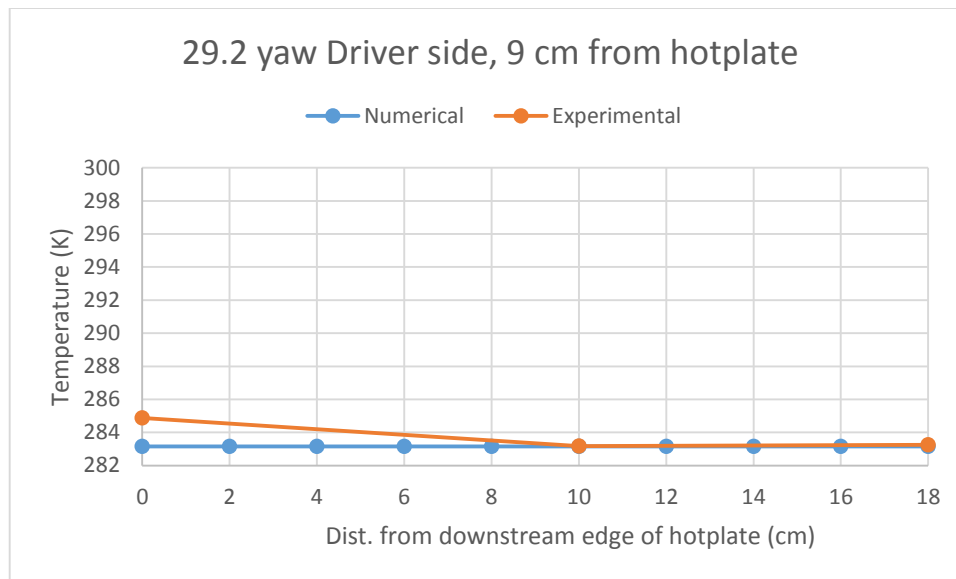


Figure 4.24: Comparison of numerical and experimental temperature data 9 cm away from the hotplate at 29.2° yaw on the driver side.

At 29.2 degrees yaw, it appears that the numerical data underestimates the temperature consistently on the driver side aside from the first point in Fig. 4.22. The largest overestimation between points is in Fig. 4.22, where the difference in temperature is approximately 13 degrees (or 5%). This is seen to smaller degrees closer to the hotplate.

Perhaps the small wake directly behind the driver side of the hotplate as the vehicle is yawed is not accurately modelled to capture the aero-thermal phenomena due the complex geometries involved around the gas tank and hotplate.

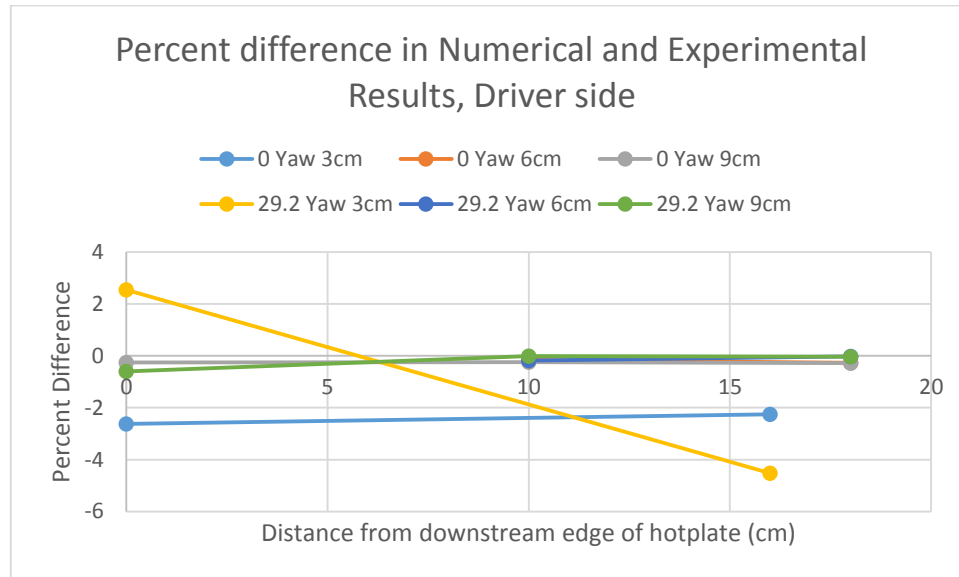


Figure 4.25: Percent difference in the numerical and experimental results for the driver side.

The maximum percent difference in Fig. 4.25, approximately 5%, is still within the accepted range of error for numerical data (Karniadakis and Sherwin, 2005). Upstream along the hotplate towards the front of the vehicle, the errors were observed to decrease.

A similar analysis was performed on the passenger side: the numerical simulations tend to underestimate temperature at 0 yaw, and overestimate the temperatures at 29.2 yaw. The graphs comparing the experimental and numerical data are presented in Appendix A. The percent differences are presented below in Fig. 4.26; the passenger side has even better accuracy than the driver side, with the maximum percent difference being approximately 2.5%.

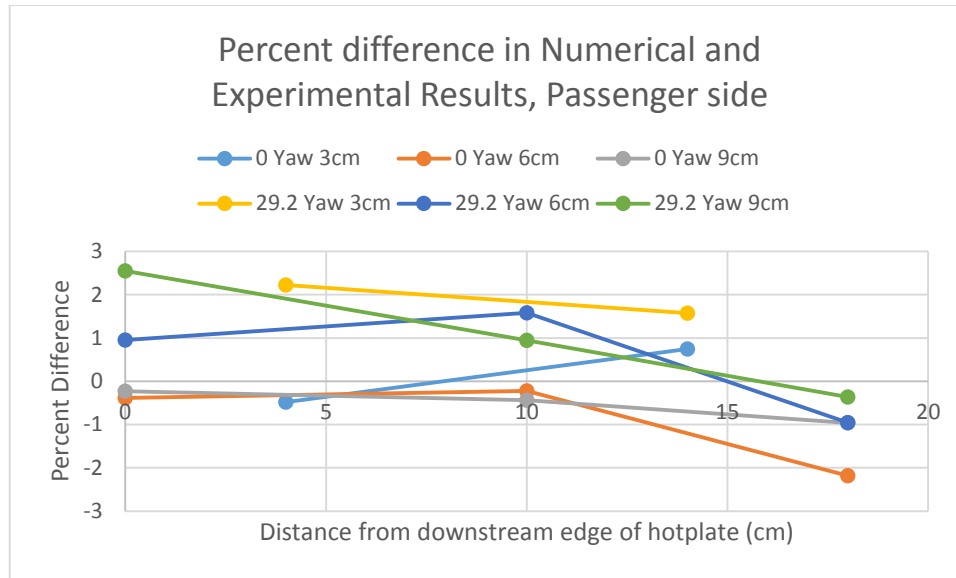


Figure 4.26: Percent difference in the numerical and experimental results for the passenger side.

4.2.2 Grid Independence

The purpose of grid independence is to ensure that the solutions are not dependent on how the domain is discretized. If the domain is too coarse (i.e., filled with larger elements), it may not capture the details correctly, especially wake effects that vary in size. In addition, if the discretization is too large, the values could be inaccurate.

In this grid independence test three meshes of different sizes were examined. By comparing the data of similar points between the three meshes, it becomes clear how independent the solution is from the mesh. There are various methods to validate a grid independence test from numerical studies, testing with different orders of accuracy and the multiple mesh sizes. Accepted practice is to simply discuss on selected relevant parameters to the study using any method making note of the correlation or possible error (Roache et al., 1986; Slater, 2008). The grid independence test method used in this thesis is the three mesh method (Roache et al., 1986). Two locations were selected downstream of the hotplate at

the solid rear axle of the suspension to report the temperature values recorded across the three meshes. Fig. 4.27 shows the locations measured. Figs. 4.28, 4.29 and 4.30 show the difference in mesh sizing for the coarse, medium and fine meshes. The variance is easily seen in the smaller features of the underbody, such as the increased number of elements representing the small area behind the hotplate and the solid beam axle. The coarse mesh had approximately 6 million elements, with the medium mesh having 15 million, and the fine mesh with 28 million elements. The coarse mesh finished simulating in about a week, the medium mesh in two weeks, and the fine mesh in five weeks.

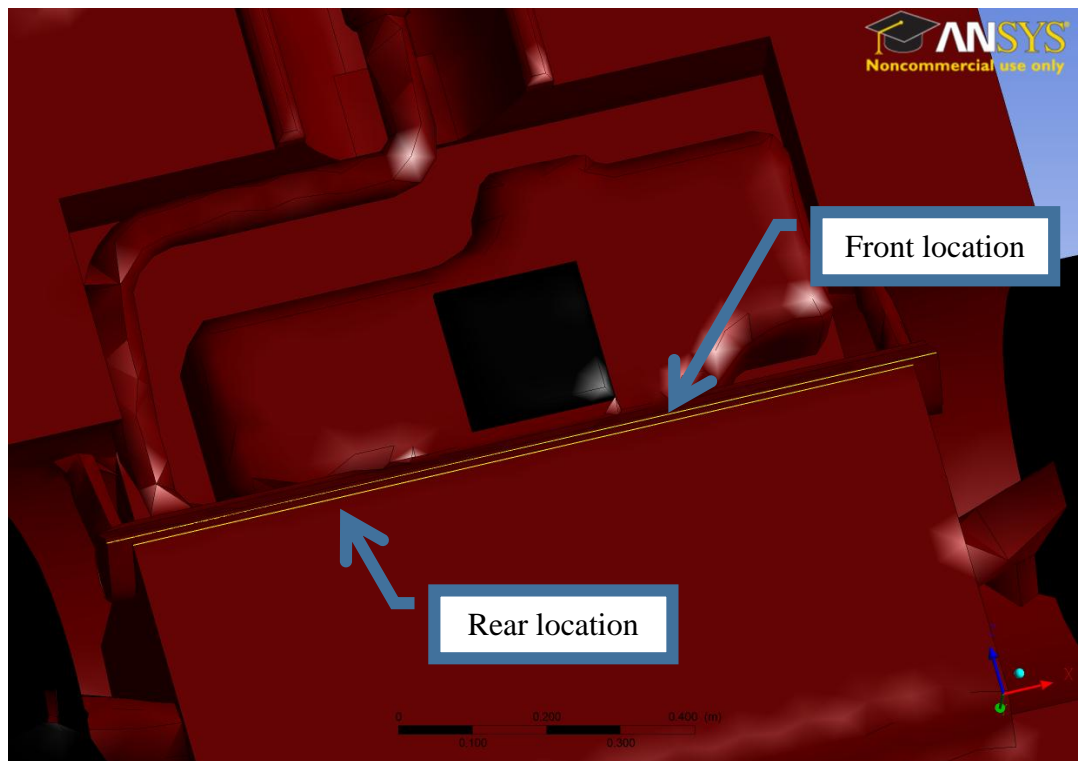


Figure 4.27: Showing the locations used for the grid independence test. The yellow lines indicate the locations data was compared across.

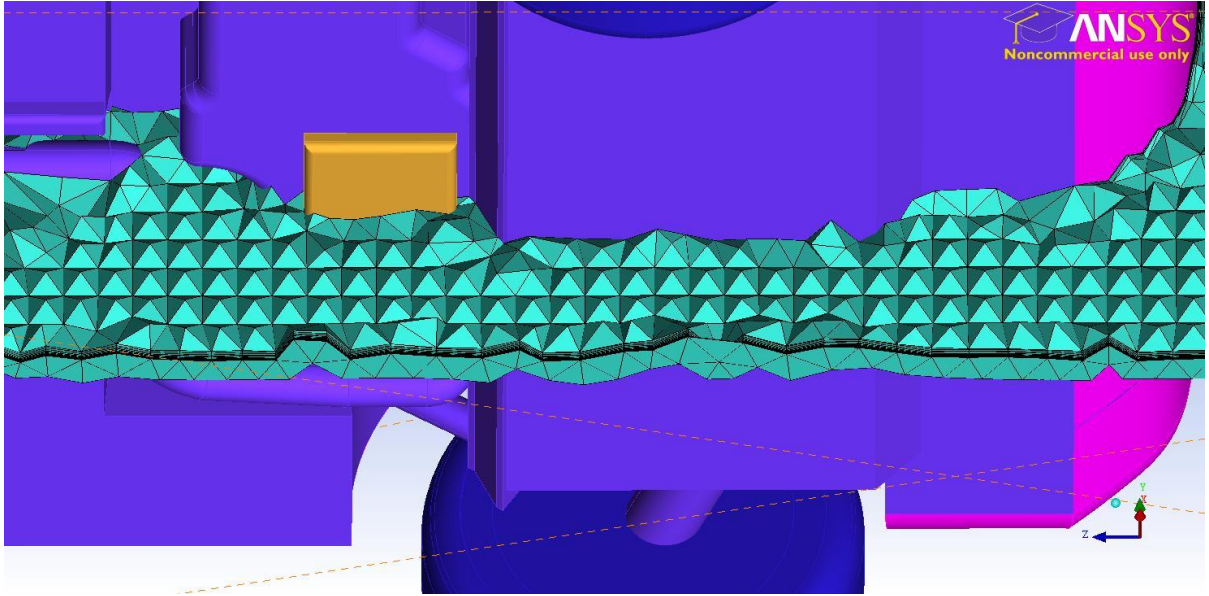


Figure 4.28: Coarse mesh of the vehicle.

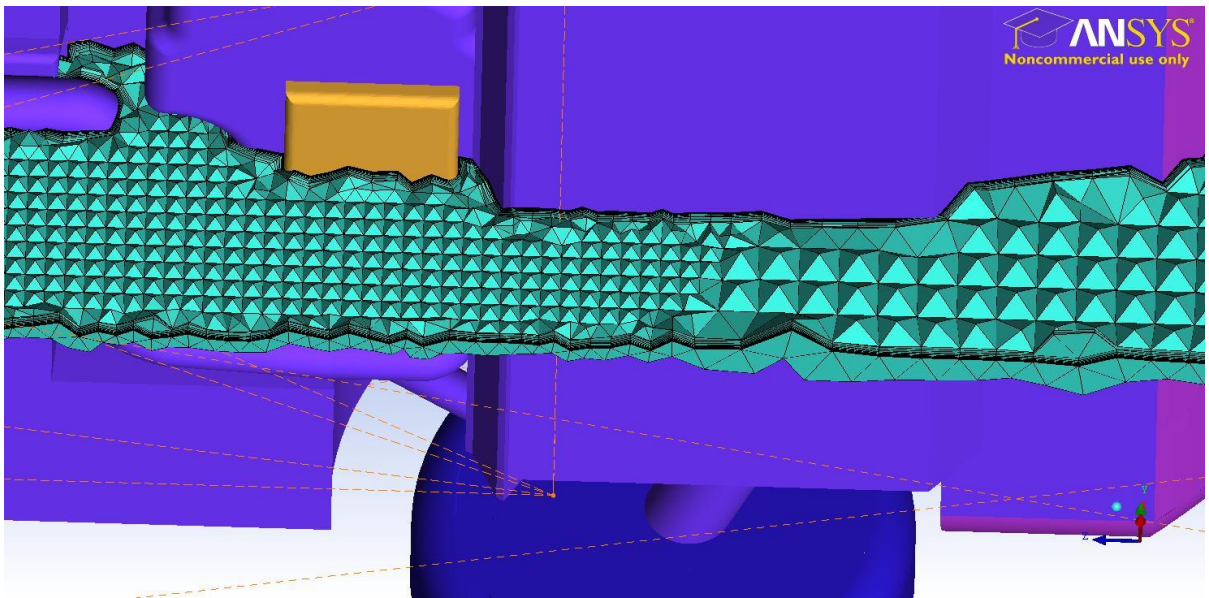


Figure 4.29: Medium mesh of the vehicle.

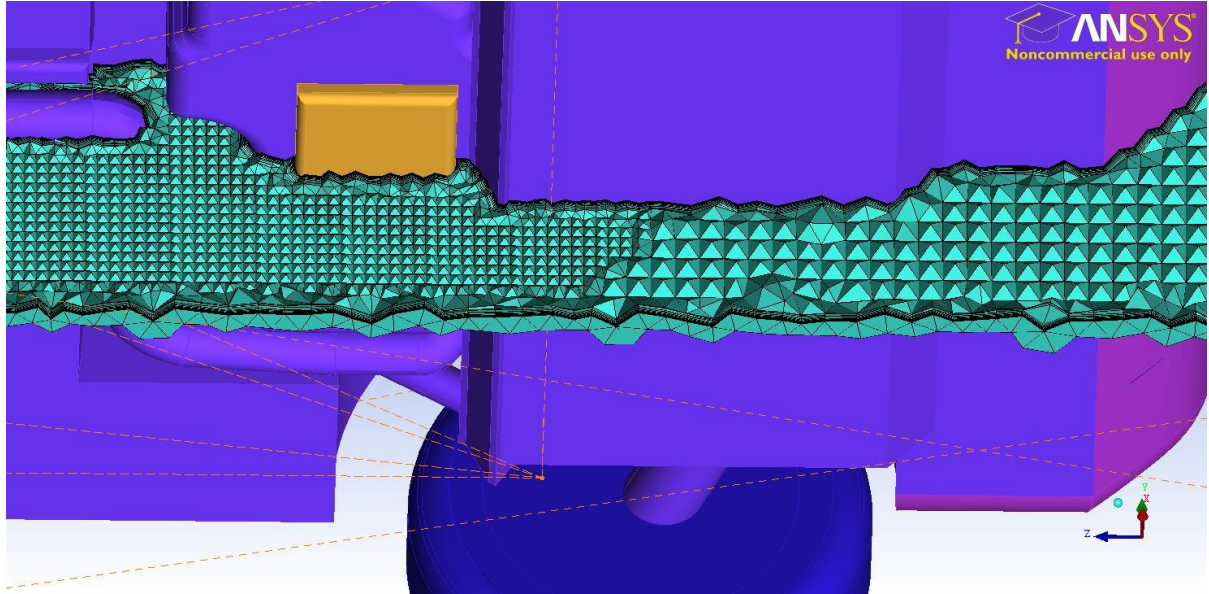


Figure 4.30: Fine mesh of the vehicle.

Figures 4.31 and 4.32 show the results from the grid independence test at the two measured locations. The coarse mesh barely registers the temperature increase immediately behind the hotplate in either situation. The fine mesh captures the temperature increase in both locations over a larger area and with a softer gradient, likely as a result of more elements providing information along the length. Compared to the fine mesh, the medium mesh notes the effect of the hotplate in a slightly different location, with the maximum temperature noted for the front location being under-estimated by 1.5K for the front location and over-estimated by 1K in the rear location. This variance could be a result of how ICEM partitioned the domain near the hotplate, but the trends observed are roughly the same and with an error of 0.5% when comparing maximum values between the medium and fine meshes. This is far less than the ten percent error as accepted in CFD practice (Karniadakis and Sherwin, 2005), thus the medium mesh is sufficiently independent of the solution. In addition to this, the drastic time savings between the medium and fine cases, with the fine mesh requiring 150% more time to simulate to a similar level, it was decided

that to save on computational time a medium mesh approach was taken for the rest of the numerical test cases.

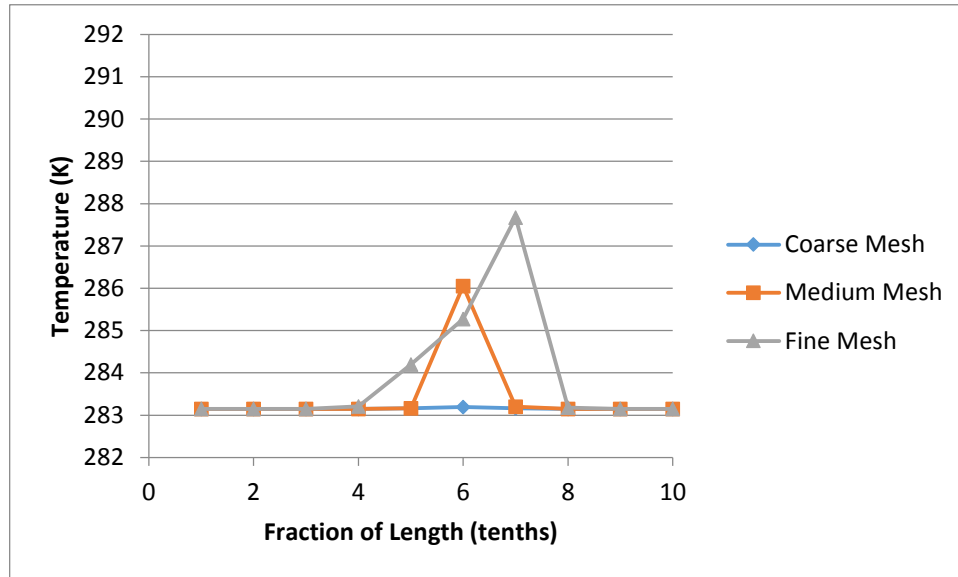


Figure 4.31: Grid independence test illustrating the temperature along the front location of the solid rear axle.

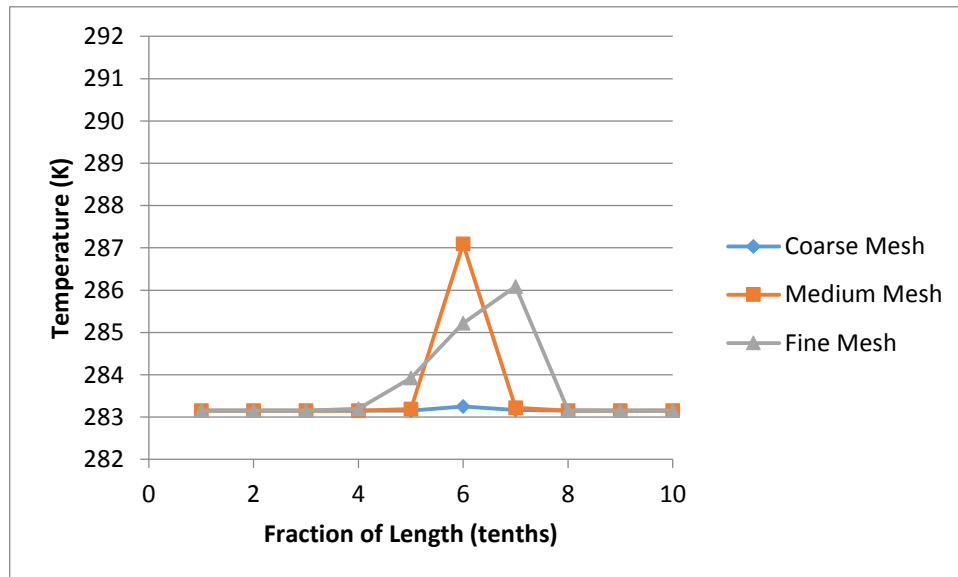


Figure 4.32: Grid independence test illustrating the temperature along the rear location of the solid rear axle.

4.2.3: Numerical Results

Four cases were numerically simulated in Fluent. In order of increasing yaw angle, these four cases are reported in Table 1 as Test 1 (0° yaw, 50 km/h wind speed, 10°C ambient temperature), Test 7 (8° yaw, 100 km/h wind speed, 10°C ambient temperature), Test 8 (15.6° yaw, 100 km/h wind speed, 10°C ambient temperature) and Test 3 (29.2° yaw, 50 km/h wind speed, 10°C ambient temperature).

The results are first reported in terms of the temperature contours at the vehicle centreline and at the location of the thermocouples (5mm from the vehicle surface) as well as isosurface plots. Velocity results are then discussed through contours at the vehicle centreline and streamlines close to the vehicle surface.

4.2.3.1: Thermal Results

Figures 4.33 and 4.34 illustrate the temperature contours for Test 1 (0° yaw, 50 km/h, 10°C ambient temperature) in various planes and degrees of zoom, such as looking at the vehicle from the side profile to looking at the vehicle from the top.

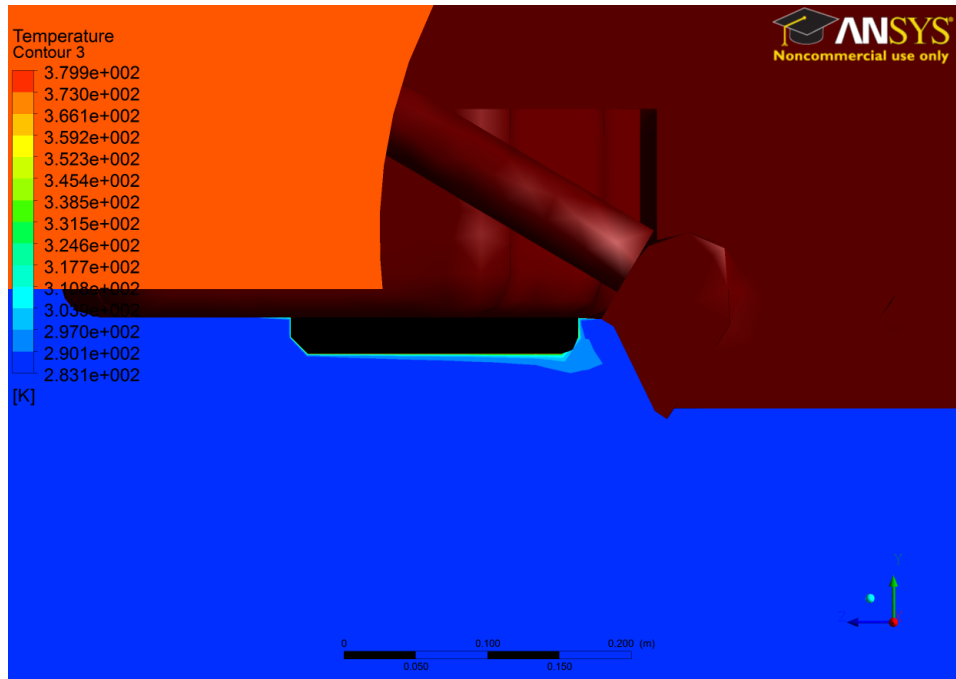


Figure 4.33: A zoomed in view of the temperature contours at the vehicle centerline from the side profile for Test 1.

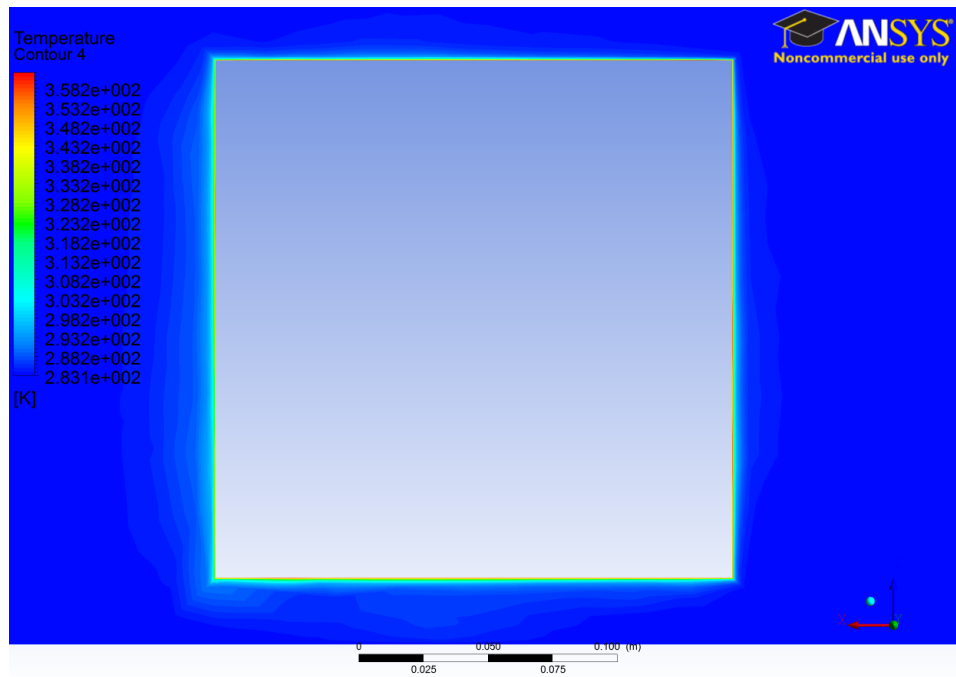


Figure 4.34: Zoomed in view of the temperature contours 5 mm below the surface of the gas tank from the top view for Test 1.

Like the experimental data, it's clear that the heat convects away from the hotplate surface. Figure 4.33 shows how the air gets partially trapped in front of the solid axle suspension, making it difficult to easily convect away from the surface. Figure 4.34 shows that the convection effects are stronger than the radiation effects, as a larger gradient is seen in the direction of the flow (vertically on the diagram, where convection is stronger) than perpendicular to it (where radiative heat transfer would be stronger). Figure 4.33 also shows how the heat convects away in the direction perpendicular (in the heightwise direction, vertically in Fig. 4.33) to the hotplate surface. The heat convects away in a boundary layer, influenced by the velocity of the air and the fact the air heats up, reducing the temperature gradient as the air goes downstream along the hotplate.

Figures 4.35 and 4.36 illustrate the temperature contours for Test 7 (8° yaw, 100 km/h, 10°C ambient temperature).

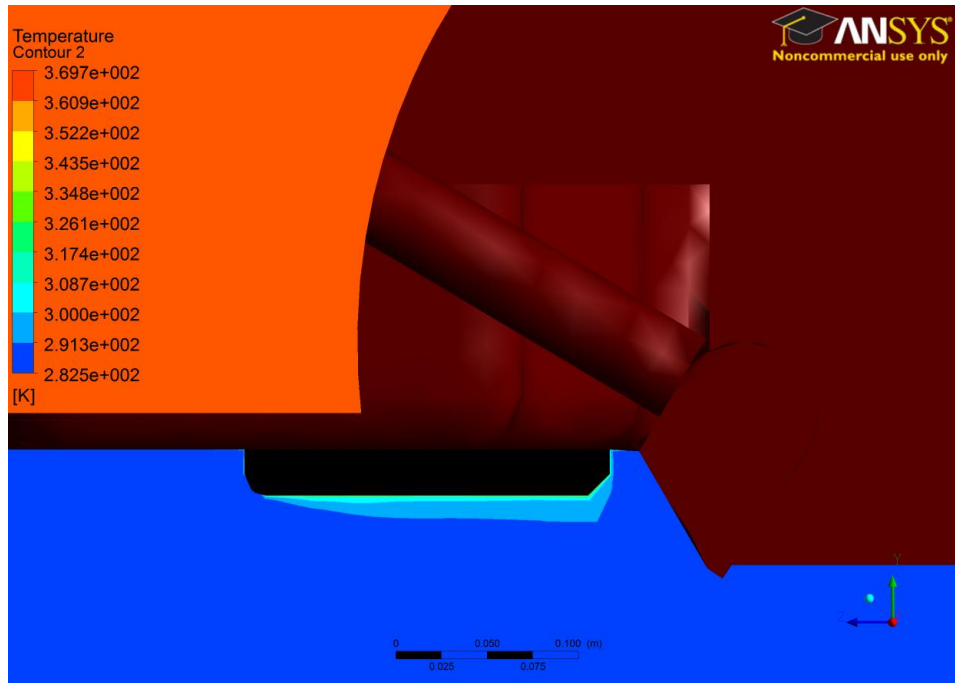


Figure 4.35: A zoomed in view of the temperature contours at the vehicle centerline from the side profile for Test 7.

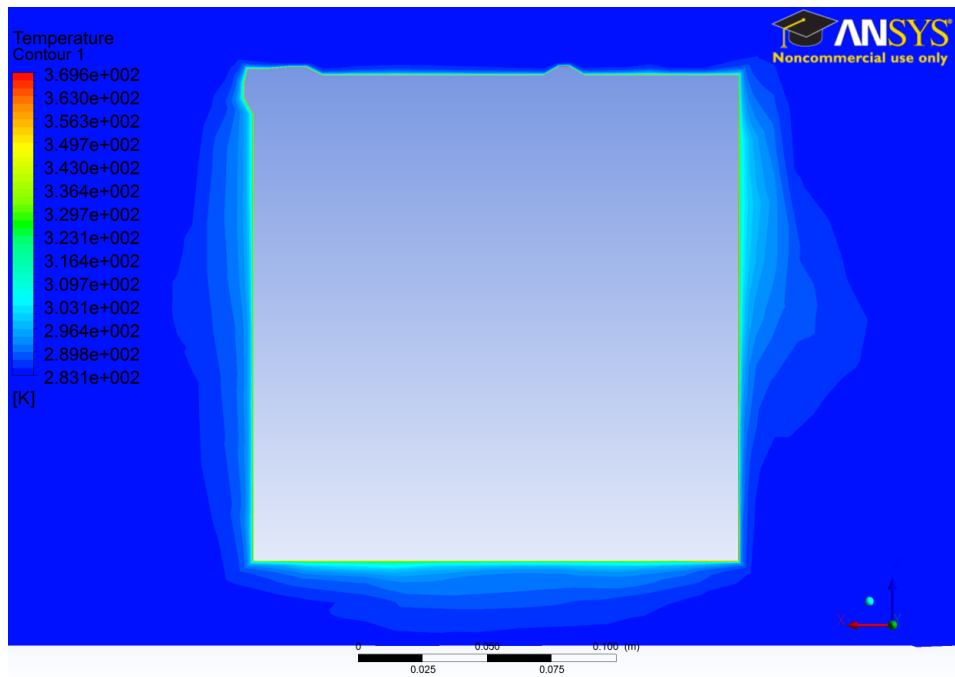


Figure 4.36: Zoomed in view of the temperature contours 5 mm below the surface of the gas tank from the top view for Test 7.

Similar to the experimental data, Fig. 4.36 demonstrates the heat convecting along the passenger side, likely due to the same reason as the experimental data – the driver side of the hotplate is in the way of the flow, thus the heat moves over the hotplate to the passenger side of the hotplate. Again, Fig. 4.35 shows the side profile with the heat also convected away from the hotplate perpendicular to the surface in a boundary layer fashion, with an even larger thermal boundary layer observed.

Figures 4.37 and 4.38 illustrate the temperature contours for Test 8 (15.6° yaw, 100 km/h, 10°C ambient temperature).

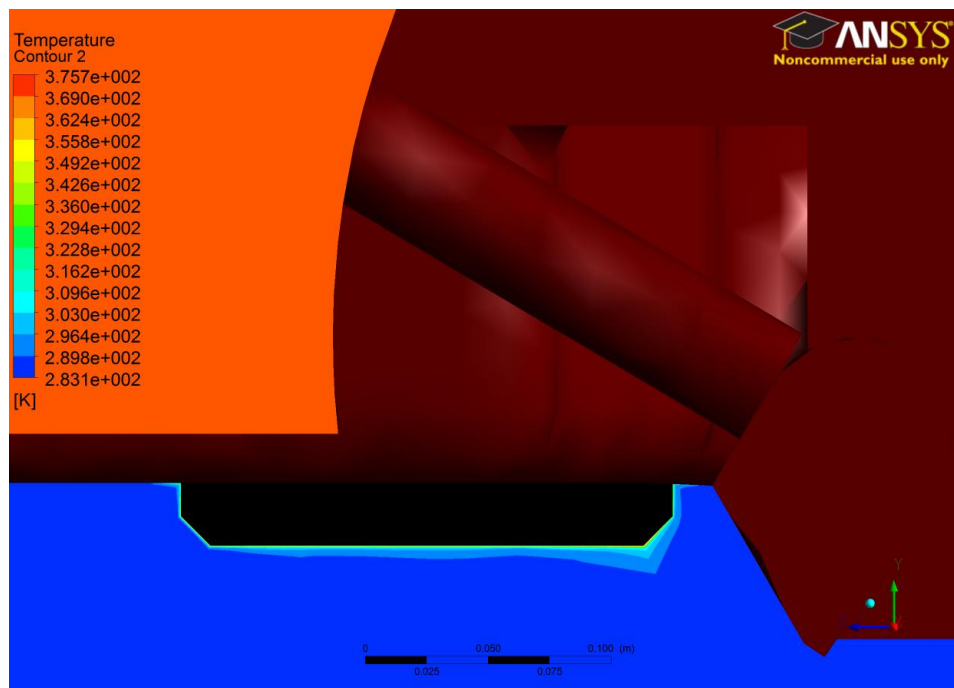


Figure 4.37: A zoomed in view of the temperature contours at the vehicle centerline from the side profile for Test 8.

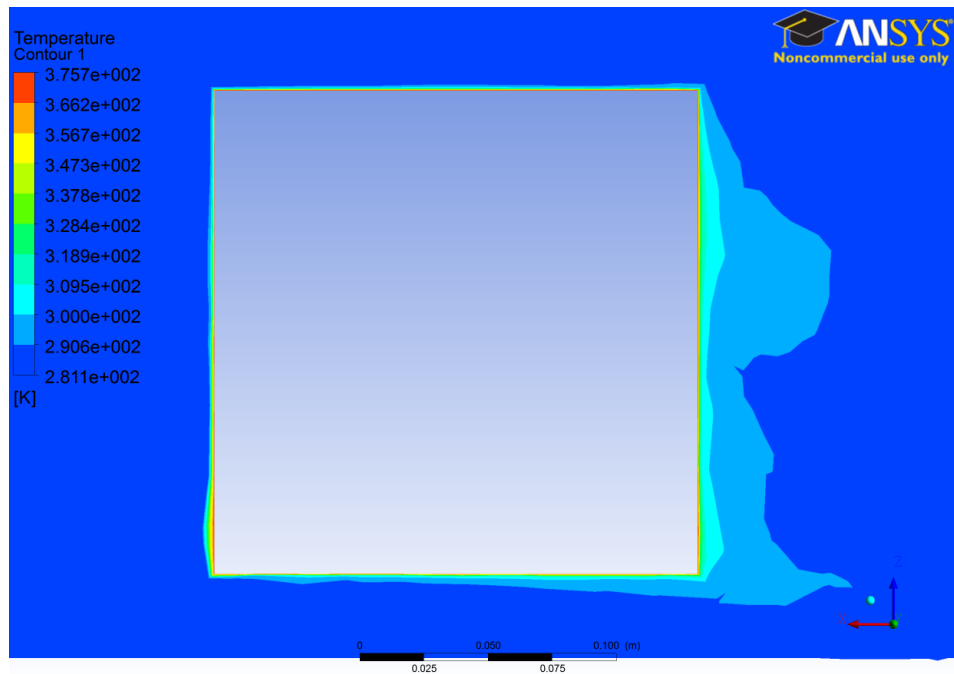


Figure 4.38: Zoomed in view of the temperature contours 5 mm below the surface of the gas tank from the top view for Test 8.

Like the experimental data, the heat convects along the passenger side. Through just the contours, it doesn't quite show why experimentally, the thermocouples on the passenger side in the upstream (towards the top of the figure) direction increased in temperature. The isosurface results later may give further insight.

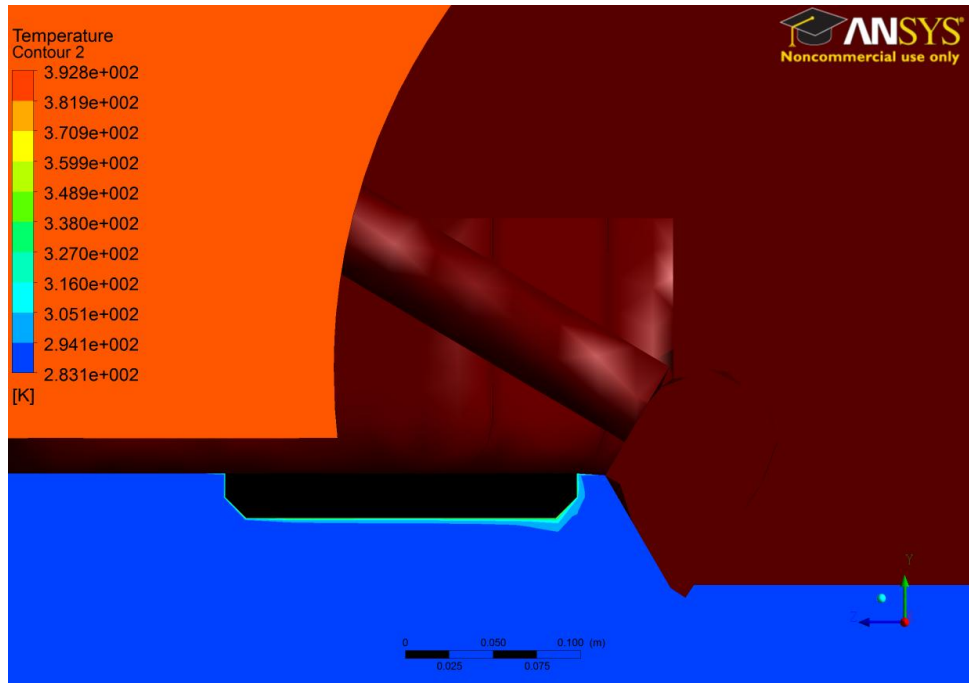


Figure 4.39: A zoomed in view of the temperature contours at the vehicle centerline from the side profile for Test 3.

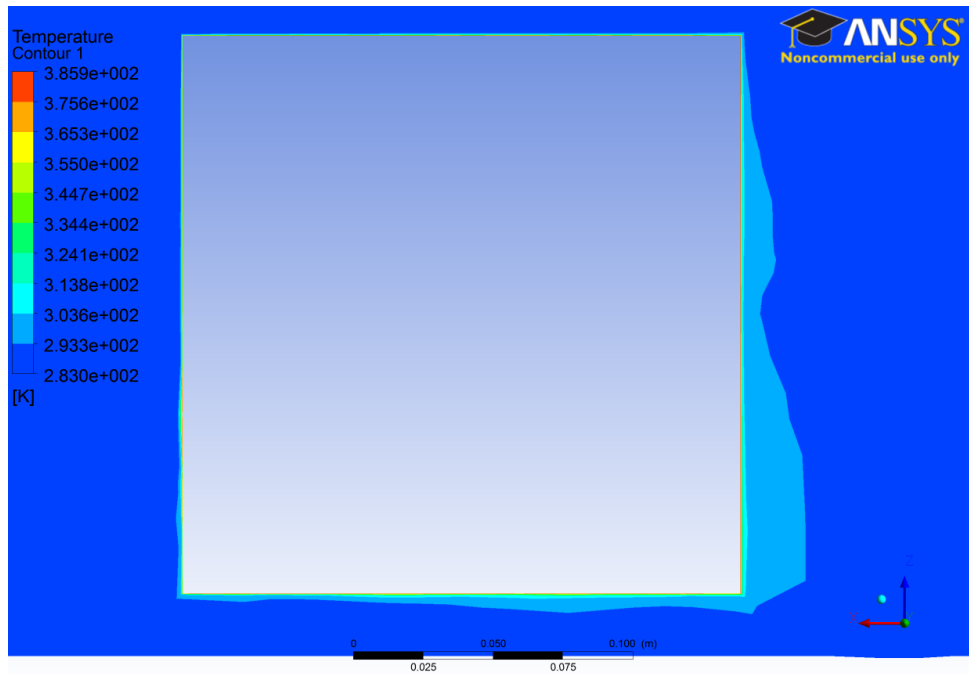


Figure 4.40: Zoomed in view of the temperature contours 5 mm below the surface of the gas tank from the top view for Test 3.

Figures 4.39 and 4.40 show the temperature contours for Test 3 at 29.2 yaw, 50 km/h and 10°C ambient temperature. Again, the heat convects to the passenger side, matching the experimental data. This lends credence to the fact that the hot plate would redirect the flow.

Figure 4.41 illustrates isosurfaces at various temperatures in order to show how the heat is convected away from the hotplate surface. The isosurfaces are at a.) 283.5K, b.) 285K, and c.) 290K for Test 1. These values were chosen to clearly illustrate the diffusion of heat away from the hotplate. It's clear through Fig. 4.41a, b and c that the heat that is convected away travels in the same direction of the flow, whereas some air gets trapped behind the solid rear beam axle as shown by the contours as well. This trapped heat is shown clearly in Fig. 4.41c, with the high temperature heat encountering the obstruction and not being able to convect over it. As expected, the hotter temperatures are closer to the heat source, whereas the colder air diffuses out further behind the car.

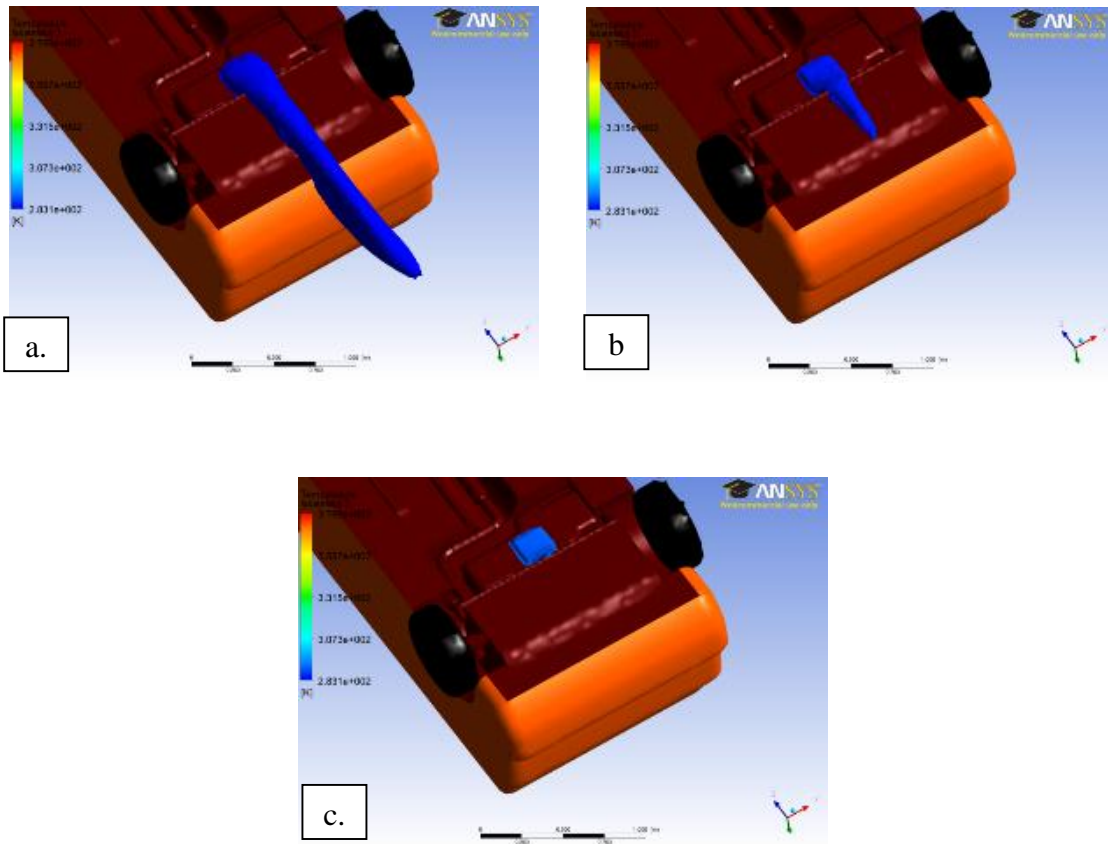


Figure 4.41: Temperature isosurfaces at a.) 283.5K, b.) 285K, c.) 290K for Test 1.

Figure 4.42 illustrates isosurfaces for Test 7 at a.) 283.5K, b.) 285K, and c.) 290K. Figure 4.42a and b gives some additional insight into how the heat is convected away further from the hotplate: the heat travels in the same direction of the flow, likely because the hotplate no longer obstructs the flow further away from it. Figures 4.42b and c again show how the higher temperatures are closer to the heat source, whereas the colder temperatures of Figure 4.42a extend further behind in the car and in the direction of the flow. The isosurface of Fig. 4.42a shows various deformities when compared to Fig. 4.41a and the 0° yaw case; this distorted isosurface could be a result of the increased turbulence in the air due to the increasing yaw angle.

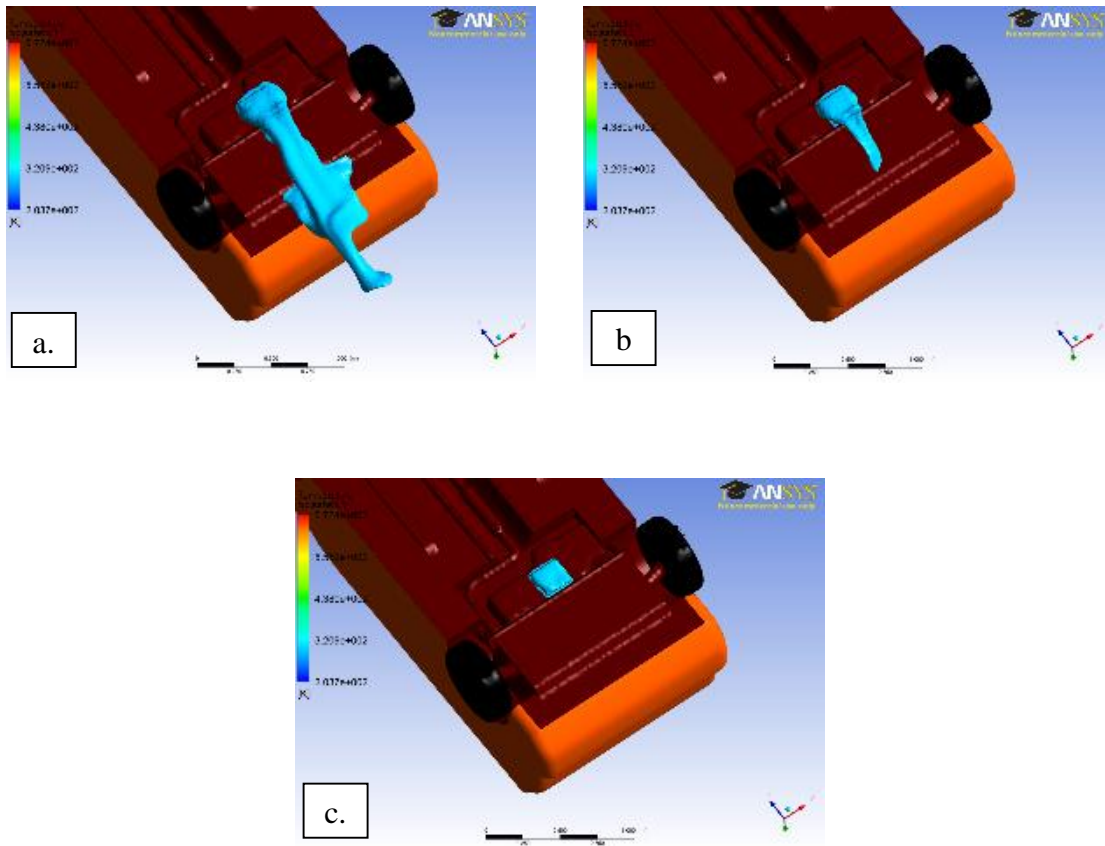


Figure 4.42: Temperature isosurfaces at a.) 283.5K, b.) 285K, c.) 290K for Test 7.

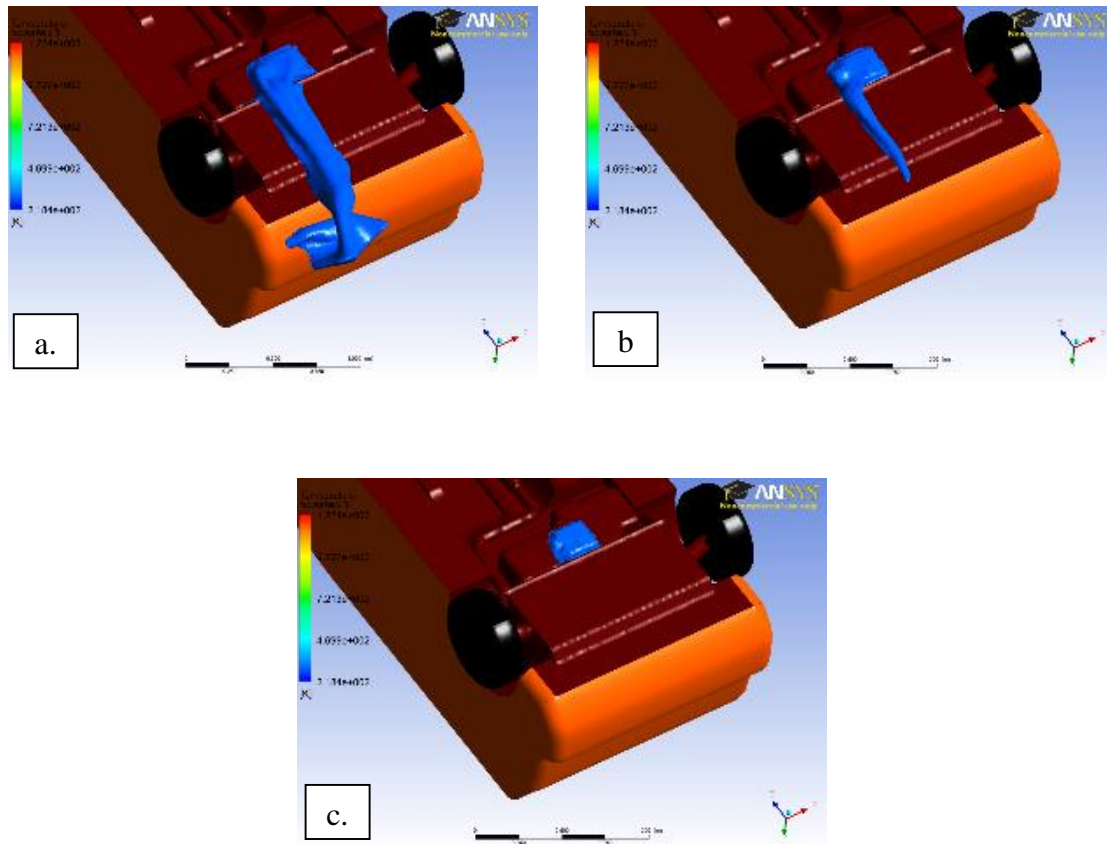


Figure 4.43: Temperature isosurfaces at a.) 283.5K, b.) 285K, c.) 290K

Looking at the isosurfaces of Figs. 4.42 and 4.43 give greater insight into Test 8 and the experimental results: at the 15 degree yaw angle, the heat appears to curve around the hot plate instead of following the angle of the flow at 8 degree yaw, carrying more heat to the passenger side. It is speculated this occurs due to the asymmetry of the gas tank; perhaps this is some sort of ideal angle for the air to glance off of the gas tank towards the hotplate that causes this temperature distribution to result. All three figures exhibit this behaviour, suggesting a very large change in the underbody flow to affect even the hotter core that was unaffected by turbulence in Test 7.

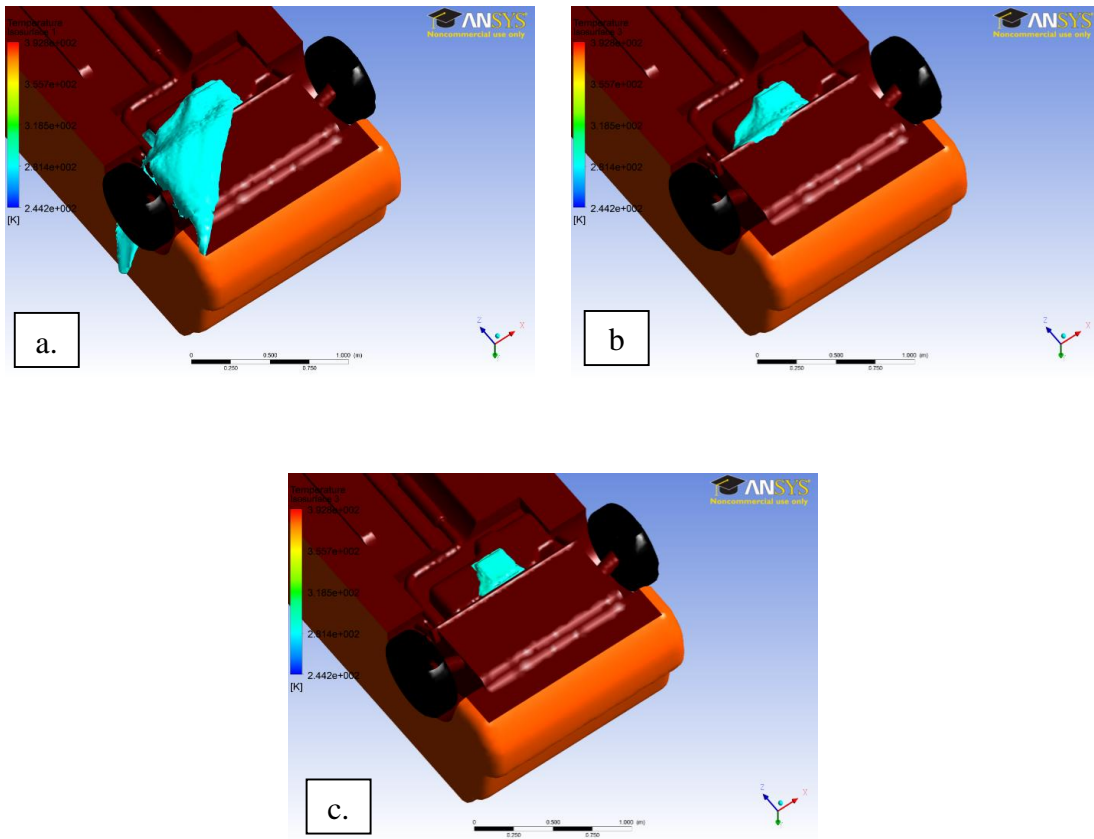


Figure 4.44: Temperature isosurfaces at a.) 283.5K, b.) 285K, c.) 290K for Test 3.

Figure 4.44 shows the isosurfaces for Test 3. With the this large yaw angle the flow greatly redirects the heat, with Figure 4.44 showing the air at 283.5K even reaching the wheel well. Figures 4.44b and c show again how the solid beam axle blocks the heat from convecting over it.

4.2.3.2: Velocity Results

Figures 4.45 to 4.47 show the velocity contours at the vehicle centreline for Test 1. The contours depict the nature of the flow around the vehicle and confirm expected patterns: the flow hits the front of the vehicle, stops, and then separates to over and under the vehicle. Under the vehicle, the flow is slower than over the vehicle, due to the obstructions there.

Behind the vehicle, there is a wake resulting from the air separating at the base of the vehicle, as the air does not immediately mix with the dead water behind the vehicle. Being at 0 degrees yaw, the top view shows how the wake is formed fairly symmetrically. The slight differences are likely a result of the asymmetrical underbody design.

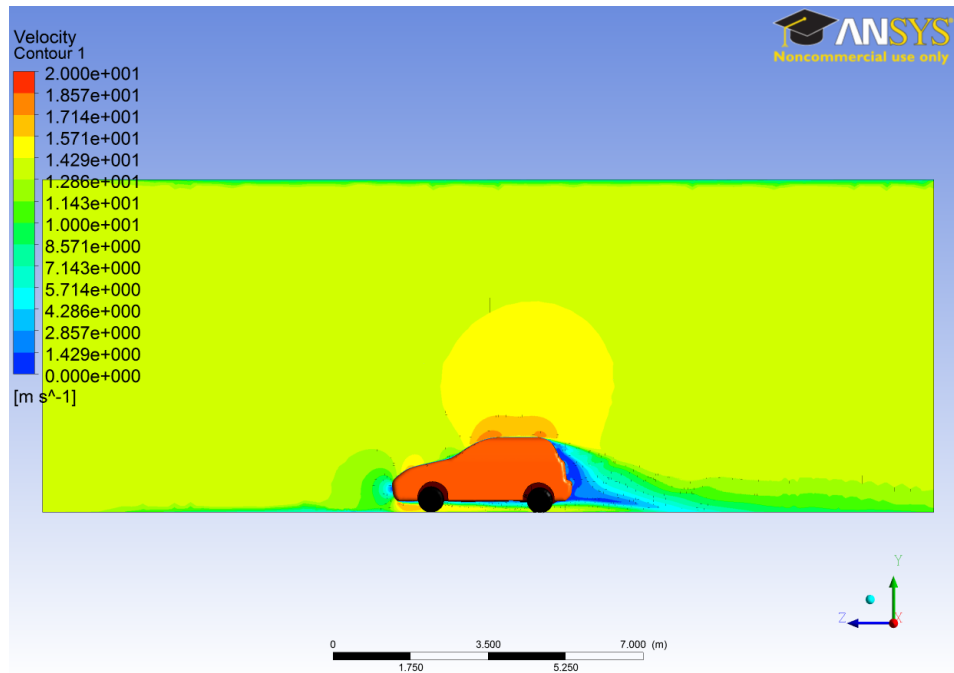


Figure 4.45: Velocity contours at the vehicle centreline from the side profile for Test 1.

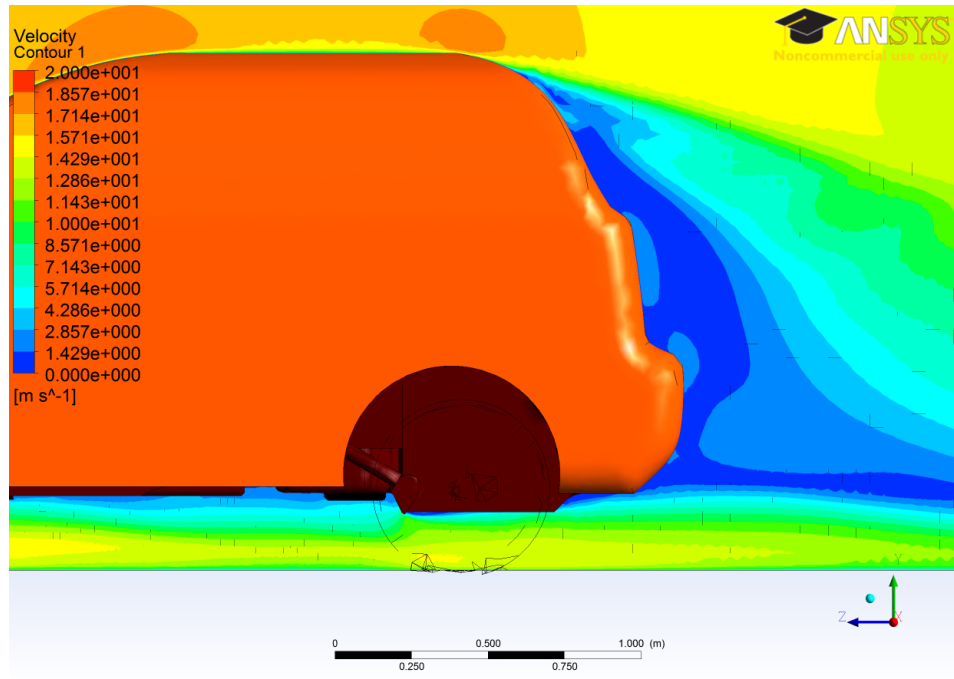


Figure 4.46: Zoomed in view of velocity contours at the vehicle centreline from the side profile for Test 1.

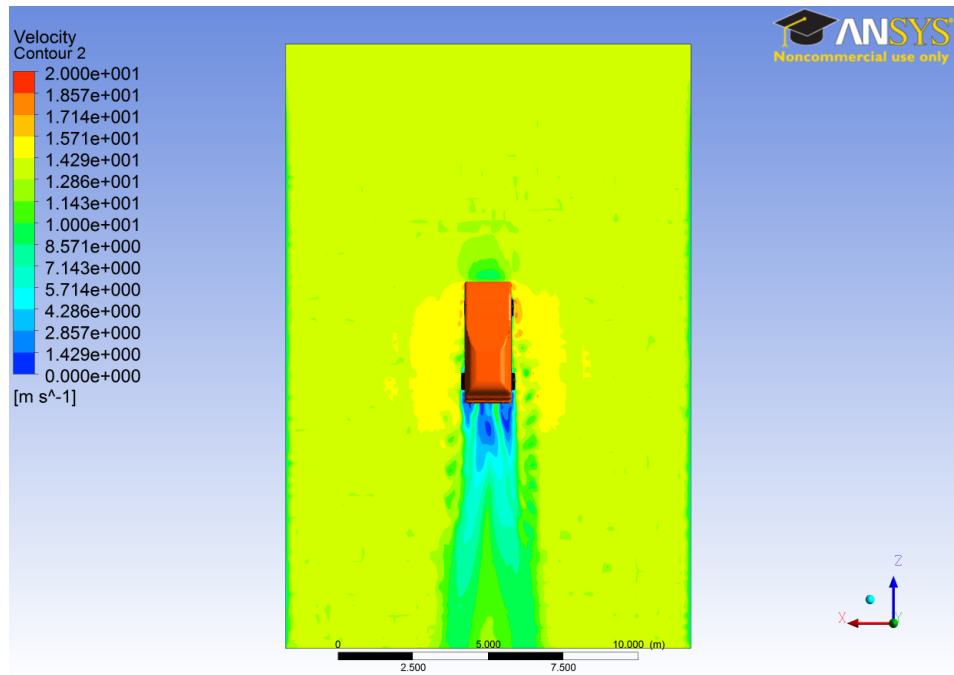


Figure 4.47: Velocity contours 5 mm below the gas tank from the top view for Test 1.

Figures 4.48 to 4.50 show the velocity contours at the vehicle centreline for Test 7. Being at the centreline and at 8 degrees yaw, the contours are not on a symmetrical (or at least near symmetrical) plane. The contours of Figs. 4.48 and 4.49 show multiple recirculation regions which are vortices that will be easier to see using streamlines. Figure 4.50 illustrates the top view of the velocity contours, which clearly show how the wake is affected by yaw angle – the wake begins to form from the front passenger side corner due to the yaw angle this area of the vehicle obstructs the flow.

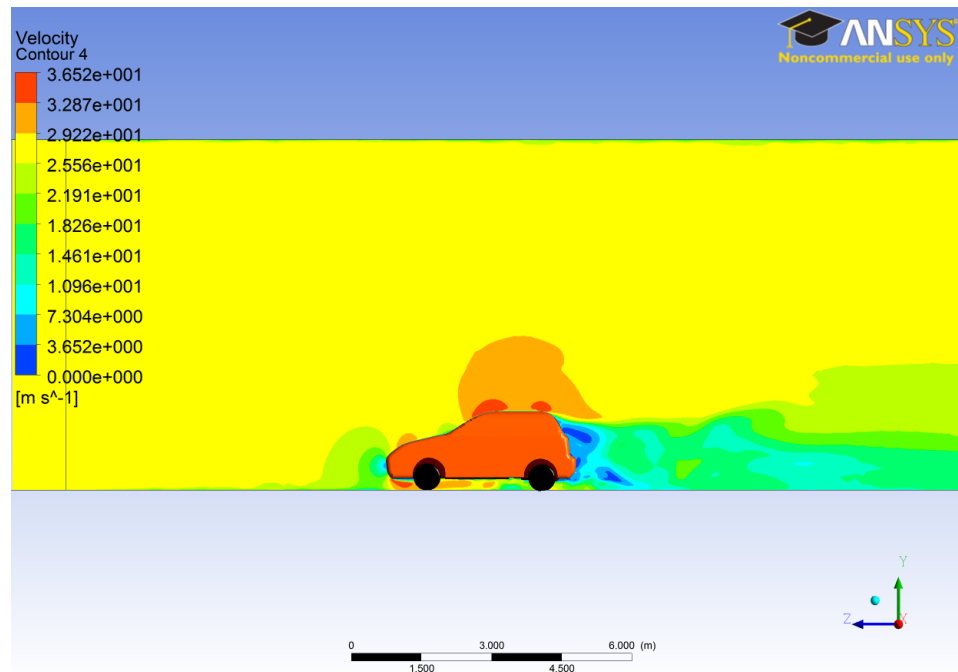


Figure 4.48: Velocity contours at the vehicle centreline from the side profile Test 7.

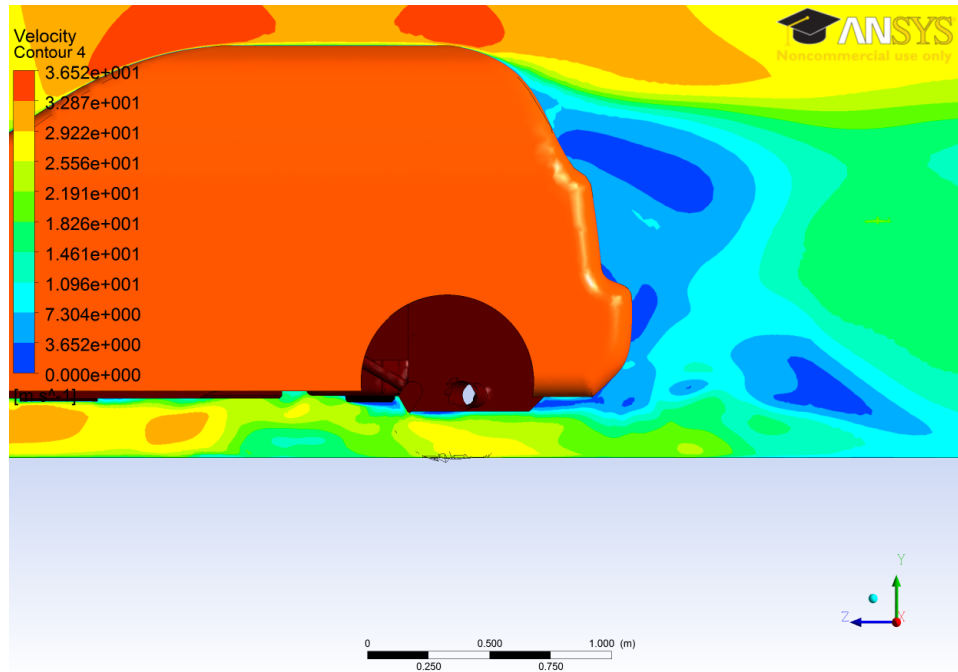


Figure 4.49: Zoomed in view of velocity contours at the vehicle centreline from the side profile for Test 7.

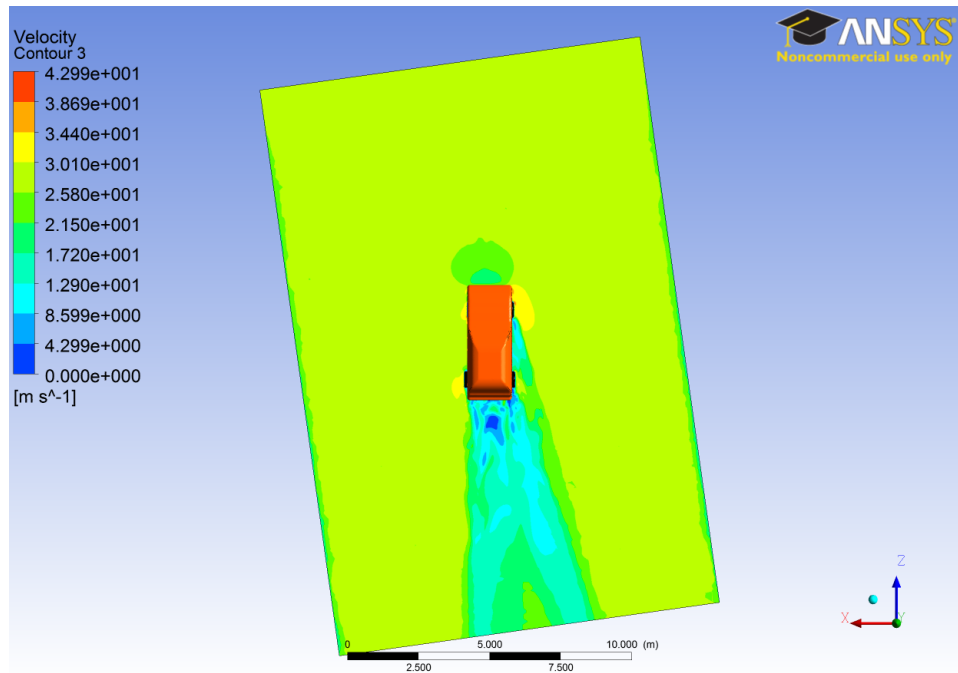


Figure 4.50: Velocity contours 5 mm below the gas tank from the top view for Test 7.

Figures 4.51 to 4.53 show the velocity contours at the vehicle centreline for Test 8. Being at the centreline and at 15.6 degrees yaw, the contours are again not on a symmetrical plane and have similar results to the contours at 8 yaw. The contours of Figs. 4.51 and 4.52 also show multiple recirculation regions which are vortices that will be easier to visualize from the streamlines. Figure 4.53 illustrates the top view of the velocity contours, which clearly show how the wake is affected by yaw angle – the wake begins to form from the front passenger side corner as due to the yaw angle this area of the vehicle obstructs the flow, again similar to the 8 degree yaw case but with a larger wake with the higher yaw angle. Interestingly a small wake off of the front passenger tire is formed and resolved, likely due to the sloping front hood of the vehicle allowing mixing of freestream air into the wake, controlling the size.

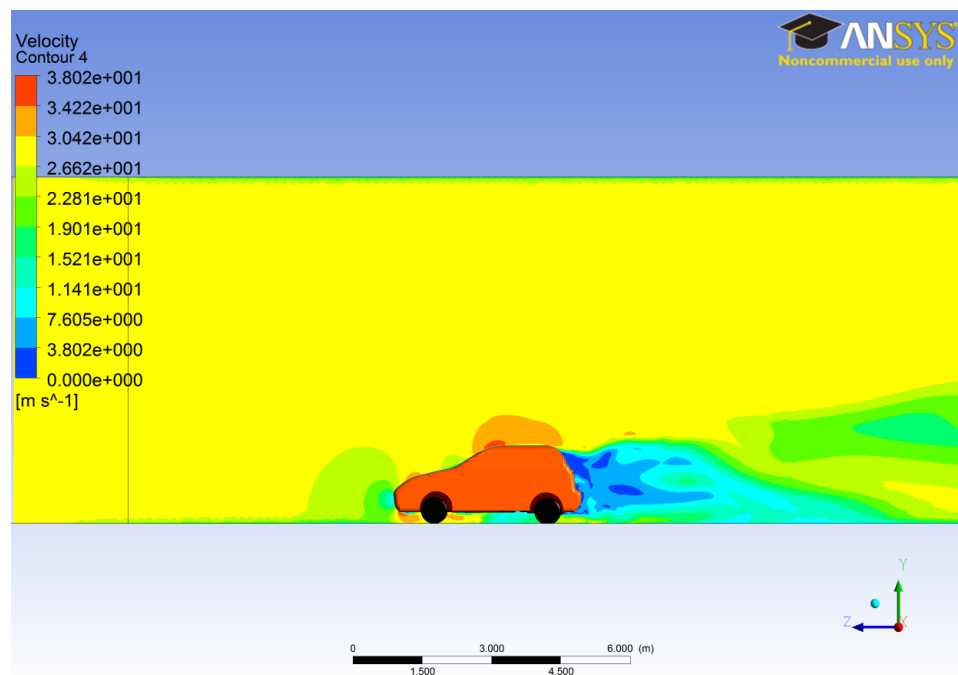


Figure 4.51: Velocity contours at the vehicle centreline from the side profile for Test 8.

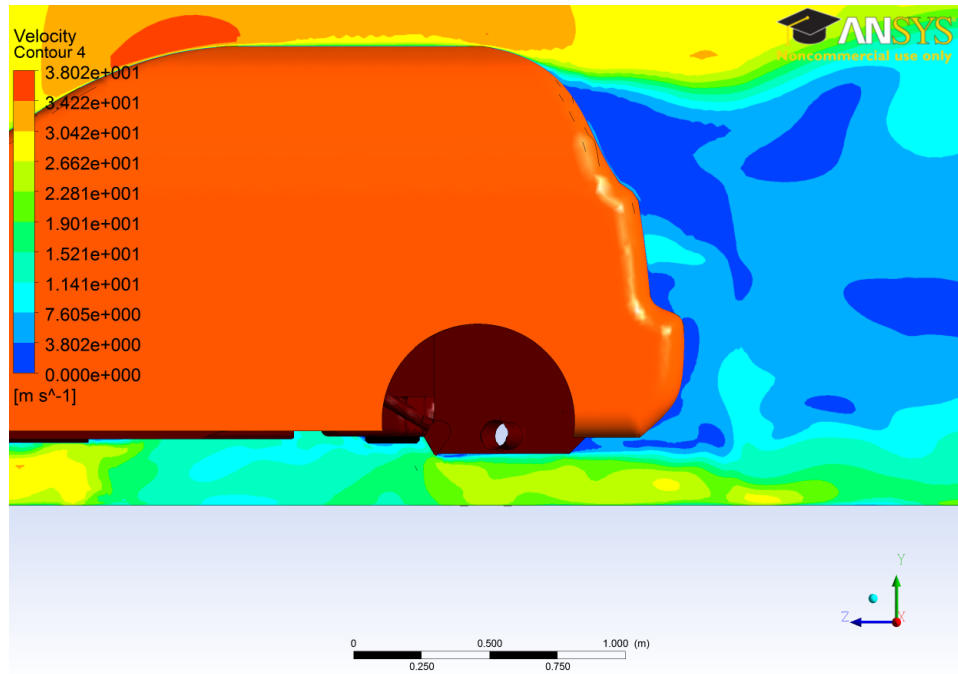


Figure 4.52: Zoomed in view of velocity contours at the vehicle centreline from the side profile for Test 8.

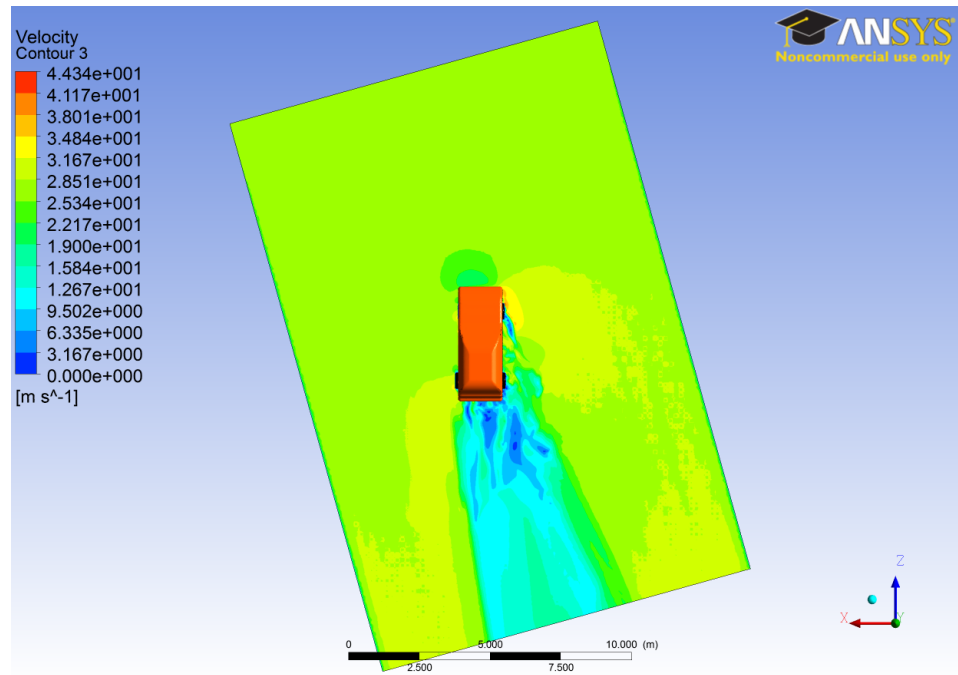


Figure 4.53: Velocity contours 5mm below the gas tank from the top view Test 8.

Figures 4.54 to 4.56 show the velocity contours at the centreline and 5mm underneath the gas tank for Test 3. At the centreline, due to the numerical setup of the domain, the air is channeled towards the rear driver's side corner of the domain, in which the air deflects off the wall and redirects to the outlet. This leads to the high velocity seen towards the exit of the domain. Around the vehicle, large recirculation zones are seen coming off the tires and rear of the vehicle as shown in Fig. 4.56.

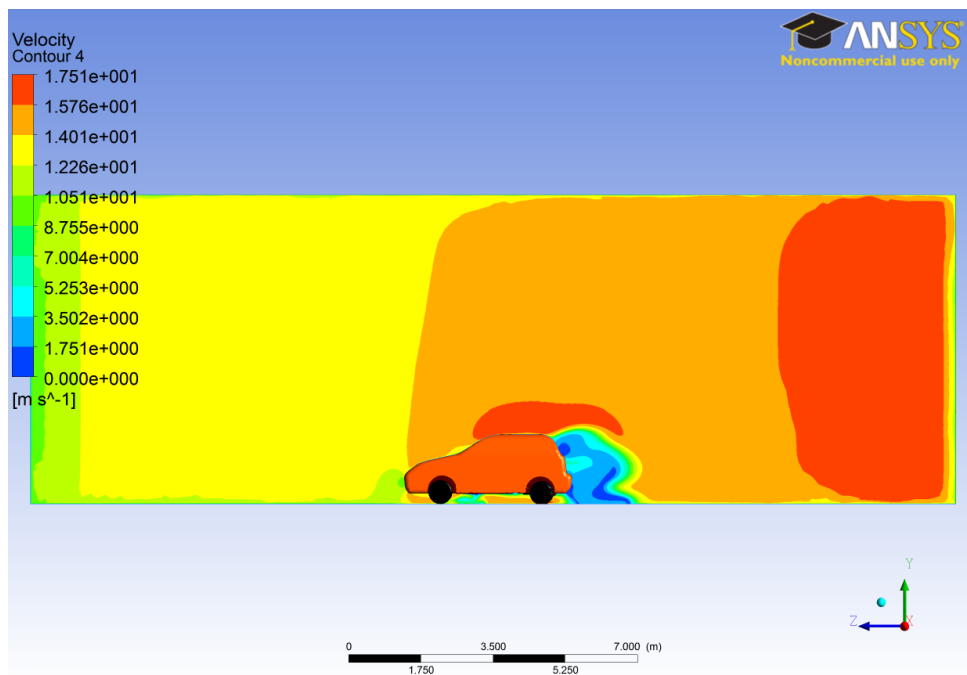


Figure 4.54: Velocity contours at the vehicle centreline from the side profile for Test 3.

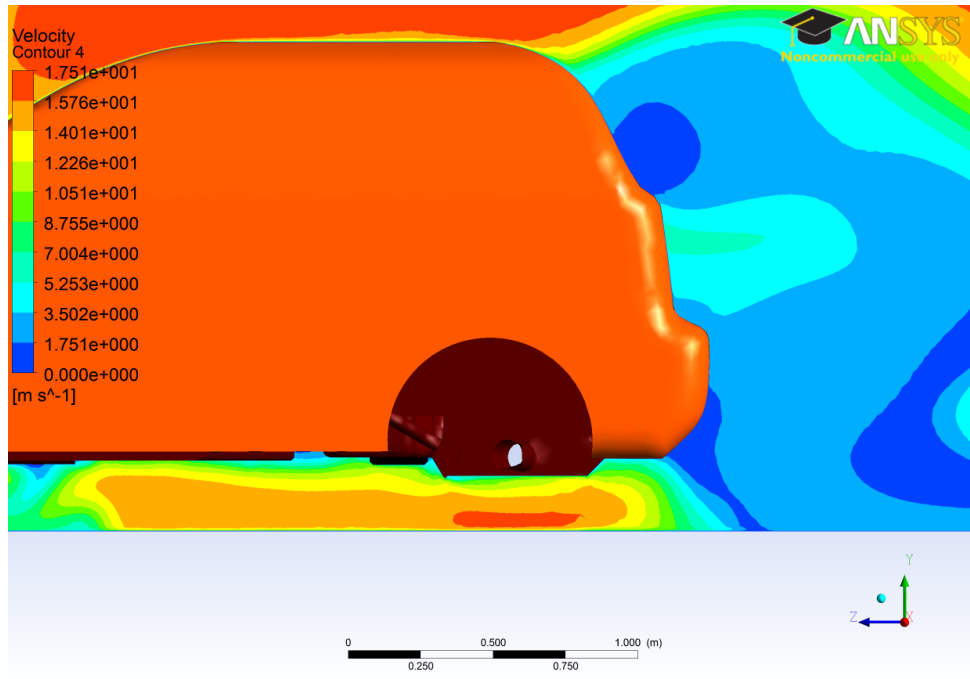


Figure 4.55: Zoomed in view of velocity contours at the vehicle centreline from the side profile for Test 3.

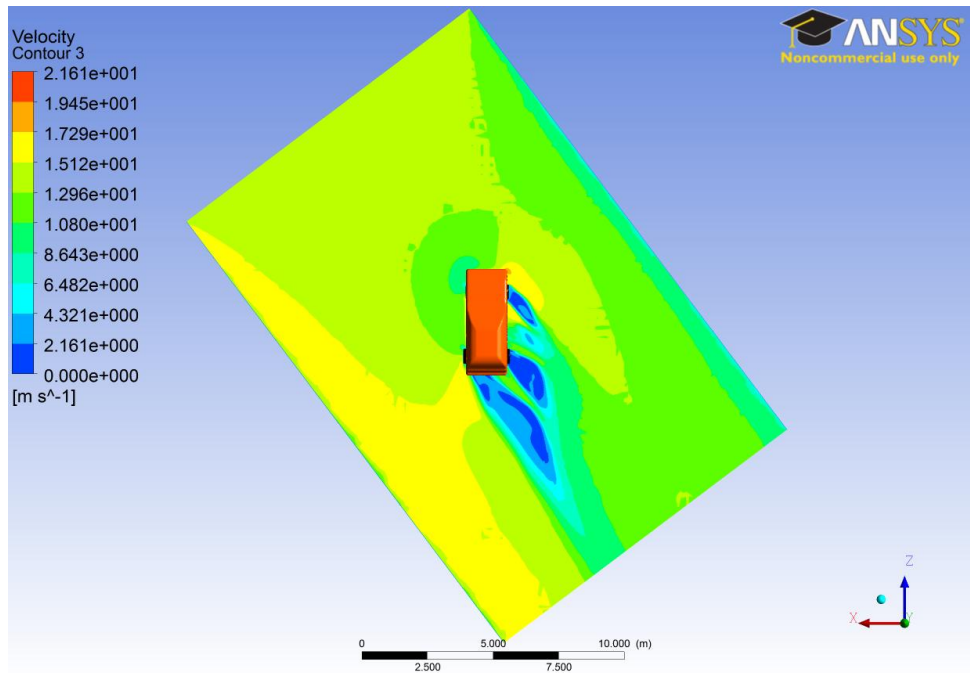


Figure 4.56: Velocity contours 5 mm below the gas tank from the top view Test 8.

Figure 4.57 shows streamlines of the flow around the vehicle in various views from a.) in front of the vehicle, b.) behind the vehicle, c.) under and d.) over the vehicle for Test 1. The streamlines illustrate in three dimensions how the flow moves around the vehicle. The air around the top of the vehicle and the sides of the vehicle are fairly organized as shown in Fig. 4.57a and b. Under the vehicle, the flow is relatively more disorganized compared to the sides and the top due to the obstructions underneath the vehicle. The tufts under the vehicle in the experimental case show some correlation with the streamlines under the vehicle, showing the flow under the vehicle roughly following the direction of the flow, with some effects by the geometry imparting some local effects.

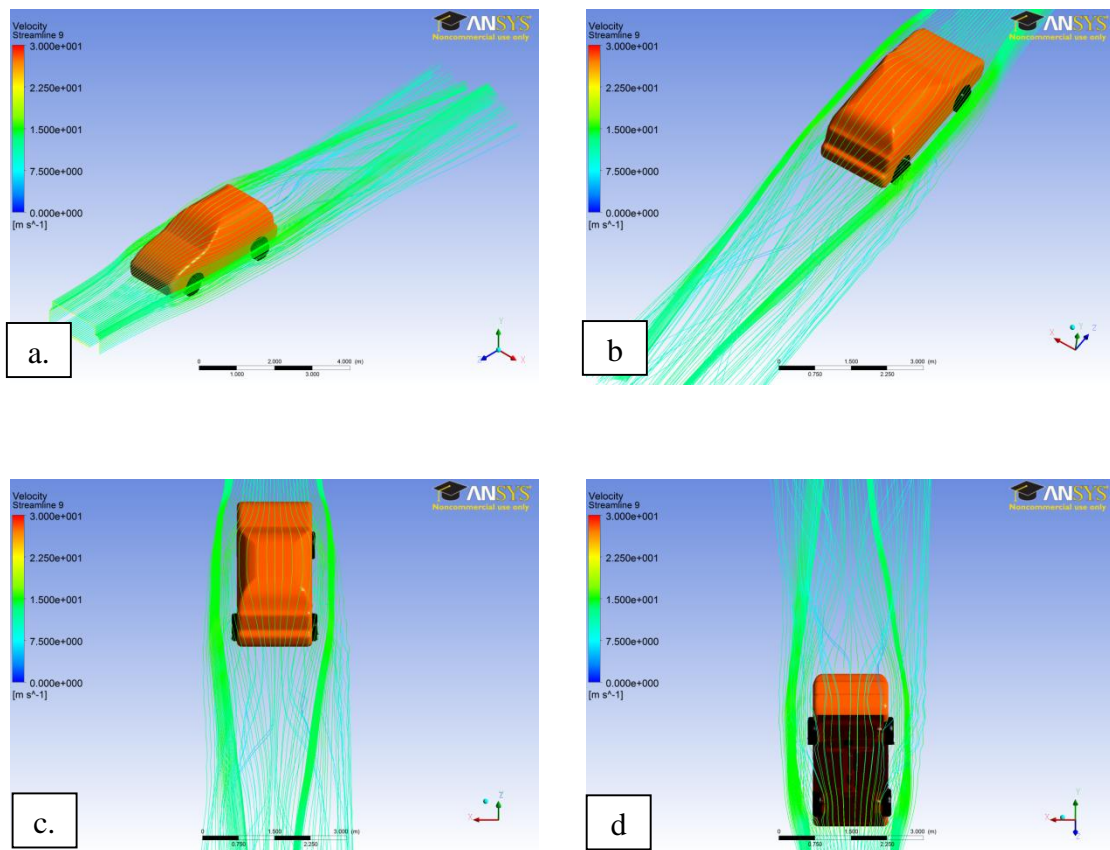


Figure 4.57: Velocity streamlines a.) in front of the vehicle, b.) behind the vehicle, c.) over and d.) under the vehicle for Test 1.

Figure 4.58 shows streamlines of the flow around the vehicle in various views from a.) in front of the vehicle, b.) behind the vehicle, c.) over and d.) under the vehicle for the 8 degrees yaw case. The streamlines illustrate in three dimensions the vortices seen in 4.48 and 4.49 with large vortices coming off of the driver side of the vehicle. Smaller vortices come from the passenger side, likely due to the low sloping hood of the vehicle that allows the free stream air to interact with the wake, absorbing some of the energy in the vortices and breaking them up.

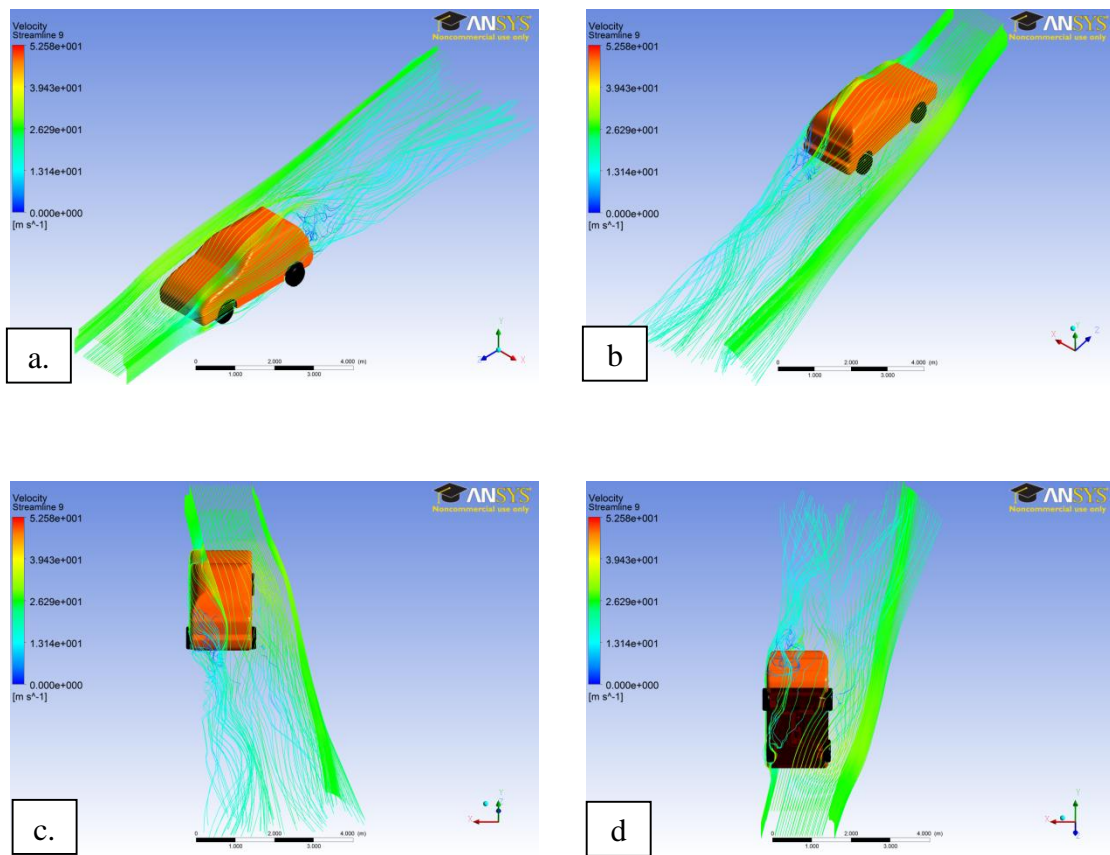


Figure 4.58: Velocity streamlines a.) in front of the vehicle, b.) behind the vehicle, c.) over and d.) under the vehicle for Test 7.

Figure 4.59 shows streamlines of the flow around the vehicle for Test 8 in various views from a.) in front of the vehicle, b.) behind the vehicle, c.) over and d.) under the vehicle. The streamlines illustrate in three dimensions the vortices seen in Figs. 4.51 and 4.52, with large vortices coming off of the driver side of the vehicle. Again, smaller vortices come off of the passenger side, likely due to the low sloping hood of the vehicle that allows the free stream air to interact with the wake, absorbing some of the energy in the vortices and breaking them up. Underneath the body there is even more disturbance of the flow with increasing yaw angle compared to the 8 degree yaw case, with the front driver side tire interacting with the flow ahead of the hotplate.

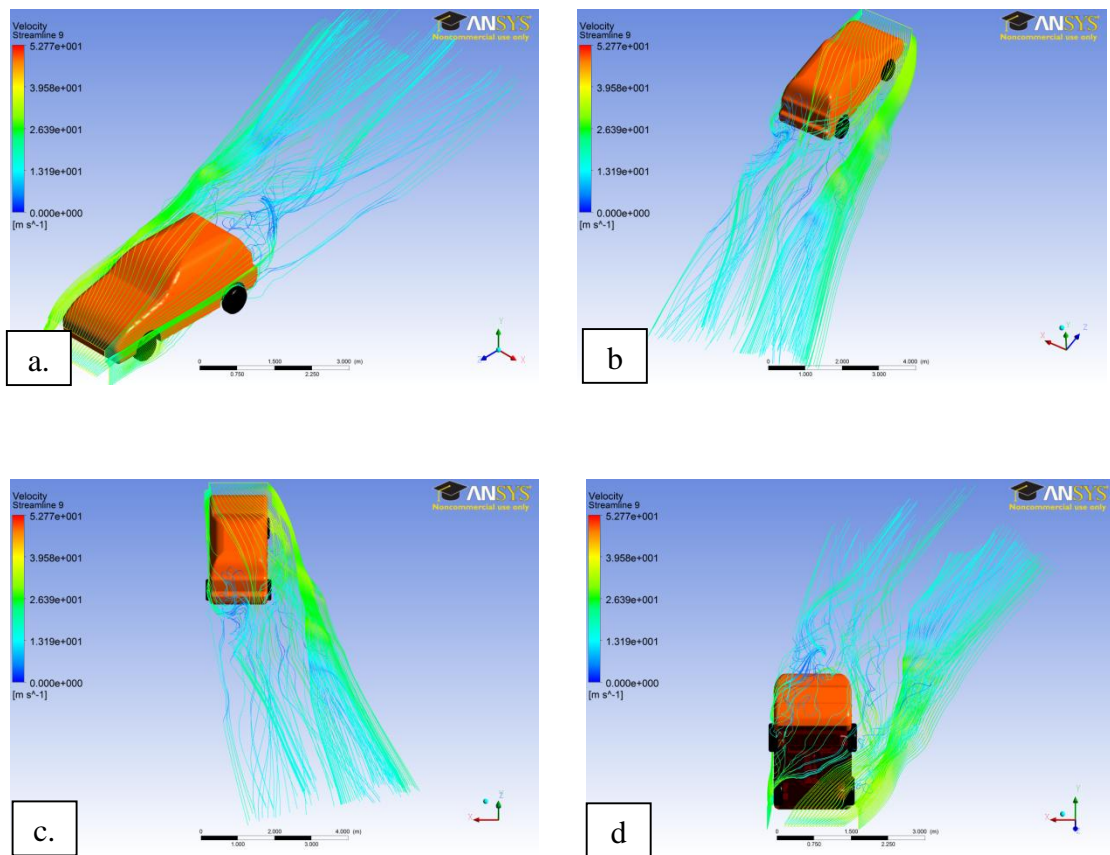


Figure 4.59: Velocity streamlines a.) in front of the vehicle, b.) behind the vehicle, c.) over and d.) under the vehicle for Test 8.

Figure 4.60 shows streamlines of the flow around the vehicle for Test 3 in various views from a.) in front of the vehicle, b.) behind the vehicle, c.) over and d.) under the vehicle. The extreme yaw angle required the starting points of the streamlines to be shifted over 1 m towards the driver's side in order to properly envelope the vehicle. Here a large amount of vortices are seen coming off of the driver's side in Figs. 4.60, b and c, with passenger side flow separating almost immediately off of the front passenger's corner of the car. Underneath the vehicle in Fig. 4.60d, the flow is clearly shown sweeping across over the hotplate in the same direction that the heat convected over it.

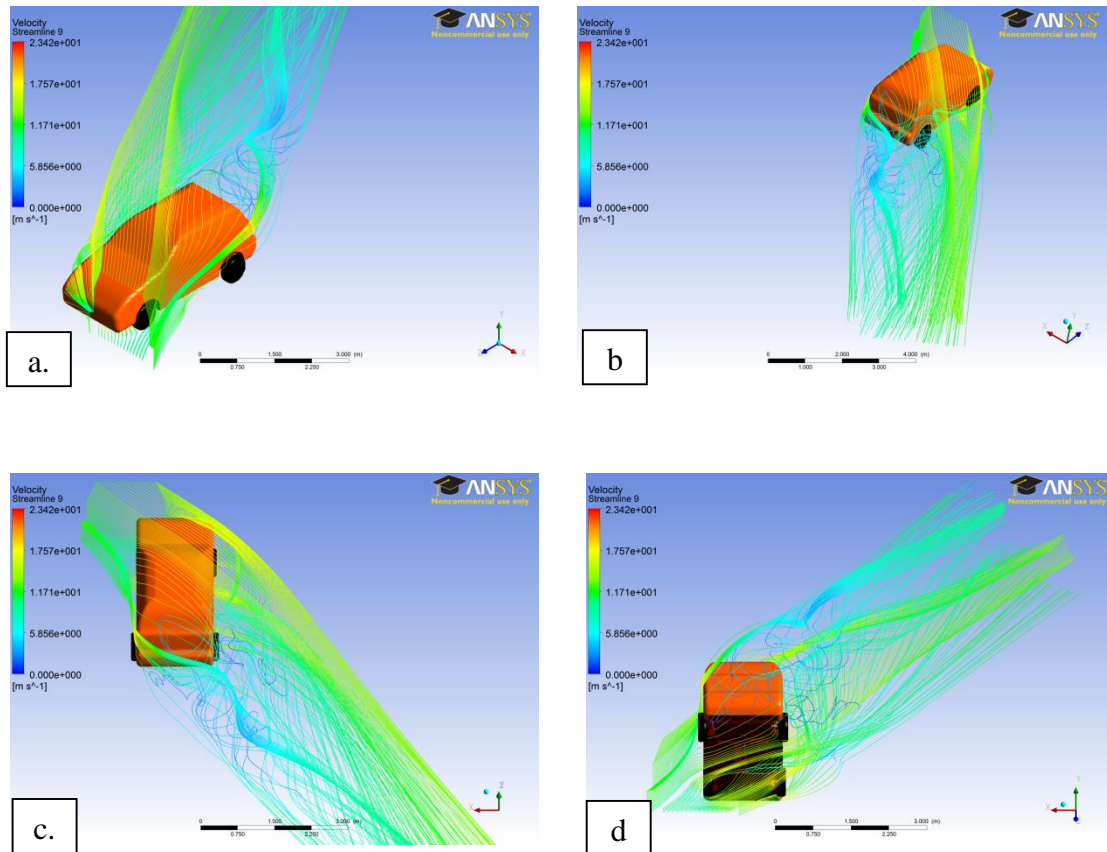


Figure 4.60: Velocity streamlines a.) in front of the vehicle, b.) behind the vehicle, c.) over and d.) under the vehicle for Test 3.

4.3: Underbody Battery Pack Cooling Simulation Results

The results presented in Section 4.2 indicate that underbody cooling can provide appreciable benefits when applied to a generic case, such as the experimental design using the hotplate. Using this as a baseline, applying the underbody cooling concept to a more realistic situation is the next step. As discussed in Chapter 1, there are huge challenges in cooling battery packs of EV and HEV vehicle. This could also be addressed through external air cooling like the experimental case with the hotplate. The battery packs are typically located under the vehicle or towards the rear of the vehicle in an effort to maximize interior packaging requirements and lower the vehicle's centre of gravity. The battery consists of numerous cells that store and discharge energy to drive the electric motor depending on the driving demands. The charging and discharging rates of a cell depend on the temperature of the individual cell. However, the energy requirements from the vehicle apply to the whole battery pack. If an individual cell is charging at a different rate because of a localized temperature increase, this could lead to overcharging the cell, damaging the cell and thus reducing the capacity of the battery. To prevent these temperature localizations, the batteries are also required to be maintained at a consistent and uniform temperature. External cooling of the battery can help to reduce existing battery cooling system demands, such as reducing fan or pump speed, thus reducing the energy required by these systems.

Current air cooling methods focus on internally cooling the battery pack through the cells and different manifold designs (Park, 2013, Pearson et al., 1999) and improving said designs in order to increase their effectiveness. For external cooling, potential optimizations are available using external aerodynamic devices to channel and speed up

the air, such as a diffuser. The battery pack is built into the angled surface of a drag and downforce diffuser design as suggested by Jowsey and Passmore (2013) and compared to a case where no diffuser is used. This section analyzes the effects of the local velocity changes through the diffuser and also its effects on the surface temperature of the battery pack. Given an appropriate vehicle speed, this forced convection could be achieved through diffuser effects instead of using energy to power a fan to drive the air. This offers potential energy savings. The idea is to observe whether the velocity (and related convective heat transfer) increase at the inlet of the diffuser can overcome the reduction in convective heat transfer at the diffuser exit due to the reduction in velocity.

4.3.1: Numerical Results

Figure 4.61 shows the velocity contours at the vehicle centerline.

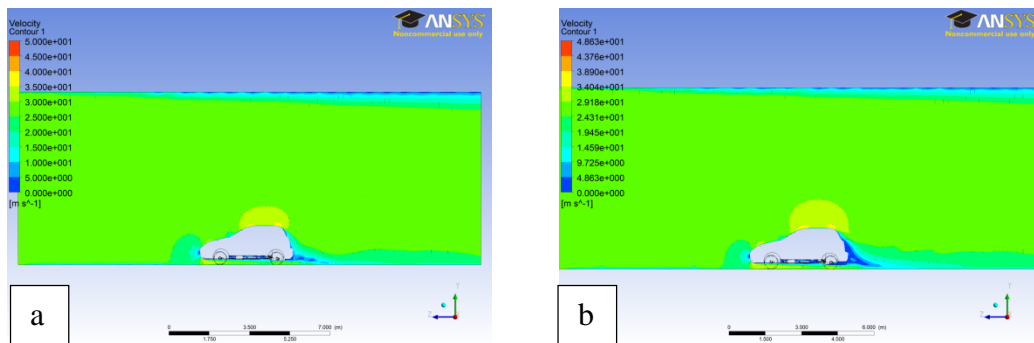


Figure 4.61: Velocity contours at vehicle centerline for a) the no diffuser case, and b) the diffuser case.

The wake appears to be well resolved. The wake continues to follow the streamlines coming off of the roof of the vehicle. Figs. 4.62 and 4.63 show the flow patterns at the front and rear of the vehicle at the centerline respectively.

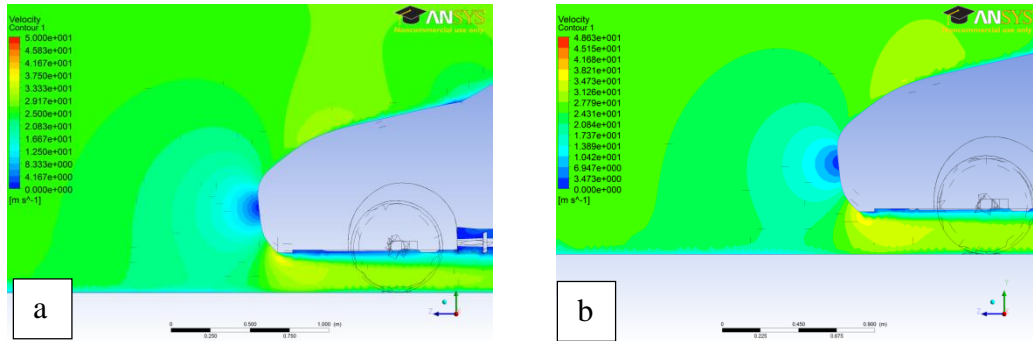


Figure 4.62: Velocity contour at vehicle centerline at the front of the vehicle for a.) the no diffuser case and b.) the diffuser case.

At the front of the vehicle, the velocity contours are the same. This is expected since the front geometries of the vehicles in both test cases are the same. The size of the recirculation zone looks larger for the diffuser case. The size of the dead air – the area of low or no velocity behind the car – is larger for the diffuser case. Given that this is a drag and downforce optimized diffuser design, this means there is a high pressure area behind the car to counteract the stagnation point in front the car, thus reducing pressure drag. Also of note is that the flow is not entirely separated from the battery pack. The flow near it is slower, as expected since the flow continues downstream to the rear of the vehicle. At the throat of the diffuser, a larger region of the air is faster compared to the no diffuser case.

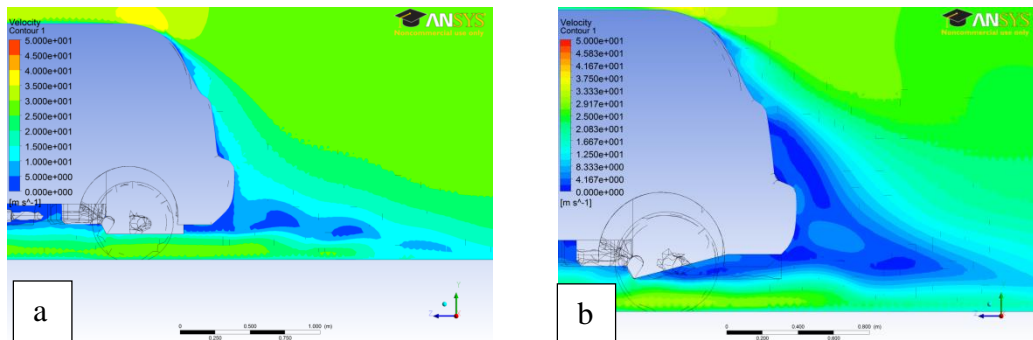


Figure 4.63: Velocity contour at vehicle centerline at the rear of the vehicle for a.) the no diffuser case and b.) the diffuser case.

Figures 4.64 and 4.65 show the streamlines of the air near the vehicle's rear section showing the flow at the top of the vehicle and underneath it. These streamlines reinforce the impressions made from the velocity contours at the vehicle centerline: the size of the dead air area behind the vehicle is larger in the diffuser case as shown by Fig. 4.64b compared to Fig. 4.65b. This is shown through the streamlines spiraling closer to the trunk in the diffuser case versus the no diffuser case.

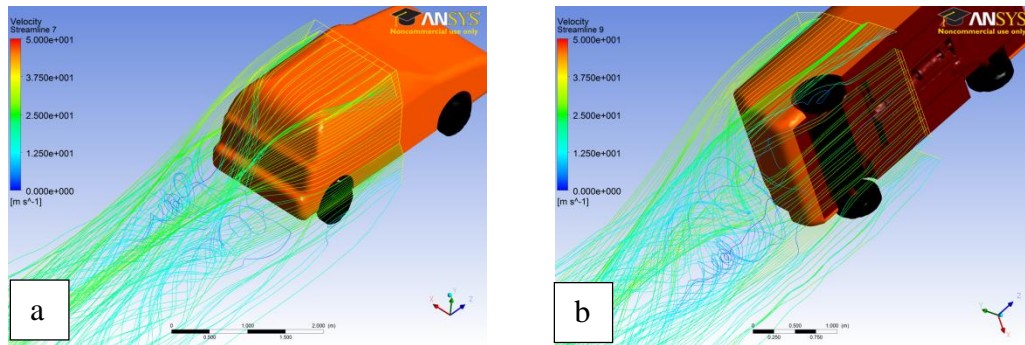


Figure 4.64: Velocity streamlines at the rear section of the vehicle for the no diffuser case showing a.) the top-rear view and b.) the bottom rear view.

In addition, the diffuser helped to control the formation of vortices in the wake in the rear bumper section. Figure 4.64a shows vortices coming off the rear bumper from the sides and underneath the vehicle, whereas the diffuser case in Fig. 4.65a only shows vortices coming off the sides of the diffuser underneath the vehicle, with the flow off the sides of the vehicle detaching from the surface smoothly. The reduction in vortices creates a higher pressure behind the vehicle in the diffuser case, thus reducing drag, as expected from the drag-optimized diffuser design.

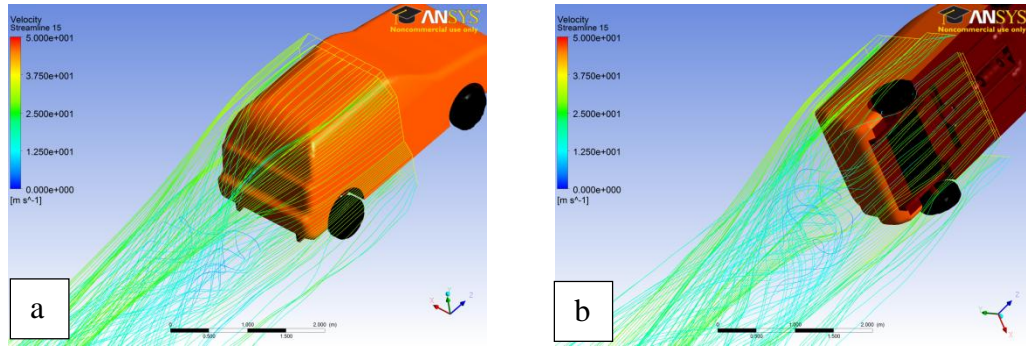


Figure 4.65: Velocity streamlines at the rear section of the vehicle for the diffuser case showing a.) the top-rear view and b.) the bottom rear view.

Figure 4.66 demonstrates the temperature contours of the battery pack with some noticeable patterns. There exist hot spots in both cases, likely due to the asymmetrical underbody of the vehicle affecting the flow. For the no diffuser case, the hot spots exist both near the leading edges and towards the middle of trailing edge of the battery pack. However, for the diffuser case, the hot spots are roughly in the middle of the rear trailing edge. The diffuser also appears to be delaying the onset of the hot spots on the battery pack, moving them further downstream. So while the maximum temperature did slightly increase in the battery pack, the increased velocity at the throat of the diffuser does appear to be aiding cooling of the leading edge of the battery pack more consistently.

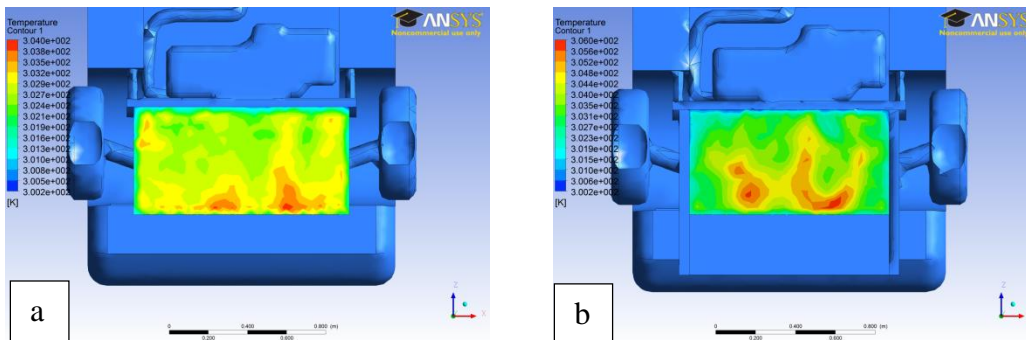


Figure 4.66: Temperature contour of the battery pack for a.) the no diffuser case and b.) the diffuser case.

Figure 4.67 shows the temperature contour at the vehicle centerline for both cases. It is apparent that the convective heat transfer on the battery pack surface dominates the heat transfer away from the battery until the flow separates off the battery pack downstream in the no diffuser case, and thus the temperature contour spreads away from the surface more due to radiative heat transfer. Conversely, the flow near the battery pack surface is slower in the diffuser case thus the effects of radiative heat transfer have a larger visible impact.

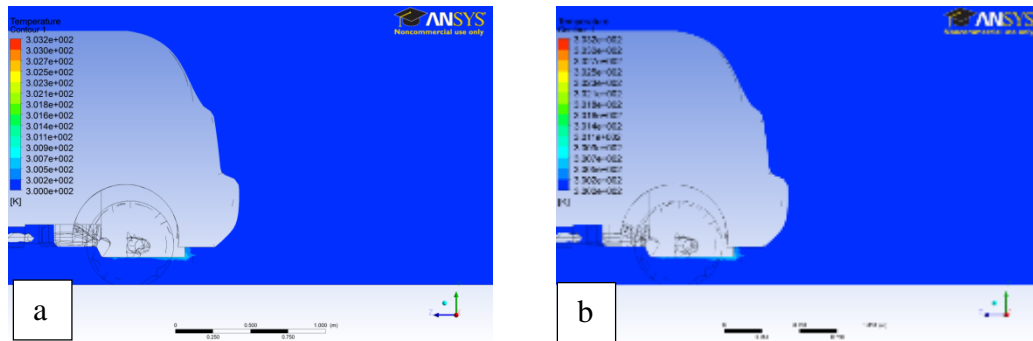


Figure 4.67: Temperature contour of the battery pack at the vehicle centerline for a.) the no diffuser case and b.) the diffuser case.

Figures 4.68, 4.69 and 4.70 show isosurfaces at temperatures of 300.125K, 301K and 303K respectively. These isosurfaces help to illustrate the areas of the flow at a given temperature. Fig. 4.68b shows how in the diffuser case the heat relatively quickly moved from the diffuser inlet, as shown by the shorter isosurface. However, Fig. 4.68a shows how the heat is somewhat trapped behind the battery pack due to recirculations immediately off the trailing edge, while in the diffuser case of Fig. 4.68b, the heat disperses fast due to the integrated design of the battery pack with the diffuser eliminating the recirculation zone.

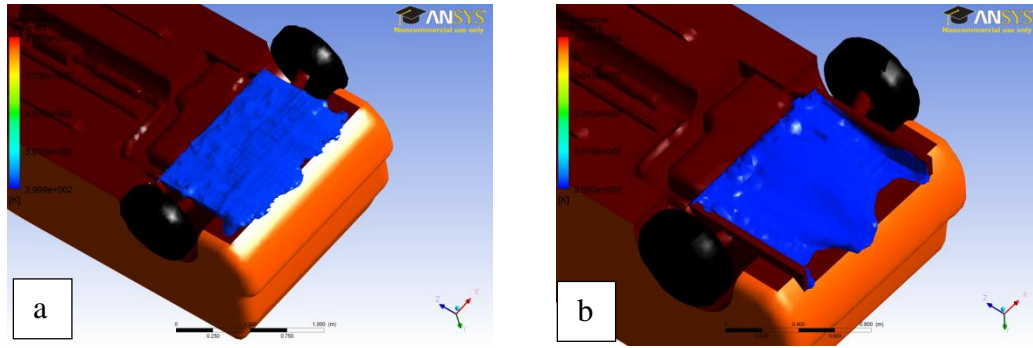


Figure 4.68: Temperature isosurface at 300.125K of the battery pack at the vehicle centerline for a.) the no diffuser case and b.) the diffuser case.

Figure 4.69 shows isosurfaces at 301K. Comparing Figs. 4.68a to 4.68b, it is clear that in the diffuser case more air near the battery is at this given temperature, especially downstream near the rear of the battery pack where there appears to be larger pockets of air at 301K. The asymmetrical nature of the pockets could be a result of the asymmetrical underbody upstream of the flow. This is also consistent with the observation that at the leading edge of the diffuser the hot air is quickly removed, as shown by the isosurface at further downstream in the diffuser case versus the no diffuser case. Finally, Figs. 4.70 shows isosurfaces at 303K with a smaller isosurface in Fig. 4.70a compared to Fig. 4.70b, it is clear that convection dominates the heat transfer in the no diffuser case.

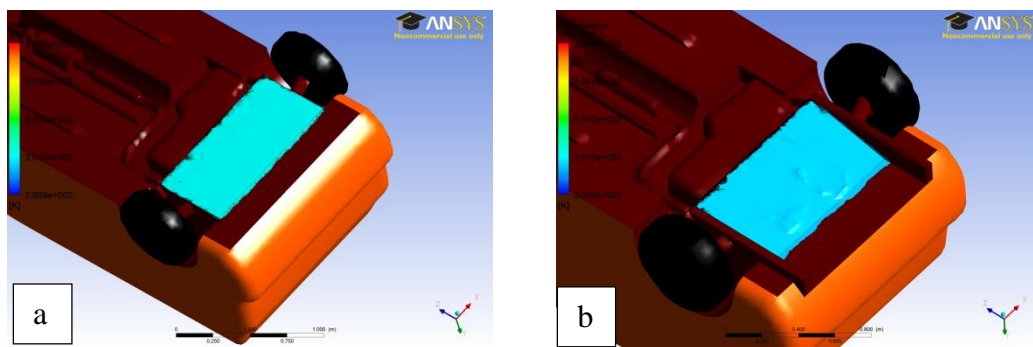


Figure 4.69: Temperature isosurface at 301K of the battery pack at the vehicle centerline for a.) the no diffuser case and b.) the diffuser case.

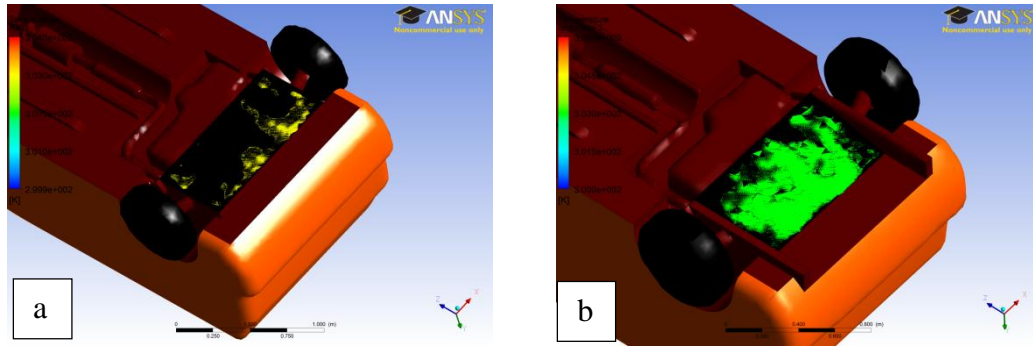


Figure 4.70: Temperature isosurface at 303K of the battery pack at the vehicle centerline for a.) the no diffuser case and b.) the diffuser case.

Chapter 5: Conclusion and Recommendations

This thesis had two main goals with regards to underbody aero-thermal research. The first was to conduct a fundamental study using an arbitrary heat source to understand how heat and velocity is distributed under a passenger car in various wind speeds and yaw angles. This was achieved using wind tunnel measurements and numerical simulations. The second goal was to apply the fundamental study to a realistic case, such as a theoretical Chevrolet Aveo5 hybrid electric vehicle (HEV) battery pack requiring cooling. In addition, to investigate whether cooling of battery packs can be improved through the use of a vehicle aerodynamic device such as an underbody diffuser. This second objective was achieved using numerical simulation. The conclusions drawn from this study are summarized in Section 5.1 below.

5.1: Summary of Results

The results confirmed that the underbody cooling strongly depends on wind speed. In general, a higher wind speed tended reduce the range in temperature at locations near the heat source, with the maximum temperature variation between all the tests of nearly 10°C at 100 km/h wind speed versus 15°C at 50 km/h. This is attributed to increased turbulence under the vehicle which enhanced mixing and diffusion of heat, thus increasing the convective heat transfer coefficient.

Greater than the wind speed, however, is the effect of yaw angle. The relative angle of the vehicle to the wind direction has a huge effect on how the heat is distributed under the vehicle. The angle changes the way the flow interacts with the hot plate, greatly altering of the local flow direction. This causes other aerodynamic effects such as recirculation and wake regions. As the vehicle yaws and exposes only one side of the hot plate to the

incoming cooling air, the flow deflects off of the hot plate and carries the heat downstream on the exposed side. This results in non-uniform cooling of the hot plate. It was observed that irrespective the yaw used, only the thermocouples in the vicinity of the hot plate recorded significant temperatures. It was also observed that the rear axle deflected the airflow and prevented heat from getting to the thermocouples behind it.

The CFD results were consistent with this observation. At 0° yaw, the temperature was relatively evenly distributed at both the driver and passenger sides of the hot plate. As the yaw angles increased (to 29.6°) the driver side of the hot plate was more exposed to the airflow which convected the heat to the downstream to the passenger side to increase of the temperature in that region. When the direction of the yaw angle changed to negative 29.6° the trends described above were reversed as expected although not identical. The different ambient temperatures affect the distribution by changing which yaw angle the maximum temperature was observed; at 10°C ambient temperature, the maximum was at 15.6° yaw whereas at 50°C ambient temperature the maximum was at 0° yaw. Heat also convects away perpendicularly to the hot plate, as shown in the three-dimensional profiles of the isosurfaces.

With regards to velocity, the surface of the vehicle underbody the flow is highly turbulent. The exhaust piping channel affected both the flow direction and velocity the most. On the other hand, when the yaw angle increased to 15.6° and higher, more consistent flow patterns were observed at sections more exposed to the nozzle airflow.

Overall, the diffuser did have a noticeable effect on the temperature and velocity distribution underneath the car. Closer to the throat of the diffuser, the temperatures were

relatively more consistent compared to the no diffuser case. It is shown that the temperature of the battery pack upstream decreased whereas that at the downstream slightly increased compared to the no diffuser case. In addition, a larger range of temperatures were observed, with a 6K variance versus 4K of the no diffuser case. The huge advantage of the diffuser case is that there are smaller hot spots in comparison to the no diffuser case. These small hot spots limit the number of cells in a battery that would be affected by the drastic temperature increase, thus preventing damage to the overall pack. If in a more extreme case the temperature difference could be higher, leading to a more extreme difference in charging/discharging rates.

5.2: Contribution

There is no studies in the open literature that investigated the relationship between underbody aerodynamics and underbody thermodynamics. This study fills that gap and provides results showing how underbody thermodynamics are affected by wind speed, and yaw angle as well as ambient temperature. The physical insight this study provided is necessary for automotive engineers to design more effectively underbody vehicle packaging to enhance cooling of underbody heat sources. The measurements made in the boundary layer above the heat source showed significantly different patterns at different cross flows, wind speeds and ambient temperatures.

Furthermore, this thesis was initiated by an industry partner to study the effects of cross winds on vehicle aero-thermal phenomena. The results reported are useful to wind tunnel designers in developing design trade-offs involved with thermal phenomena due to cross-wind effects or in justifying to customers the benefits of incorporating yawing capability in their wind tunnels.

In regards to the battery pack study, aerodynamic devices are used to improve the air flow under the vehicle to help improve the external cooling of the battery. As shown in the analysis of the battery pack, there are valid benefits to underbody aero-thermal research, with a drag and downforce optimized diffuser stabilizing the temperature at the surface of the battery, reducing the risk of damage to the individual cells through under- or over-charging.

5.3: Recommendations for Future Works

The experimental part of this thesis was limited to two-dimensional measurements. To further improve the baseline results, more research is needed investigate experimentally the three-dimensional heat distribution with layers of thermocouples, increase velocity measurements, and increased numbers of thermocouples to solidify the trends observed.

The current study investigates the use of generic diffuser to improve cooling of battery pack. Future work should focus on optimizing a diffuser design specifically for battery pack cooling. This is more likely to provide better opportunities to optimize the effectiveness of air cooling the battery pack surface.

References

Al-Hallaj, S, and Selman, J.R. (2002) “Thermal Modeling of Secondary Lithium Batteries for Electric Vehicle/Hybrid Electric Vehicle Applications.” *Journal of Power Sources* 110 (2002), pp 341-348

Al-Waked, R and Behnia, M. (2004) “The Performance of Natural Draft Dry Cooling Towers Under Crosswind: CFD Study”. *International Journal of Energy Research*. 24. pp 147-161.

Alajbegovic, A, Amodeo, J, and Jansen, W. (2006) “Thermal Management Simulation for Passenger Cars – Towards Total Vehicle Analysis”. *EXA Corporation and Jaguar Cars*.

Apolloni, M. (2006) “Derivation of a 1-D Thermal Model of Vehicle Underhood Temperatures on the Basis of Test Data using an Evolutionary Algorithm”. *ETH – Swiss Federal Institute of Technology*.

Baker, C.J. (1991a). “Ground Vehicles in High Cross Winds Part I: Steady Aerodynamic Forces” *Journal of Fluids and Structures*. Vol 5. pp 69-90.

Baker, C.J. (1991b). “Ground Vehicles in High Cross Winds Part II: Unsteady Aerodynamic Forces” *Journal of Fluids and Structures*. Vol 5. pp 91-111.

Baker, C.J. (1991c). “Ground Vehicles in High Cross Winds Part III: The Interaction of Aerodynamic Forces and the Vehicle System” *Journal of Fluids and Structures*. Vol 5. pp 221-241.

Barnard, R.H. “Drag and Lift” (2009) in Barnard, R.H *Road Vehicle Aerodynamic Design: An Introduction*. Third Edition. St. Albans, Hertfordshire, England. MechAero.

Barnard, R.H. “Understanding Air Flows” (2009) in Barnard, R.H *Road Vehicle Aerodynamic Design: An Introduction*. Third Edition. St. Albans, Hertfordshire, England. MechAero.

Barnard, R.H. “Racing Cars and Other High-Performance Vehicles” (2009) in Barnard, R.H *Road Vehicle Aerodynamic Design: An Introduction*. Third Edition. St. Albans, Hertfordshire, England. MechAero.

- Barnard, R.H. “Internal Air Flows – Engine and Transmission Cooling” (2009) in Barnard, R.H. *Road Vehicle Aerodynamic Design: An Introduction*. Third Edition. St. Albans, Hertfordshire, England. MechAero.
- Barnard, R.H. (2000) “Theoretical and Experimental Investigation of Aerodynamic Drag Due to Automotive Cooling Systems”. *Journal of Automobile Engineering*. 214.8, pg 919-927.
- Bearman, P.W. (1980) “Review – Bluff Body Flows as Applied to Vehicle Aerodynamics”. *Journal of Fluids Engineering*. Vol. 102, pg 265-274.
- Beaudoin, J.F, Aider, J.L. (2008) “Drag and Lift Reduction of a 3d Bluff Body using Flaps”. *Experimental Fluids*. Vol 44, pp 491-501.
- Bennon, P.I.K. (2010) National Renewable Energy Laboratory. *Integrated Vehicle Thermal Management*.
- Bitsche, O., and Gutmann, G. (2004) “Review – Systems for hybrid cars”. *Journal of Power Sources*. Vol. 127, pp 8-15.
- Chan, C.C. (2007) “The State of the Art of Electric, Hybrid and Fuel Cell Vehicles”. *Proceedings of the IEEE*. Vol. 95, No. 4, pp. 704-718.
- Cooper, K.R. (1984) “The Wind-Tunnel Simulation of Surface Vehicles” *Journal of Wind Engineering and Industrial Aerodynamics*. Issue 17, pp 167-198.
- Cooper, K.R. (1991) “The Wind-Tunnel Simulation of Wind Turbulence for Surface Vehicle Testing” *Journal of Wind Engineering and Industrial Aerodynamics*. Issue 38, pp 71-81.
- Cooper, K.R. (1993) “Bluff Body Aerodynamics as Applied to Road Vehicles”. *Journal of Wind Engineering and Industrial Aerodynamics*. Issue 49, pp. 1-22.
- Costa, E. (2003) “CFD Approach on Underhood Thermal Management of Passenger Cars and Trucks”. *SAE Technical Papers*. 2003-02-3577.
- Fago, B., Lindner, H., and Mahrenholtz, O. (1991) “The effect of ground simulation on the flow around vehicle in wind tunnel testing”. Vol. 38, pp 47-57.

- Foss, J.F, Schwannecke, J.K, Lawrenz, A.R, Mets, M.W, Treat, S.C, and Dusel, M.D. (2004) "The Thermal Transient Anemometer". *Measurement Science and Technology*. 15. pp 2248-2255.
- Fournier, E. (2004) *Underhood Temperature Measurements of Four Vehicles*. Biokinetics and Associates Ltd. <http://www.mvfri.org/Contracts/Final%20Reports/R04-13v01%20Underhood%20Temperatures%201.pdf>. Accessed June 6, 2013.
- George, A.R. "Aerodynamic Effects of Shape, Camber, Pitch and Ground Proximity on Idealized Ground-Vehicle Bodies". *Journal of Fluids Engineering*. Vol. 103. Pp 631-637.
- Heft et al. (2012) "Introduction of a New Realistic Generic Car Model for Aerodynamic Investigations," *SAE International*, 2012-01-0168
- Howell, J., Passmore, M., and Tuplin, S. (2013) "Aerodynamic Drag Reduction on a Simple Car-Like Shape with Rear Upper Body Taper," *SAE Int. J. Passeng. Cars - Mech. Syst.* 6(1):52-60
- Hucho, Wolf-Heinrich. (1993) "Aerodynamics of Road Vehicles". *Annu. Rev. Fluid Mech.* 1993-25. pg 485-537.
- Incopera, F.P, DeWitt, D.P, Bergman, T.L, Lavine, A.S. "Introduction" (2006) in Incopera, F.P, DeWitt, D.P, Bergman, T.L, Lavine, A.S. *Fundamental of Heat and Mass Transfer*. Sixth Edition. John Wiley and Sons.
- Jones, M.A, and Smith, F.T. (2003) "Fluid Motion for Car Undertrays in Ground Effect". *Journal of Engineering Mathematics*. Vol. 45, pp. 309-334.
- Jowsey, L., and Passmore, M. (2010) "Experimental study of multiple-channel automotive underbody diffusers," *Proceedings of the Institution of Mechanical Engineers*, Issue 224, pp 865-879.
- Kang, S.O et al. (2011) "Actively Translating a rear diffuser device for the aerodynamic drag reduction of a passenger car". *International Journal of Automotive Technology*, Vol 13 No.4, pp 583-592.
- Karniadakis, G., and Sherwin, S "Introduction" (2005) in *Spectral/hp Element Methods for CFD: Second Edition*. New York, NY, USA. Oxford University Press.

Katz, J. “Airfoils and Wings” (1995a) in Katz, J. *Race Car Aerodynamics: Designing for Speed*. Cambridge, MA, USA. Bentley Publishers.

Katz, J. “Aerodynamics of the Complete Vehicle” (1995b) in Katz, J. *Race Car Aerodynamics: Designing for Speed*. Cambridge, MA, USA. Bentley Publishers.

Khaled, M, Alshaer, A, Hachem, F, Harambat, F, and Peerhossani, H. (2012) “Effects of Ground Vehicle Inclination on Underhood Compartment Cooling”. *International Journal of Automotive Technology*. 13.6, pp 895-904.

Kizilel, R., Sabbah, R., Selman, J.R., Al-Hallaj, S. (2009) “An Alternative Cooling System to Enhance the Safety of Li-ion Battery Packs”. *Journal of Power Sources*. Vol. 194. pp. 1105-1112.

Kleber, A. (2001) “Simulation of Air Flow Around an OPEL ASTRA Vehicle with FLUENT”. *Journal Articles by fluent Software Users*. JA132.

Knaus, H, Ottosson, C, Brotz, F, and Kühnel, W. (2005) “Cooling Module Performance Investigation by Means of Underhood Simulation”. *SAE Technical Papers*. 2005-01-2013.

Kuthada, T and Wiedemann, J. (2008) “Investigations in a Cooling Air Flow System under the Influence of Road Simulation”. *SAE Technical Papers*. 2008-01-0796.

Lan, K.T and Srinivasan, K. (2009) “Influences of Free Stream Conditions on Vehicle Thermal Management – An Analytical Study”. *SAE Technical Papers*. 2009-01-1152.

Lanfrit, M. (2005) “Best Practice Guidelines for handling Automotive External Aerodynamics in FLUENT”. *ANSYS*. Version 1.2.

Lietz, R.L (2001) “Vehicle Aerodynamic Shape Optimization”. *SAE International*, 2011-01-0169.

Lin, C, Saunders, J.W and Watkins, S. (2007) “Effect of Cross-Winds on Motor Car Engine Cooling”. *SAE Technical Papers*. 970138.

Mahamud, R., and Park, C. (2011) “Reciprocating air flow for Li-ion battery thermal management to improve temperature uniformity”. *Journal of Power Sources*. Vol 196, pp 5685-5696.

- Marklund, J. (2013) "Under-body and diffuser flows of Passenger Vehicles: The influence of vehicle rear under-body design on the total drag coefficient" ISBN 978-91-7385-866-3.
- Menter, F.R., Kuntz, M., and Langtry, R. (2003) "Ten Years of Industrial Experience with the SST Turbulence Model". *Turbulence, Heat and Mass Transfer 4*.
- Ripple, D.C. (1995). "NIST ITS-90 Thermocouple Database". *National Institute of Standards and Technology*. <http://srdata.nist.gov/its90/main/>. Accessed November 25, 2014.
- Ng, E.Y, Watkins, S, Johnson, P.W and Mole, L. (2002) "Use of a Pressure-Based Technique for Evaluating the Aerodynamics of Vehicle Cooling Systems," *SAE Technical Papers*. 2002-01-0712.
- Nobel, T.P and Jain, S.K. (2001) "A Multi-Dimensional Approach to Truck Underhood Thermal Management". *SAE Technical Papers*. 2001-01-2785.
- Park, H. (2013) "A Design of Air Flow Configuration for Cooling Lithium Ion Battery in Hybrid Electric Vehicles". *Journal of Power Sources*. Issue 239, pp 30-36.
- Pesaran, A.A. (2001) National Renewable Energy Laboratory. *Battery Thermal Management in EVs and HEVs: Issues and Solutions*.
- Pesaran, A.A. (2002) "Battery Thermal Models for Hybrid Vehicle Simulations". *Journal for Power Sources*. Vol. 110, pp. 377-382.
- Pesaran, A.A, Burch, S., Keyser, M. (1999) "An Approach for Designing Thermal Management Systems for Electric and Hybrid Vehicle Battery Packs". Paper presented at *The Fourth Vehicle Thermal Management Systems Conference and Exhibition*. May 24-27, 1999, London, UK.
- Pesaran, A.A, Vlahinos, A., and Burch, S.D. (1997) National Research Energy Laboratory. *Thermal Performance of EV and HEV Battery Modules and Packs*.
- Pesaran, A.A, Vlahinos, A., and Stuart, T. (2003) "Cooling and Preheating of Batteries in Hybrid Electric Vehicles". Paper presented at the *6th ASME-JSME Thermal Engineering Joint Conference*. March 16-20, 2003.

Regert, T and Lajos, T. (2007) “Description of flow field in the wheelhouses of cars”. *International Journal of Heat and Fluid Flow*. Vol 28, pp 616-629.

Rao, Z., and Wang, S. (2011) “A review of power battery thermal energy management”. *Renewable and Sustainable Energy Reviews*

Roache, P.J., K. Ghia, and F. White, "Editorial Policy Statement on the Control of Numerical Accuracy," ASME Journal of Fluids Engineering, Vol. 108, No. 1., March 1986, p. 2.

Renn, V., and Gilhaus, A (1986) “Aerodynamics of Vehicle Cooling Systems”. *Journal of Wind Engineering and Industrial Aerodynamics*. Vol. 22, pp 339-346.

Sabbah, R., Kizilel, R., Selman, J.R., Al-Hallaj, S. (2008) “Active (air-cooled) vs. Passive (phase change material) thermal management of high power lithium-ion packs: Limitation of temperature rise and uniformity of temperature distribution”. *Journal of Power Sources*. Vol. 182, pp. 630-638.

Siqueira, C. L, Vatauvuk, P, Jokuszies, M, Lima, M.R. (2002) “Numerical Simulation of a Truck Underhood Flow”. *SAE Technical Papers*. 2002-01-3453.

Slater, J. (2008) “Examining Spatial (grid) Independence”. NPARC Alliance CFD Verification and Validation. NASA. <
<http://www.grc.nasa.gov/WWW/wind/valid/tutorial/spatconv.html>>. Accessed October 24, 2014.

Talom, H.L and Beyene (2008), A. “Heat Recovery from Automotive Engine.” *Applied Thermal Engineering*. Vol. 29. pp 439-444.

Tsubokura, M., Kobayashi, T., Nakashima, T., Nouzawa, T., Nakamura, T., Zhang, H., Onishi, K., and Oshima, N. (2008) “Computational visualization of unsteady flow around vehicles using high performance computing”. *Computers & Fluids*.

Uhl, B, Brotz, F, Fauser, J and Krüger, U. (2001) “Development of Engine Cooling Systems by Coupling CFD Simulation and Heat Exchange Analysis Programs”. *SAE Technical Papers*. 2001-01-1695.

White, F.M (2008). “Introduction” in White, F.M (2008) *Fluid Mechanics*. Sixth Edition. New York, New York, United States of America. McGraw Hill.

White, F.M (2008). “Integral Relations for a Control Volume” in White, F.M (2008) *Fluid Mechanics*. Sixth Edition. New York, New York, United States of America. McGraw Hill.

Wille, S, Kuthada, T, Widdecke, N, and Wiedemann, J. (2010) “Integrated Numerical and Experimental Approach to Determine the Cooling Air Mass Flow in Different Vehicle Development Stages”. *SAE Technical Papers*.2010-01-0287.

Yilbas, B. (2013) *Introduction to Turbulence*, PDF. University of Ontario Institute of Technology, viewed July 7, 2014. <ENGR 5122G Blackboard site>

Zhang, X, Toet, W, Zerihan, J. (2006) “Ground Effect Aerodynamics of Race Cars”. *Applied Mechanics Reviews*, Vol. 59, pg 33-49.

Appendix A: Passenger Side Grid Independence Test

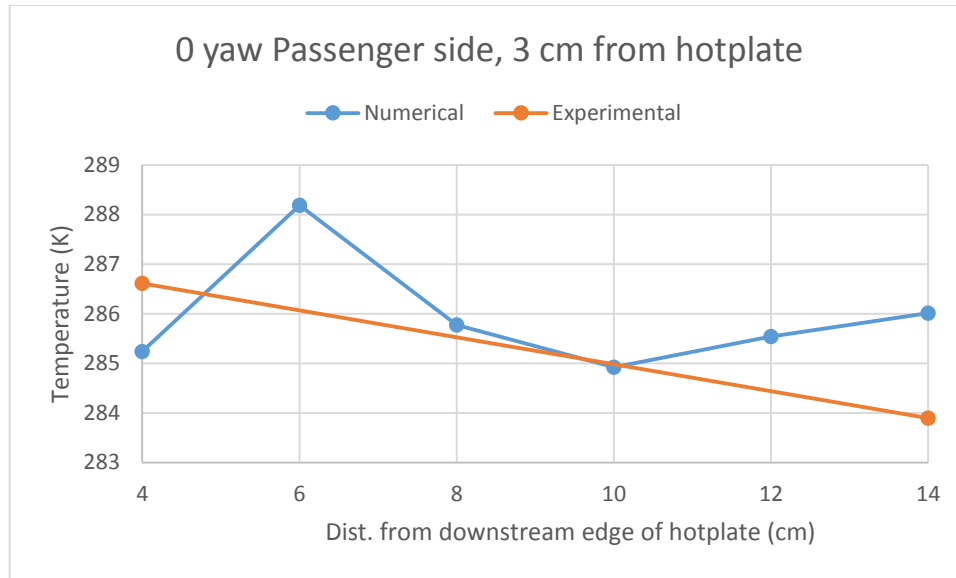


Figure A.1: Comparison of numerical and experimental temperature data 3 cm away from the hotplate at 0° yaw on the driver side.

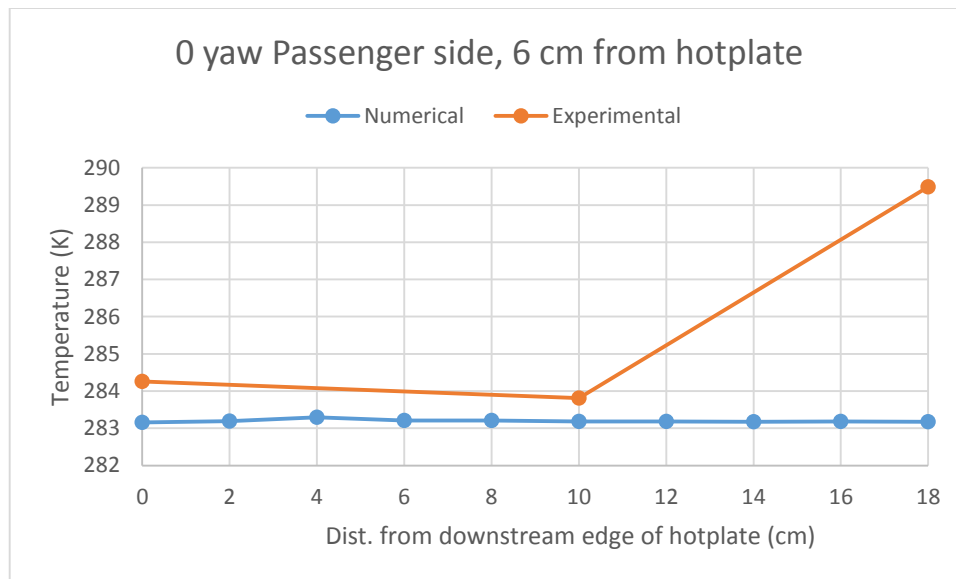


Figure A.2: Comparison of numerical and experimental temperature data 6 cm away from the hotplate at 0° yaw on the driver side.

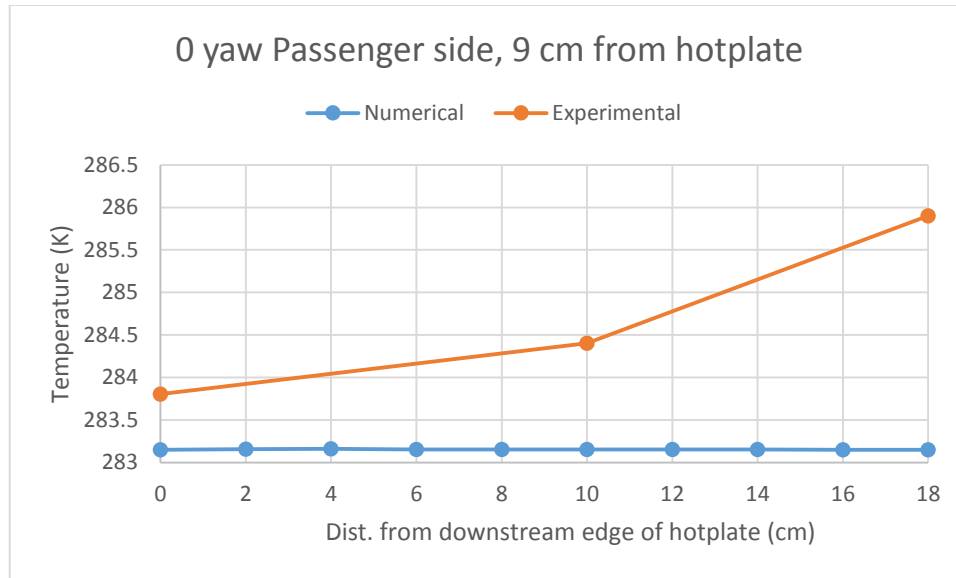


Figure A.3: Comparison of numerical and experimental temperature data 9 cm away from the hotplate at 0° yaw on the driver side.

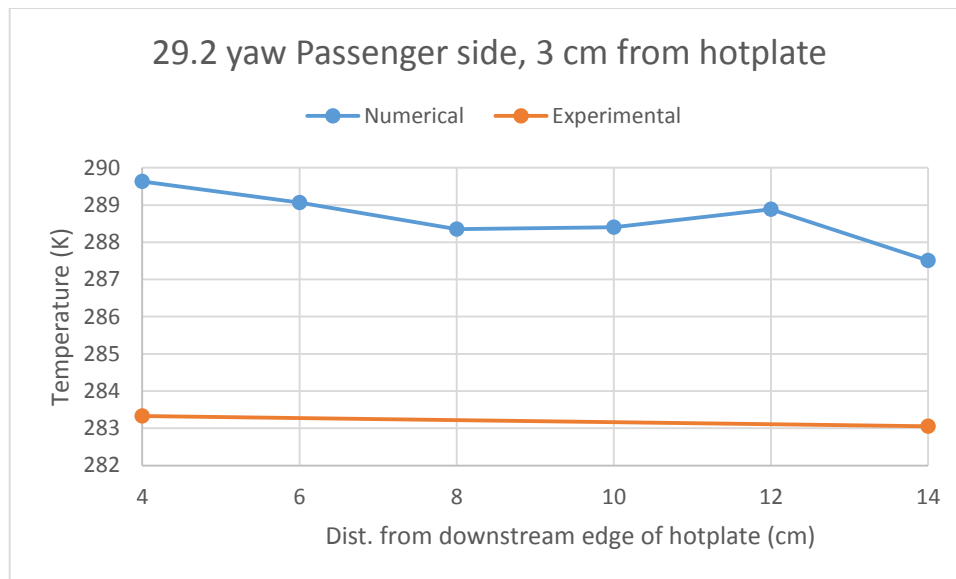


Figure A.4: Comparison of numerical and experimental temperature data 3 cm away from the hotplate at 29.2° yaw on the driver side.

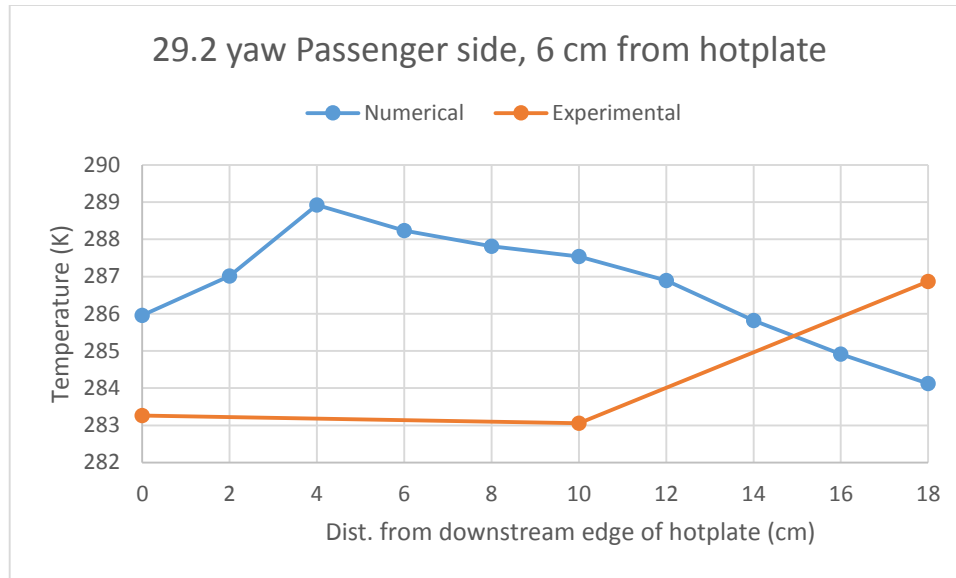


Figure A.5: Comparison of numerical and experimental temperature data 6 cm away from the hotplate at 29.2° yaw on the driver side.

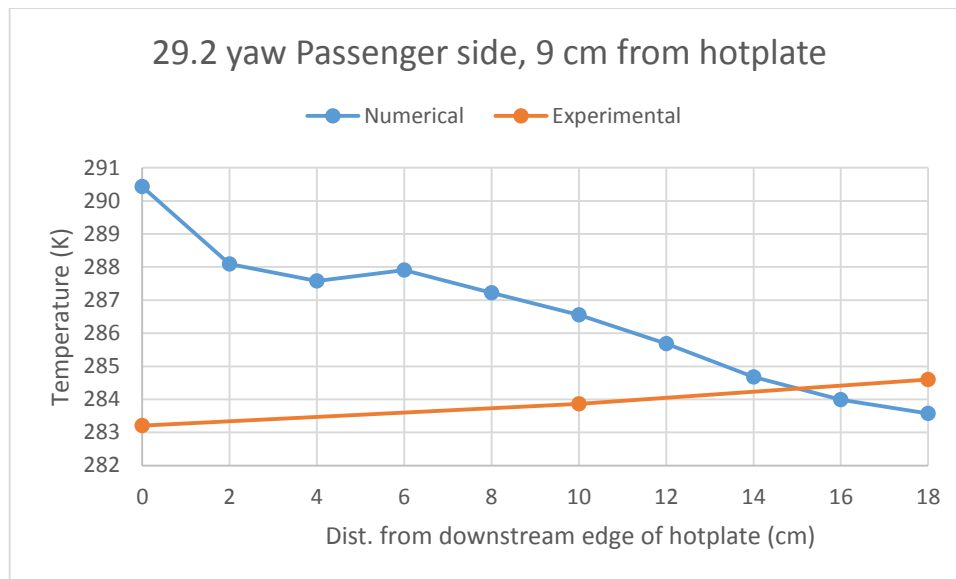


Figure A.6: Comparison of numerical and experimental temperature data 9 cm away from the hotplate at 29.2° yaw on the driver side.